Directed Assembly of Nanomaterials for Making Nanoscale Devices and Structures: Mechanisms and Applications

Zhimin Chai, Anthony Childress, and Ahmed A. Busnaina*

Read Online

ACCESS | Metrics & More | Article Recommendations

ABSTRACT: Nanofabrication has been utilized to manufacture one-, two-, and three-dimensional functional nanostructures for applications such as electronics, sensors, and photonic devices. Although conventional silicon-based nanofabrication (top-down approach) has developed into a technique with extremely high precision and integration density, nanofabrication based on directed assembly (bottom-up approach) is attracting more interest recently owing to its low cost and the advantages of additive manufacturing. Directed assembly is a process that utilizes external fields to directly interact with nanoelements (nanoparticles, 2D nanomaterials, nanotubes, nanowires, etc.) and drive the nanoelements to site-selectively assemble in patterned areas on substrates to form functional structures. Directed assembly processes can be divided into four different categories depending on the external fields: electric field-directed assembly, fluidic flow-directed assembly, magnetic field-directed assembly, and optical field-directed assembly. In this review, we summarize recent progress utilizing these four processes and address how these directed assembly processes harness the external fields, the underlying mechanism of how the external fields interact with the nanoelements, and the advantages and drawbacks of utilizing each method. Finally, we discuss applications made using directed assembly and provide a perspective on the future developments and challenges.

KEYWORDS: *directed assembly, bottom-up fabrication, nanomaterials, nanotechnology, nanoelectronics, microelectronics, electrophoresis, dielectrophoresis, magnetophoresis, fluidic assembly*
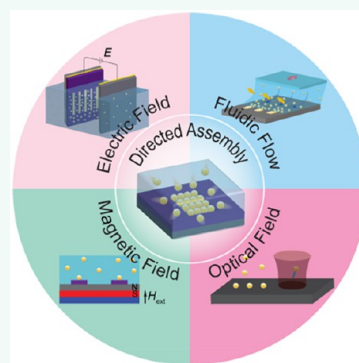
For the past three decades, nanofabrication has been an effective and efficient approach to manufacture one-, two-, or three-dimensional (1D, 2D, or 3D) functional nanostructures.[1−3] These nanostructures have at least one dimension <100 nm and can be used for a variety of applications in many fields such as electronics,[4−8] photonics,[9−11] energy,[12,13] biology,[14−18] and medicine.[19−22] In the broadest terms, nanofabrication techniques can be categorized into two distinct approaches, namely top-down and bottom-up (Figure 1).[23−25] The top-down approach employs physical (photons,[26,27] electrons,[28] ions,[29,30] etc.) or chemical (acids, bases, etc.) means to reduce a base material to nanoscopic dimensions.[24] It has been widely adopted by the semiconductor industry to manufacture integrated circuits for consumer electronics. To keep pace with Moore's Law,[31,32] which states that the number of transistors doubles every two years, silicon-based nanofabrication has evolved into a manufacturing technology with extremely high precision (feature size down to 3 nm) and integration density (around two hundred million transistors per square millimeter).[33] While having experienced massive success for six decades, top-down nanofabrication has become increasingly expensive and complex with hundreds of process steps and capital intensive, employing state-of-the-art fabrication facilities which can cost upward of $20 billion[34] each. Furthermore, the top-down fabrication is intrinsically subtractive in nature,[35] requiring a high consumption of materials and adding substantial costs to the fabrication process. Considering the ultrahigh resolution and level of integration needed, the high system complexity and high fabrication and operating cost, the application of top-down nanofabrication works well but at an extremely high cost and limited versatility in the materials that could be used in the manufactured devices.
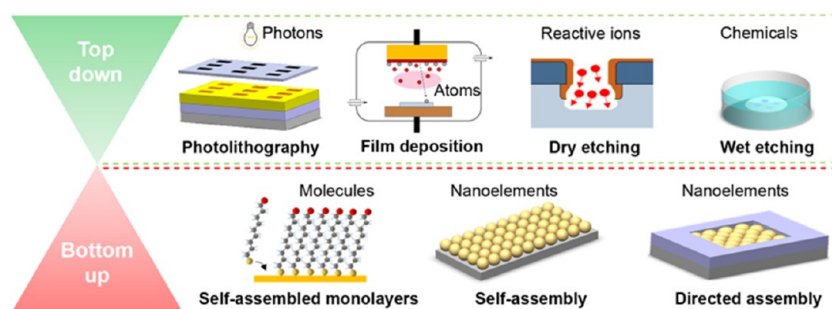
In contrast, bottom-up methods are intrinsically additive and can typically be employed at a much lower cost and thus have
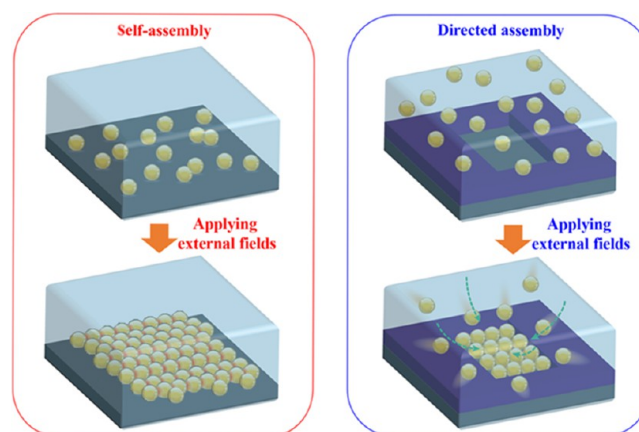
Figure 1. Schematic illustration of the top-down and bottom-up nanofabrication methods. The top-down method employs physical (photons, electrons, ions, reactive ions, etc.) or chemical (acids, bases, etc.) means of lithography, etching, and deposition. The bottom-up method constructs nanoscale architectures through self-assembly or directed assembly of basic building blocks such as atoms, molecules, and nanoelements.

attracted great attention in recent years. Inspired by the formation of complex and multilevel structures and systems (snowflakes, DNA, proteins, lipid bilayers, etc.) in nature, bottom-up fabrication constructs nanoscale architectures through self-assembly[36−39] of basic building blocks such as atoms,[40,41] molecules (DNA,[42] block copolymers,[43,44] etc.) and nanoelements[45] (nanoparticles, 2D nanomaterials, nanotubes, nanowires, etc.). During self-assembly, disordered building blocks spontaneously assemble into ordered structures via interelement interactions driven by the minimization of free energy.[46] The spontaneous self-assembly relies heavily on the interelement interactions. Because these interactions are inherently short-range and rather weak,[47−49] close-packed periodic structures with short-range ordering are typically obtained.[50,51] For instance, colloidal nanospheres tend to self-assemble into hexagonally close packed (hcp) or cubic close packed (ccp) structures.[52,53] Unfortunately, the assembled colloidal crystal structures often result in a very small domain size of a few micrometers to tens of micrometers and contain local disorder.[54−57] Another example is block copolymers that consist of two or more chemically distinct polymer blocks which are likely to self-assemble into phase-separated microdomains with periods of 3−50 nm.[58−61] The microdomains lack long-range order and typically exhibit fingerprint patterns.[62] Although the aforementioned periodic nanostructures show promise in diverse fields such as nanophotonics, solar cells, catalysts, and data storage,[63−65] their application in functional devices would be greatly improved if long-range ordering could be achieved. In addition, because of the weak interelement interactions, self-assembly is usually conducted under specific and stringent conditions to avoid any disturbances. As an example, atomic self-assembly based epitaxial film growth always takes place in ultrahigh vacuum (10^{-8}−10^{-12} Torr) to avoid collision between atoms and gases in the chamber. The lattice constant of substrates should match the interatomic distance of the films to be deposited to avoid defects like lattice distortion. Besides short-range ordering, another deficiency of self-assembly is that it is always nonselective which is undesirable when making electronic devices where selective assembly in specific areas is a necessity.

To address the short-range ordering issue of self-assembly, it is crucial to enhance the interelement interactions. Directed self-assembly has emerged as an obvious approach to realize this and it has studied intensively in the past two decades.[66,67] The directed self-assembly process relies on the manipulation of the assembly elements by applying external directing fields (electric, fluidic, magnetic, etc.). For example, in the presence of an electric field, nanoparticles become polarized because their permittivity is mismatched to their surrounding medium, inducing dipoles across the nanoparticles.[68−70] The adjacent dipoles tend to attract one another head-to-tail, which results in enhanced interaction between nanoparticles and thus long-range ordering for assembled nanostructures. Similarly, a magnetic field enhances the interelement interactions through induced magnetic dipole−dipole interactions.[71−74] Utilizing directing templates with chemically or physically (static charges, etc.) functionalized pattern areas provides a powerful means to accomplish selective self-assembly.[75,76] The pattern areas are typically designed to interact with nanoelements to enable their site-specific deposition. By defining the design of the pattern areas, template-assisted directed self-assembly enables the fabrication of arbitrarily shaped patterns.

While directed self-assembly has been the subject of numerous reviews,[36,39,48,53,66,67,75−78] almost all the work reviewed, as discussed previously, focuses on employing external fields or templates to enhance interelement interactions or introduce element-template interactions in order to accomplish self-assembly of nanoelements into ordered structures (Figure 2). Besides enhancing interelement interactions, the external fields also directly interact with nanoelements as driving forces

Figure 2. Schematic illustration of the self-assembly and directed assembly processes. During the directed self-assembly process, external fields are exerted to enhance interparticle interactions and assist particles to assemble into long-range ordered structures, while the directed assembly process utilizes external fields to directly interact with particles and drive the particles to site-selectively assemble in predefined pattern areas on substrates to form functional structures.

to direct the nanoelements to assemble at specific locations on substrates. In this case, obtaining ordered structures is no longer the focus, but rather the focus is on using nanoelements as building blocks for the fabrication of functional structures. In many cases, massive nanoelements without a certain order are assembled.[79−82] In other cases, the assembled nanoelements even fuse into solid structures.[83−85] There has been a dearth of relevant review in this field, which motivated this current work. However, it should be noted that the difference between directed self-assembly and directed assembly is subtle. The directed self-assembly relies on self-assembly on a surface, during which external fields are applied to drive nanoelements to the substrate where short-range interelement interactions create ordered structures, while directed assembly utilizes external fields to direct nanoelements to site-selectively assemble onto a patterned substrate to create functional structures. In other words, directed assembly consists of two steps, the first is to create a functionalized substrate where 2D or 3D patterns are created, and the second step is the application of an external field to direct particles to assemble only onto or into these patterns.

Directed assembly has been developed into a potentially powerful tool for the fabrication of electronics and sensors.[81,86−89] In the directed assembly process, external fields such as electric,[90−97] magnetic,[98−105] optical,[106−108] and fluid flow[109−112] are applied to nanoelements to generate driving forces that direct the nanoelements to target substrates that, when combined with lithography techniques for substrate functionalization, allows site-selective fabrication of functional structures (Figure 3).

In this review, we summarize recent progress in directed assembly of diverse nanoelements under various external forces such as electric fields, fluidic flow, magnetic fields, and optical fields. The application and control of the external fields and the underlying mechanism of how these fields interact with the nanoelements will be the main focus of this review. In addition,

the advantages and disadvantages of utilizing each external field will be discussed. The scope of this review is restricted to processes that combine top-down lithography (when necessary) and directed assembly for the purpose of realizing the area-selective arrangement of nanoelements into functional structures. Some of the methods reviewed here do not require the use of lithography. In the following sections, we will discuss how to generate and control the external fields and how the external fields interact with the nanoelements in each directed assembly approach. Following this, some devices fabricated by directed assembly will be introduced. Finally, perspectives on the future developments and challenges facing the directed assembly process will be discussed. At the end of the main text, tables summarizing the main directed assembly methods, and selected references are tabulated for each method showing the types of materials used, the experimental parameters, and the application if mentioned in the reference. The tables are not exhaustive, but instead aim to highlight more recent works to show the typical materials and parameters used for assembly.

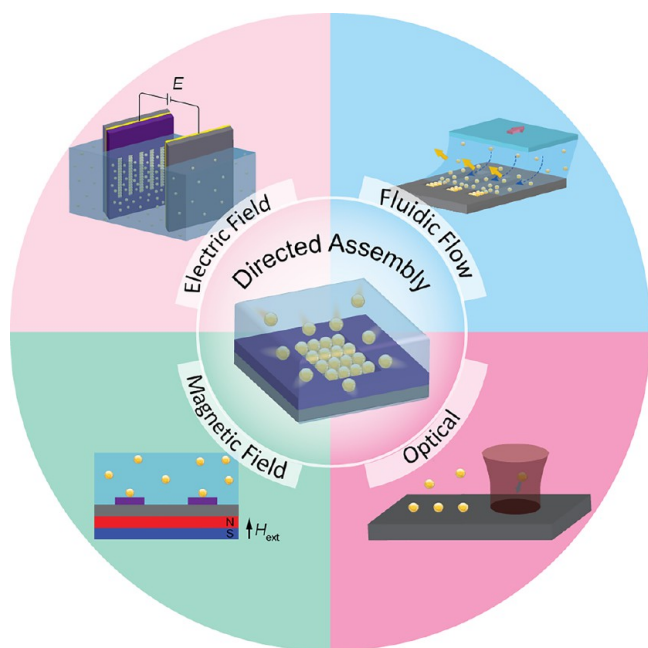## ELECTRIC FIELD-DIRECTED ASSEMBLY

Electrophoretic-Directed Assembly. Nanoparticles suspended in a liquid medium tend to acquire surface charges caused either by ionization of surface groups, adsorption of charged species (ions and ionic surfactants) or chemical functionalization of the nanoparticle.[113,114] When an electric potential is applied within a suspension of charged nanoparticles, the nanoparticles will be attracted toward the electrode of the opposite charge by the coulomb force, resulting in a migration of nanoparticles known as electrophoresis (EP) (Figure 4a). Extensive research[113,115,116] has been conducted using the EP force to assemble ceramic,[117−119] polymer,[120] metallic,[121,122] and semiconducting[123] nanoparticles into films for broad areas of applications, including light-emitting devices,[124] supercapacitors,[125] solar cells,[126] and sensors.[127] Using patterned substrates, site-specific assembly of nanoparticles into functional structures can be achieved as shown in Figure 4b,c for the case of polystyrene latex (PSL) particles.[128−132] The patterns can be made using photoresist or some other dielectric layer on a conductive substrate, allowing the nanoparticles to assemble only in the patterned region when an electric field is applied.

During the EP assembly process, the magnitude of EP force exerted on a nanoparticle is given by

$$F_{EP} = QE \qquad (1)$$

where Q is the effective surface charge of the nanoparticle, and E is the strength of the electric field. It should be noted that the effective surface charge of the nanoparticle is different from the surface charge mentioned above. The effective surface charge depends on the solvent, pH, and the ionic strength of the suspension. Charged nanoparticles in a liquid medium are always surrounded by a cloud of ions with an opposite charge (counterions). This cloud of ions surrounding a particle will reduce the electrostatic force between particles, leading to a decrease of the effective surface charge. This attenuation of the force between particles due to other ions is known as screening and has important implications for the stability of colloids and the solubility of ions.

The electrostatic forces involved in colloidal stability can be described using the Derjaguin−Landau−Verwey−Overbeek theory.[129,131] At the surface of a charged particle in solution, there is a dense layer of counterions called the Stern layer where

Figure 3. Schematic illustration of diverse directed assembly processes: electric field-directed assembly, magnetic field-directed assembly, optical field-directed assembly, and fluidic flow directed assembly.
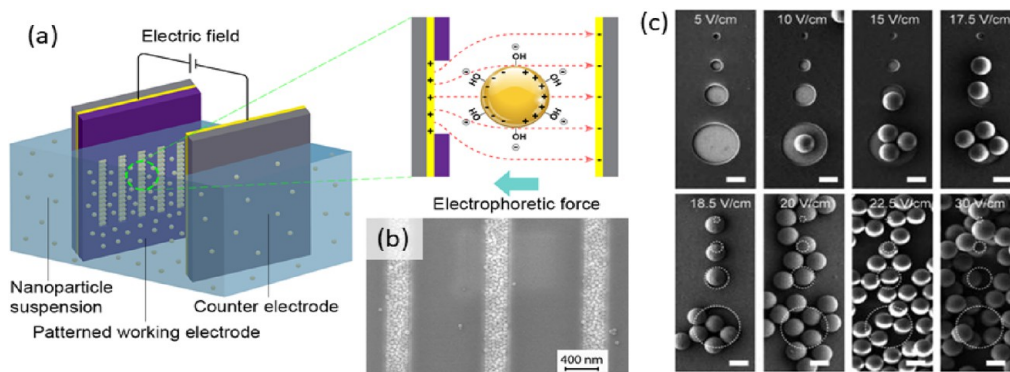
Figure 4. (a) Schematic illustration of EP assembly. (b) 50 nm PSL particles in 260 nm wide trenches. Reprinted with permission from ref 129. Copyright 2006, AIP Publishing. (c) PSL microparticles assembled as a function of field strength. Reprinted with permission from ref 133. Copyright 2015, American Chemical Society.

the ions are considered immobilized and move with the particle. Beyond this is the "diffuse layer" composed mostly of counterions. These two layers of ions form the "double layer" and its thickness depends on the concentration of ions in the solution. The thickness of the double layer is characterized by the Debye length (κ^{-1}) or the point at which the surface charge has decreased by a factor of the natural logarithm e. The molecules of the liquid medium within the diffuse layer are assumed to move along with the particle where the outer boundary is defined by the slipping plane. It is the potential measured at this slipping plane that is known as the zeta potential (ζ), which is typically used to characterize the surface charge of a particle. The effective surface charge of the nanoparticle can be calculated based on the simplified Debye−Hückel approximation as

$$Q = 4\pi R\varepsilon_m(1 + \kappa R)\zeta \tag{2}$$

$$\kappa^{-1} = \sqrt{\frac{\varepsilon_m k_B T}{2N_A e^2 I}} \tag{3}$$

where ε_m is the dielectric constant (permittivity) of the medium, k_B is the Boltzmann constant, T is the temperature, N_A is Avogadro's number, e is the elementary charge, I is the ionic strength of the electrolyte, and R is the radius of the nanoparticle. The ζ potential quantifies the effective surface charge of the nanoparticle and can be determined by measuring the electrophoretic mobility μ of the particle experimentally and then applying the Henry equation:[114,134]

$$\mu = \frac{\nu}{E} = \frac{2}{3}\frac{\varepsilon_m \zeta}{\eta} f(\kappa R) \tag{4}$$

where ν is the velocity of the nanoparticle, η is the viscosity of the medium, and $f(\kappa R)$ is the Henry's function. The Henry equation can be simplified as the Hückel equation:

$$\mu = \frac{2}{3}\frac{\varepsilon_m \zeta}{\eta} \quad (\kappa R \ll 1) \tag{5}$$

or the Smoluchowski equation:

$$\mu = \frac{\varepsilon_m \zeta}{\eta} \quad (\kappa R \gg 1) \tag{6}$$

depending on the nanoparticle radius and the Debye length. For nanoparticles suspended in a polar environment, a large ζ potential will ensure their stability. Typically, a ζ potential

greater than 40 mV in magnitude is desirable for well suspended nanoparticles. A low ζ potential will result in faster agglomeration and consequently precipitation of the suspended particles.

Based on the discussion above, increasing the effective surface charge and the electric field strength is the key to increase the EP force and thus the assembly rate. Qian et al.[133] investigated the effect of the electric field strength on the assembly of PSL microparticles (2 μm in diameter). At a low field strength of 5 V cm^{-1}, no PSL particles were assembled, as seen in Figure 4c. With the increase of the field strength, PSL particles started assembling within the patterned circles. Until a field strength of 18.5 V cm^{-1} was reached, patterns with diameters from 500 nm to 5 μm were fully filled with PSL particles. Upon further increasing the field strength, over assembly of PSL particles was observed where a significant number of particles were deposited outside of the intended area. Yilmaz et al.[122] and Xiong et al.[129] reported a similar trend when they assembled PSL and silica nanoparticles. Xiong was able to assemble single file lines of 15 nm silica nanoparticles in 30 nm wide trenches using 2 V bias. Although the applied voltage is relatively low, modeling showed the effective potential above the patterned trenches to be 200−300 V m^{-1}, and even as high as 3000−4000 V m^{-1} at a position 15−20 μm from the conductive surface of the pattern. Yilmaz et al. varied the potential from 2 to 5 V where the lowest voltage resulted in poor coverage of particles. Coverage increased with voltage until 100% coverage was achieved at 3.4 V. However, for higher voltages, over assembly occurred where particles were deposited outside of the patterned areas.

Yilmaz carried out further modeling of the velocity and path of a particle as a function of particle size when exposed to an electric field in proximity of the patterned electrode area.[135] The velocity of the particle in suspension can be found using the Langevin equation:

$$\frac{dv_p}{dt} = \frac{3}{2d(2S+1)}\frac{C_d}{C_c}W_r(v_f - v_p) - \left(1 - \frac{1}{S}\right)g\delta + n(t) + \frac{qE}{m} \tag{7}$$

where C_d is the drag coefficient, C_c is the Stokes−Cunningham slip correction, v_p and v_f are particle and fluid velocity, respectively, S is the ratio of particle to fluid density, d is the particle diameter, $n(t)$ is the Brownian diffusivity, q is the charge of the particle, E is the magnitude of the electric field, and m is the particle mass. By solving this equation numerically, the velocity of a 50 nm PSL particle located 20 and 150 μm from the
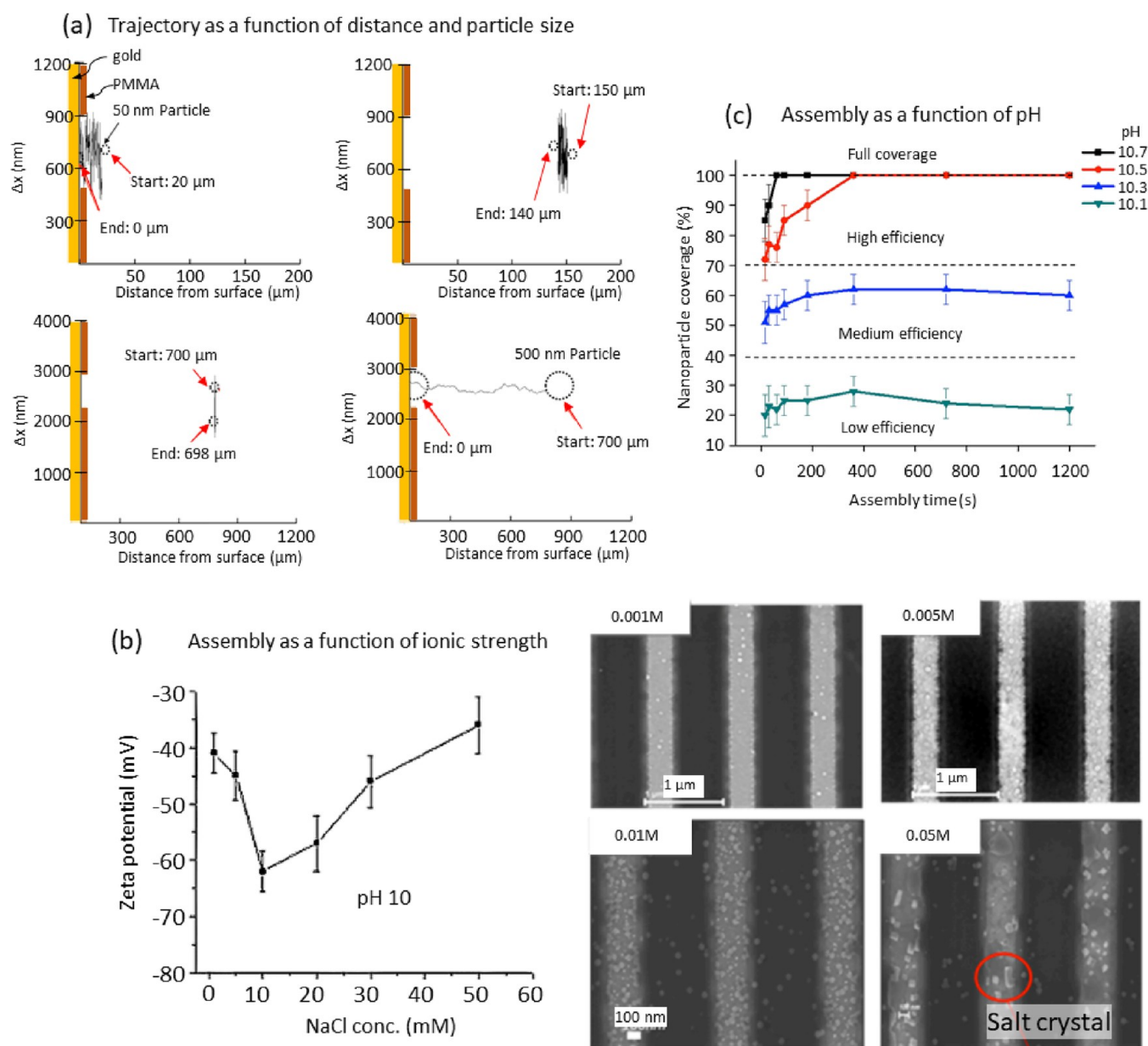
Figure 5. (a) Simulation of the trajectory of 50 and 500 nm PSL particles as a function of distance from the electrode surface. The effects of Brownian motion are much more significant for the assembly of the smaller particles. (b) Assembly as a function of ionic strength. When the concentration becomes too great, the screening effect results in lower charge and less assembly. (c) Assembly as a function of pH for 50 nm PSL particles. Below a certain pH threshold, full assembly would not occur even for extended times.[135]

electrode surface was found to be 850 $\mu m\ s^{-1}$ and 160 $\mu m\ s^{-1}$, respectively, when 2 V was simulated at pH 10.1. The greater velocity near the surface is due to the higher field strength (Figure 5a). The closer PSL particle reached the surface in 25 ms while the further particle only moved 10 μm after 50 ms. A third particle placed at 700 μm from the surface only oscillated around the starting point and did not approach the surface. These simulations show the importance of Brownian motion for particles at the nanoscale. The velocity due to Brownian motion of a 50 nm particle was calculated to be 886 $\mu m\ s^{-1}$, which is comparable to the velocity due to the EP force when the particle is close to the electrode surface. However, when it is farther away from the surface, the Brownian motion dominates, preventing small particles from approaching the surface when a field is applied. This modeling was repeated for a 500 nm PSL particle where even at a farther distance of 700 μm from the electrode

surface, the 500 nm particle was able to reach the surface in 0.01 s, due to a much weaker effect of Brownian motion on the larger particle.

Organic solvents (ethanol, propanol, butanol, etc.) and water are commonly used for EP assembly. The organic solvents typically have a low dielectric constant below 25, while water has a high dielectric constant of 80. Because a solvent with a high dielectric constant has a high dissociative power, nanoparticles dispersed in water tend to have high surface charge[117] and thus are more appropriate to be used in the EP assembly process. The pH influences the effective surface charge of the nanoparticle by affecting the ionization of the surface groups.[136−138] For a negatively charged nanoparticle, when the solution pH decreases, the ionization of the surface groups is prone to be suppressed, resulting in a less negatively charged surface. At a certain pH value known as the isoelectric point or IEP, the
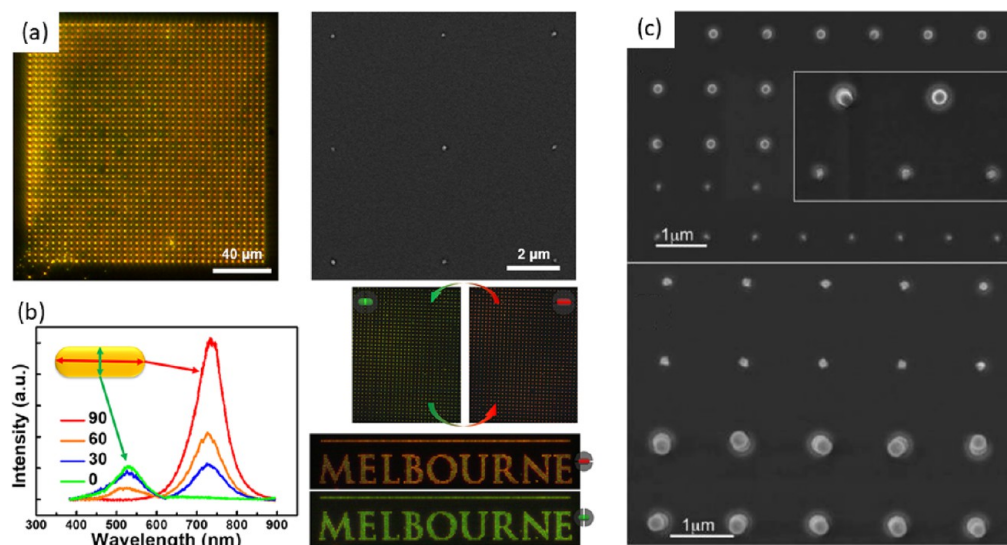
Figure 6. (a) Dark-field image of 110 nm gold nanospheres assembled by EP in a 40 × 40 array. Inset is an SEM image of nine assembled nanospheres. Reprinted with permission from ref 130. Copyright 2018, American Chemical Society. (b) Scattering spectra of a gold nanorod at different polarization angles and dark-field images of assembled gold nanorod arrays under 0° and 90° polarization. Reprinted with permission from ref 130. Copyright 2018, American Chemical Society. (c) EP assembly of 200 and 100 nm PSL nanoparticles in 210 and 110 nm circles, respectively (top); EP assembly of 200 and 50 nm PSL nanoparticles in 225 and 100 nm circles (bottom). Reprinted with permission from ref 131. Copyright 2011, American Chemical Society.

surface charge will be neutralized. Further decreasing the pH will lead to a buildup of positive H^+ groups on the particle surface. Conversely, for a positively charged nanoparticle, increasing and decreasing the pH will cause decrease and increase of the surface charge, respectively. This was demonstrated by Yilmaz et al.[122] who adjusted the pH of a PSL nanoparticle suspension by adding ammonium hydroxide solution. When the pH of the suspension was increased from 9.6 to 11.1, the surface charge per nanoparticle increased from 1.5×10^{-17} C to 2.4×10^{-16} C which also increased the assembly yield from ∼20% to 95%.

The ionic strength determines to what extent the surface charge is screened by the counterions.[134] The surface charge is more effectively screened with higher ionic strength, leading to a lower effective surface charge. As a result, the repulsive interactions between nanoparticles is also decreased, causing agglomeration of nanoparticles.[137−139] This is illustrated for the case of EP assembly in previous work.[135] The pH of a PSL suspension was held constant at 10.1 while the ionic strength was adjusted by adding NaCl up to a maximum concentration of 0.05 M. The magnitude of the ζ potential increased to a maximum of 63 mV with a salt concentration of 0.01 M. This resulted in the best coverage of assembled particles, although there were also particles deposited outside of the desired pattern. For NaCl concentrations greater than 0.01 M, the ζ potential decreased, and the highest concentration of 0.05 M caused salt crystals to form during the deposition process (Figure 5b).

Besides the aforementioned parameters, the EP assembly process can be controlled by the nanoparticle concentration and the assembly time. The influence of these two parameters on the EP assembly process is comparatively straightforward. When increasing the nanoparticle concentration and the assembly time, either more nanoparticles are driven toward the substrate by the EP force at a constant time or the time spent for the particle assembly is prolonged, leading to increased assembly yield. It should be noted that the assembly yield does not always increase with the assembly time. Instead, the yield may plateau over time. The plateau phenomenon has been attributed to the

decrease of the nanoparticle concentration and the effective electric field during the assembly process.[116] Barbee et al.[140] found that full assembly could not be achieved with a single batch of 0.5 μm microparticle suspension even though there were still plenty of particles left in the suspension. They attributed this to the depletion of buffer as 100% assembly could be realized using an additional batch of microparticles. Tiwari et al.[141] present a different view on the plateau phenomenon. They reported that the local pH near the substrate changed during the EP assembly process due to the loss of hydrogen ions through the formation of H_2 gas at the negative electrode. This decreased the effective surface charge on the nanoparticle surface and caused cessation of the assembly after ∼30 min of deposition. The plateau of assembly versus time was also found in our previous work and was a function of pH.[135] When using 50 nm PSL particles, a threshold pH exists below which complete particle coverage is not possible, even with extended deposition times (Figure 5c). This is due to Brownian motion dominating the small particles when the pH is low, as mentioned previously regarding the ionic strength. Since the electrophoretic velocity of the small particles was low at pH of 10.1 and 10.3, the nanoparticles failed to assemble even at longer assembly times.

When combined with predefined nanoscale patterns, EP assembly allows positioning of single nanoparticles with nanoscale precision within a few seconds. Employing box cavities with dimensions 10% larger than the particle size, Zhang et al.[130] assembled individual 110 nm gold nanospheres into a plasmonic pixel array. The array scattered uniform yellowish light with minimal defect sites, as shown in Figure 6a, demonstrating the reliability of the assembly process. Besides gold nanospheres, Zhang et al.[130] also assembled 100 nm × 40 nm gold nanorods using the EP assembly process. Possessing an anisotropic shape, the optical properties of the nanorods are anisotropic and polarization angle dependent. When the polarization direction is orthogonal to the major axis of the gold nanorods (polarization angle 0°), the transverse surface plasmon oscillation dominates and the assembled nanorods
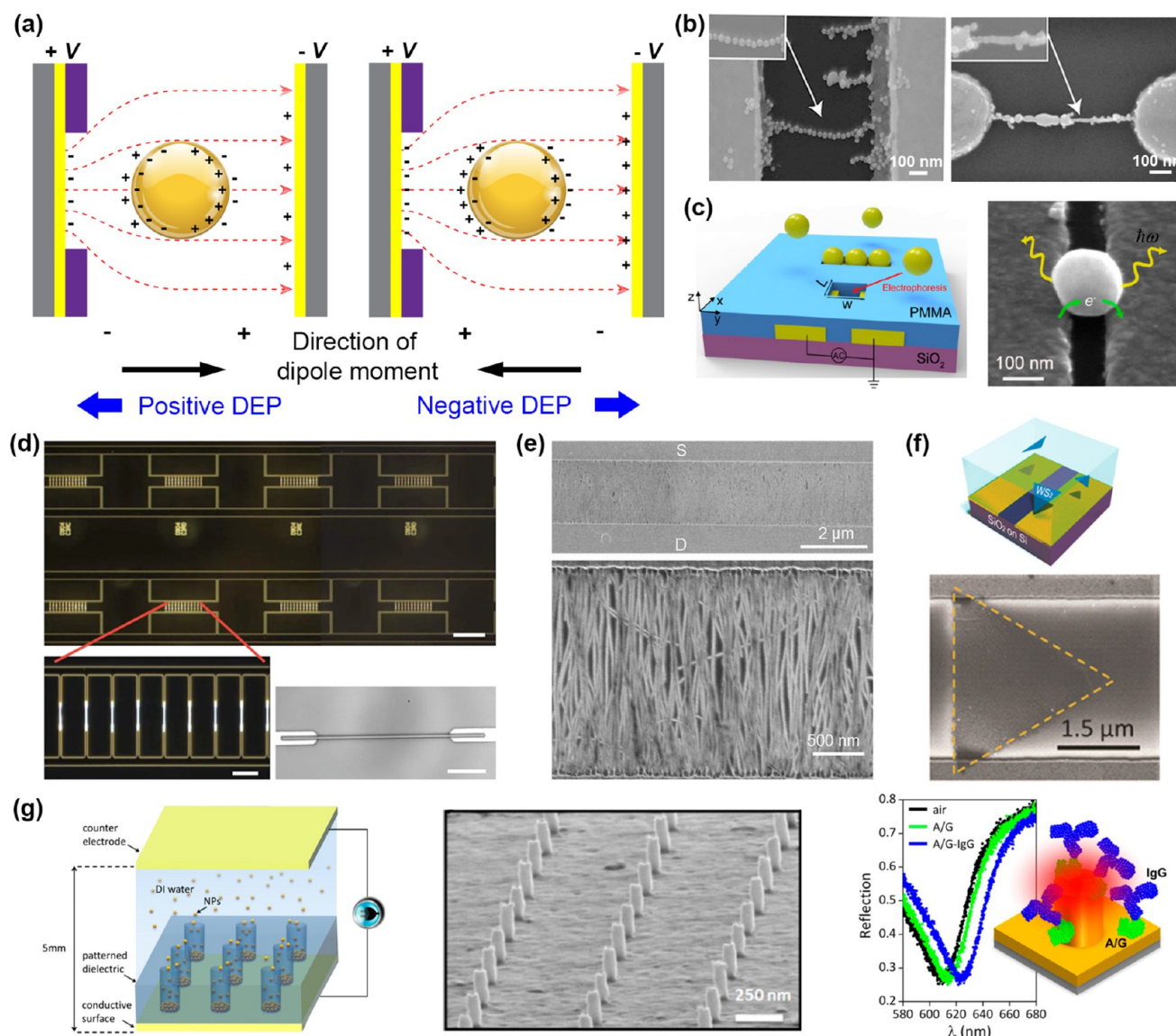
Figure 7. (a) Schematic illustration of the DEP assembly process. A nanoparticle with a higher (left) or lower (right) polarizability than the surrounding medium is polarized under an nonuniform electric field, inducing a dipole aligning with or opposite to the electric field and causing a positive or negative DEP force, respectively. (b) DEP assembly of gold nanoparticles between two planar electrodes into a pearl chain (left) and a fused nanowire (right). Reprinted with permission from ref 164. Copyright 2004, American Chemical Society. (c) Assembly of single thiol-coated gold nanoparticle for the application of electrically driven optical antenna. Reprinted with permission from ref 90. Copyright 2019, American Chemical Society. (d) Silicon nanowire assembly on eight 10-finger electrode arrays. Single nanowire was centered between two electrodes with submicrometer alignment precision. Reprinted with permission from ref 195. Copyright 2010, Nature Publishing Group. (e) DEP assembly of aligned CNTs with an ultrahigh density of 30 SWCNTs μm^{-1}. Reprinted with permission from ref 203. Copyright 2011, American Chemical Society. (f) DEP assembly of WS$_2$ sheets with one of the triangle sides perpendicular to the electrode edge. Reprinted with permission from ref 204. Copyright 2016, American Chemical Society. (g) Schematic illustration of the parallel plate setup used for the DEP assembly of 3D nanostructures (left). SEM image of DEP assembled gold nanorods (middle). Sensing of A/G and IgG proteins using the assembled gold nanorods (right). Reprinted with permission from ref 121. Copyright 2014, American Chemical Society.

appear green in color (Figure 6b). However, when the polarization direction is parallel to the major axis (polarization angle 90°), the longitudinal surface plasmon becomes dominant and the nanorods appear red. Besides positioning single nanoparticles, the confinement effect of prefabricated patterns can be utilized to sort nanoparticles with different sizes. Siavoshi et al.[131] patterned circles with different diameters and then assembled PSL nanoparticles (200, 100, and 50 nm) at designated sites. Larger nanoparticles were assembled first in the larger circles, which prevented the smaller nanoparticles from being assembled at the same sites. Then, smaller

nanoparticles were assembled in the smaller circles. By doing this, size-selective assembly of nanoparticles in sites of comparable sizes has been realized, as shown in Figure 6c.

Both direct current (DC) and alternating current (AC) fields have been utilized in the EP assembly process. One issue of using the DC field is that the maximum applicable field strength is limited. At a high electric field strength, an electrochemical reaction takes place (electrolysis), causing the formation of gas bubbles and damage to the assembled structures and even the electrodes.[142−144] However, utilizing a low field strength is undesirable in most situations because either the particle

assembly efficiency is limited or no particle assembly happens. To achieve high field strength, pulsed DC field or an asymmetric AC field is favorable.[144] Barbee et al.[140] assembled PSL microparticles using a pulsed DC field. The pulsed DC field permitted rapid assembly of the particles at a high voltage of 3 V without bubble formation because the amount of time in which the electrode and assembled structure were subject to the electric field was minimized. In the case of an AC field, the voltage that drives the electrochemical reaction is also applied to the double layer capacitance at the electrode−electrolyte interface.[142,143] When the frequency of the electric field is high enough, the impedance of the double layer capacitor decreases, resulting in the reduction of the driving voltage for the electrochemical reaction and therefore decreased bubble evolution. Under the AC field, nanoparticles periodically reverse their direction of motion and oscillate in the suspension. If the AC field is symmetric, the nanoparticles travel equal distance during each half cycle of the electric field. Therefore, no net movement of the nanoparticles occurs and in turn no nanoparticles are assembled on the electrodes. However, when the AC field is asymmetric, nanoparticles can travel a longer distance during one of the half cycles because the particle velocity does not have a linear dependence on the field strength,[143] causing net particle movement and thus particle assembly. Asymmetric AC fields have been used to non-selectively assemble nanoparticles into films.[142] Selective assembly of nanoparticles into predefined patterns under asymmetric AC field is rarely reported.

Dielectrophoretic-Directed Assembly. Besides the electrophoretic force, nanoparticles in suspension may also experience a dielectrophoretic (DEP) force.[145] The DEP force originates from polarized charge on the particle surface instead of static surface charge for the case of EP assembly. Basically, all matter polarizes when subjected to an electric field.[145] If the nanoparticles are more polarizable than the surrounding medium, the nanoparticles will possess more polarized charge than the medium at the particle/medium interface (Figure 7a), which gives rise to an induced dipole across the nanoparticles, aligning with the electric field. In a nonuniform electric field, the electric forces acting on the induced dipole are unbalanced. If the nanoparticles move toward the region where the electric field density is greater, it is referred to as a positive DEP force. If the nanoparticles are less polarizable than the medium, they will have less polarized charge and the induced dipole points in the opposite direction to the electric field (Figure 7a). Under these conditions, a nonuniform electric field will drive the nanoparticles toward the region where the electric field density is lower, which is referred to as a negative DEP force. The polarizability of a material depends on its conductivity and dielectric constant. Because a high conductivity or a high dielectric constant tends to result in a high polarizability, suspended metallic nanoparticles can be easily polarized and thus often experience a positive DEP force and move toward the high electric field region.[146] It has been reported that insulating nanoparticles also experience a positive DEP response. Even though the insulating nanoparticles have a low bulk conductivity, they always carry surface charge in the suspension, which gives rise to a surface conductance.[147−153] Because of the surface conductance, the insulating nanoparticles become highly polarizable, resulting in the positive DEP response.

The DEP force acting on a nanoparticle as a function of the conductivity, the dielectric constant, and the frequency is given by[154]

$$F_{DEP} = 2\pi\varepsilon_m \text{Re}|K(\omega)|R^3\nabla(E^2) \tag{8}$$

$$\text{Re}|K(\omega)| = \frac{\varepsilon_p - \varepsilon_m}{\varepsilon_p + 2\varepsilon_m} + \frac{3(\varepsilon_m\sigma_p - \varepsilon_p\sigma_m)}{\tau_{MW}(\sigma_p + 2\sigma_m)^2(1 + \omega^2\tau_{MW}^2)} \tag{9}$$

$$\tau_{MW} = \frac{\varepsilon_p + 2\varepsilon_m}{\sigma_p + 2\sigma_m} \tag{10}$$

where ε_m and σ_m are the dielectric constant and the conductivity of the medium, and ε_p and σ_p are the dielectric constant and the conductivity of the nanoparticle, $K(\omega)$ is the Clausius−Mossotti factor with $\text{Re}|K(\omega)|$ as its real part, ω is the frequency of the AC field, R is the radius of the nanoparticle, and $\nabla(E^2)$ is the gradient of the square of the electric field.

Like the EP phenomenon, DEP occurs in DC and AC fields, as long as the fields are nonuniform. However, since the field strength needs to be very high to generate sufficient DEP force, the DC field is seldom used in DEP assembly due to undesirable effects such as water electrolysis.[146] This is especially true for small particles since the DEP force is proportional to the volume of the particle, as shown in eq 8. For small particles, a significant DEP force can only be had by increasing the magnitude of the applied electric field, which can lead to issues related to Joule heating. Local heating caused by a nonuniform AC field causes variations in the conductivity and permittivity of the liquid medium, which gives rise to additional forces in the form of electrothermal flows acting on the particles.[155,156] The electrothermal flows can also be used for particle assembly and is discussed later.

When applying the AC field, there is a significant difference in particle motion between the EP process and the DEP process. For the EP process, nanoparticles reverse their direction of motion when alternating the field polarity, causing an oscillating motion. While for the DEP process, when the polarity of the field is reversed, the distribution of the induced charge will be reversed as well, resulting in a dipole in the same relative direction with respect to the field and a constant moving direction of the nanoparticles. Consequently, the independence of the field polarity is an important characteristic of the DEP process distinctly different from the EP process.

Besides the conductivity and the dielectric constant, the polarizability of a material is also dependent on the frequency of the AC field.[157−159] At a low frequency, the polarization of a material arises from field-induced redistribution of the free charge in the material and therefore is dominated by the material conductivity. A high conductivity gives a high polarizability, although the redistribution of the free charge is not instantaneous. It typically ranges from picoseconds to a few microseconds, depending on the material conductivity.[157] With the increase of the AC frequency, there comes a point where the movement of the free charge cannot keep pace with the field alternation. As the frequency further increases, the contribution of the free charge movement to the polarization of a material becomes negligible. Instead, the polarization of bound charge becomes dominant. In this case, a material with a high dielectric constant possesses a high polarizability. Because of the frequency-dependent polarizability, nanoparticles may experience a varying DEP force over a wide frequency range. For example, considering nanoparticles with a high conductivity and a low dielectric constant dispersed in a medium of a low conductivity and a high dielectric constant, at a low frequency,

the nanoparticles experience a positive DEP force because of their high conductivity, while at a high frequency, the nanoparticles experience a negative DEP force due to their low dielectric constant. The frequency at which a particle experiences no force from the AC field is known as the crossover frequency and is dependent on the dielectric properties of the particle and medium.[148]

One application of the DEP phenomenon is the assembly of various nanoparticles (metallic[160] or semiconducting[79,80]) between two planar electrodes into pearl chains[161] or micro/nanowires.[85,162] As a consequence of the fringing field effect, the electric field strength is always high in the vicinity of the electrode edges.[163] Under a positive DEP force, nanoparticles assemble simultaneously from the opposing electrode edges with the highest electric field intensity and finally meet at the center of the electrode gap, forming a pearl chain structure (Figure 7b).[161,164] Two mechanisms may contribute to the formation of the pearl chain: (i) nanoparticles chain together away from the electrodes under a pearl-chaining force and then move toward the electrodes due to the DEP force,[161] and (ii) nanoparticles assemble directly at the electrodes under the DEP force and then continually assemble at the front tip of the growing chain.[165] The pearl-chaining force (F_{chain}) arises from the interactions of induced dipoles between two adjacent nanoparticles[166,167] and can be calculated by[146]

$$F_{chain} = -C\pi\varepsilon_m \text{Re} |K(\omega)|^2 R^2 E^2 \tag{11}$$

where the coefficient C ranges from 3 to >1000 depending on the distance between adjacent nanoparticles and length of the chain. However, the chaining force is even weaker than the DEP force. In order to generate a large enough chaining force to overcome the repulsive electrostatic interaction between nanoparticles, the electric field strength should exceed a threshold value (E_{th}):[161]

$$E_{th} = 1.7 \frac{1}{\text{Re}|K(\omega)|} \sqrt{\frac{k_B T}{\varepsilon_p R^3}} \tag{12}$$

where k_B is the Boltzmann constant and T is the temperature. As reported previously, for gold nanoparticles 15 nm in diameter, E_{th} is as high as 56 V μm^{-1}.[168] This high electric field strength is unlikely to be available away from the electrodes under usual DEP conditions. Therefore, in the case of nanoparticle assembly, the chaining force may not be the main force for the formation of the pearl chain. However, the threshold electric field strength is inversely proportional to the diameter of the particle, as indicated in eq 12. When the particle diameter is increased by 100 times, the threshold electric field strength will decrease by a factor of 10^3, implying the possibility of utilizing the chaining force to assemble microparticles. In fact, the assembly of microparticles into 1D pearl chains and eventually 2D crystals under the assistance of the chaining force has been reported.[169,170] Apart from utilizing the chaining force, nanoparticles can be assembled directly on the electrodes under the DEP force. Once nanoparticles are assembled, they become part of the electrode. The tip of the assembled nanoparticles distorts the electric field distribution between the electrodes and creates a high electric field in the local region around the terminal nanoparticle.[146] Nanoparticles in the suspension will be attracted toward the tip of the nanoparticle chain under the DEP force such that the chain builds in the direction of the field gradient until two chains from opposing electrodes meet at the center of the electrode gap. The assembly parameters should be

well controlled in order to avoid melting of the assembled nanoparticles.[164] However, under most conditions, the assembled nanoparticles melt due to the Joule heating, forming micro/nanowires (Figure 7b),[83,171] especially when relatively small nanoparticles or high voltage is used. Velev et al.[165,171] demonstrated how gold nanoparticles can be assembled into microwires of millimeter length. They found that the microwires assembled in two different modes, bulk assembly and surface assembly depending on the assembly parameters. At a high electric field strength, microwires tend to grow in the bulk mode and the assembly speed is high. Besides the electric field strength, other parameters, such as the frequency of the electric field, the particle size, the electrolyte concentration, and the viscosity and dielectric constant of the medium, can also affect the particle assembly. A larger particle size gives rise to a higher DEP force and thus a higher assembly speed. As the electrolyte suppresses the repulsive electrostatic interactions between nanoparticles, the assembly speed increases with the electrolyte concentration. Moreover, a high dielectric constant or a low viscosity leads to a rapid assembly. Due to the high polarizability of the gold nanoparticle, the real part of the Clausius−Mossotti factor can be taken as 1 (Re|$K(\omega)$| ≈ 1).[171] According to eq 8, the DEP force should be independent of the electric field frequency. However, the results demonstrated a frequency-dependent particle assembly process. The assembly speed decreases with the increasing frequency. The authors attributed this to the frequency-dependent polarization of counterions around the nanoparticles. Besides the free charge and surface charge, the counterions surrounding the charged nanoparticles also respond to and polarize under the applied electric field. Since the mobility of the counterions is relatively low, at a high frequency, the counterions cannot follow the alternation of the electric field, causing less polarization and less DEP force. As a result, the microwires grow slower at a higher frequency. The frequency-dependent gold microwire formation was also reported by Liu et al.[172] At a low frequency of 10 kHz, microwires start assembling from opposing electrodes but cannot bridge with each other, forming a channel-like structure with two parallel banks at the center of the electrode gap. Whereas, at a high frequency of 1 MHz, a thin nanowire 100 nm in diameter is assembled along the shortest distance between the electrodes. The authors ascribed this assembly behavior to frequency-dependent electric field-induced electrohydrodynamic flow. The detailed mechanism of the electrohydrodynamic flow will be discussed in the next section. When the size of the gap between electrodes is comparable to or smaller than the particle size, the DEP assembly process can be used to trap a single nanoparticle between the electrodes[161,173] for the application of single electron transistors.[174,175] He et al.[90] assembled single thiol-coated gold nanoparticles between two electrodes for the application of electrically driven optical antennas (Figure 7c). As the electrode gap shrinks to sub-10 nm, the electric field strength between the electrodes is strongly enhanced due to the fringing field effect, resulting in an increase of 2 orders of magnitude in the trapping force compared to the 1 μm gap when a voltage as low as several 100 mV is applied.[176] The ultralow voltage can mitigate the undesired effects such as heat generation, bubble formation, and electrochemical reactions that take place when applying high voltages.

Another typical application of the DEP phenomenon is aligning and assembling 1D materials[177] such as carbon nanotubes (CNTs),[178−185] metallic nanowires,[186−188] gallium arsenide (GaAs) nanowires,[189] gallium nitride (GaN) nano-
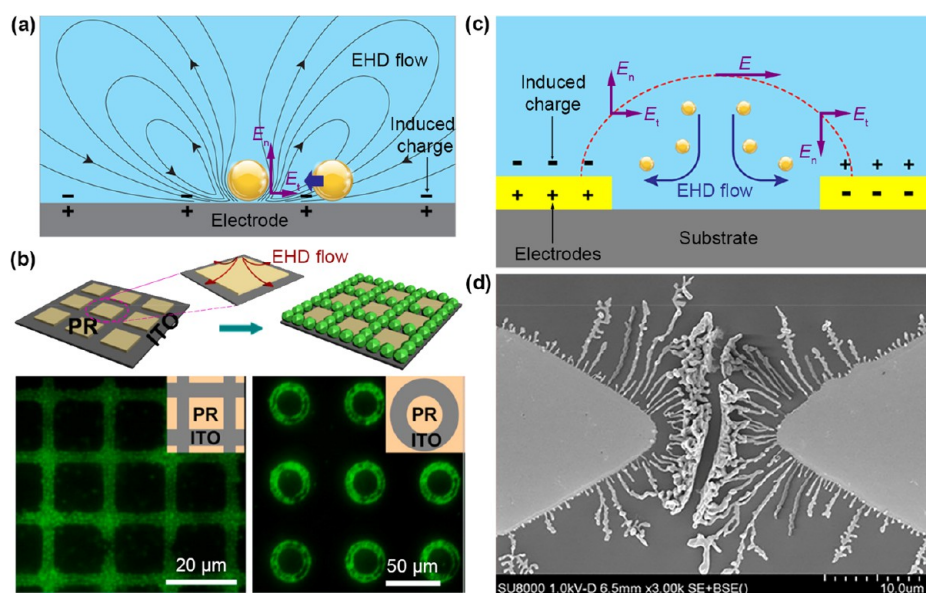
Figure 8. (a) Schematic illustration of the EHD flow that entrains a particle toward an assembled particle. The EHD flow arises from the interaction of a tangential electric field (E_t) with induced charge on the surface of an electrode. The streamlines show the pattern of the EHD flow. (b) EHD flow-directed assembly of TBPe crystals on patterned ITO substrates. Reprinted with permission from ref 234. Copyright 2014, American Chemical Society. (c) Schematic illustration of the EHD flow induced when utilizing the coplanar electrode setup. (d) EHD flow-directed assembly of gold nanoparticles into a channel-like structure. Reprinted with permission from ref 172. Copyright 2016, Elsevier.

wires,[190,191] indium arsenide (InAs) nanowires,[192] silicon nanowires,[193−195] manganese dioxide (MnO$_2$) nanowires,[196,197] nanofibers,[198] and biofunctionalized nanowires.[199] Unlike zero-dimensional (0D) nanoparticles, 1D materials experience an anisotropic DEP force, depending on their orientation in the electric field. When the 1D materials orient parallel to the electric field gradient, the DEP force can be given by the relation:[200]

$$F_{\text{DEP}\parallel} = c\varepsilon_m \text{Re}|K_\parallel(\omega)| \nabla(E^2) \tag{13}$$

$$K_\parallel(\omega) = \frac{\varepsilon_p^* - \varepsilon_m^*}{\varepsilon_m^*} \tag{14}$$

$$\varepsilon^* = \varepsilon - \frac{j\sigma}{\omega} \tag{15}$$

where c is a particle volume-related parameter, $\text{Re}|K_\parallel(\omega)|$ is the real part of the Clausius−Mossotti factor $(K_\parallel(\omega))$ along the major axis of the 1D material, ε_p^* and ε_m^* are the complex dielectric constant of the particle and the medium, respectively. Whereas when the 1D materials orient perpendicular to the electric field gradient, the DEP force needs to be modified as

$$F_{\text{DEP}\perp} = c\varepsilon_m \text{Re}|K_\perp(\omega)| \nabla(E^2) \tag{16}$$

$$K_\perp(\omega) = 2\frac{\varepsilon_p^* - \varepsilon_m^*}{\varepsilon_p^* + \varepsilon_m^*} \tag{17}$$

where $\text{Re}|K_\perp(\omega)|$ is the real part of the Clausius−Mossotti factor $(K_\perp(\omega))$ perpendicular to the major axis of the 1D material. The calculation results demonstrate that $K_\parallel(\omega)$ is orders of magnitude larger than $K_\perp(\omega)$,[200,201] implying that 1D materials mainly polarize along their major axis[202] and therefore $F_{\text{DEP}\parallel}$ is the determining force for their movement. In addition, the DEP force generates an electro-orientation torque on the 1D materials, aligning them along the direction of the electric

field,[179,180] where the torque becomes zero and the system's free energy is the lowest. The magnitude of the torque acting on 1D materials can be calculated as

$$T = F_{\text{DEP}\parallel} L \sin\theta \tag{18}$$

where L is the length of the 1D materials, and θ is the angle between the major axis of the 1D materials and the applied electric field. Raychaudhuri et al.[200] aligned and assembled individual InAs nanowires between two electrodes. The results indicate that the percentage of aligned nanowires first increases with the increasing frequency from 10 kHz to 1 MHz and then decreases as the frequency is further increased to 10 MHz. The initial increase in the aligned nanowires may be due to a reduced effect from the electrohydrodynamic flow, and the following reduction of the aligned nanowires may be attributed to the reduced DEP force. By balancing DEP, surface, and hydrodynamic forces, Freer et al.[195] precisely assembled aligned single silicon nanowires arrays at a high yield of 98.5%. Figure 7d shows the results on eight 10-finger electrode arrays. Single nanowires were centered between two electrodes with submicrometer alignment precision (average offset of 99 nm). Instead of aligning and assembling individual nanowires, Shekhar et al.[203] assembled ultrahigh density aligned CNT arrays with a density as high as 30 SWCNTs μm^{-1} (Figure 7e). Besides aligning 1D materials, the DEP phenomenon can be used to align 2D materials as well. Deng et al.[204] demonstrated assembly of triangular monolayer tungsten disulfide (WS$_2$) sheets and proved that the assembled WS$_2$ sheets displayed a preferential orientation with one of the triangle sides perpendicular to the electrode edge, as shown in Figure 7f.

In the applications mentioned above, coplanar electrodes are utilized, and the nanoelements assemble between the two electrodes on the same substrate. However, when the two electrodes are on separate substrates (such as a parallel plate setup), the nanoelements will assemble spatially in the bulk suspension. This phenomenon has been utilized to grow

complex 3D structures.[205−210] Yilmaz et al.[121] and Chai et al.[205] performed DEP assembly by applying an AC field between a patterned substrate and a counter electrode kept 5 mm apart, as illustrated in Figure 7g. The electric field strength is high around patterned regions due to the localized electric field, which generates a DEP force, attracting gold nanoparticles 5 nm in diameter to the patterned regions. The assembled gold nanoparticles fuse during the assembly process because of Joule heating, forming nanorods perpendicular to the substrates. The 3D gold nanorods exhibit a polycrystalline structure and possess an electrical conductivity that is equivalent to electroplated gold nanorods. Moreover, these gold nanorods possess a strong plasmon resonance and thus have great potential to be used in biosensing applications. Kim et al.[209] used a similar method to align single-walled carbon nanotubes (SWCNTs) vertically within a polymer template to form interconnects suitable for CMOS devices. In the work of Makaram et al.,[210] interconnects between electrodes separated in height by ∼700 nm were made through DEP of SWCNTs.

Electrokinetic Flow-Directed Assembly. In addition to the electrophoretic and the DEP forces, electrokinetic flows such as electroosmotic flow (EOF) and electrohydrodynamic (EHD) flow can also be employed for the assembly of nanoparticles.[211−214] EOF is a bulk liquid motion that results from the interaction of an electric field with counterions next to a charged surface. Since all the particles dispersed in a suspension possess surface charge with surrounding counterions, EOF can be generated when an electric field is applied. This flow has been utilized by Böhmer and Solomentsev et al.[215−217] to assemble ordered monolayer PSL microparticle crystals. The authors proposed a stepwise assembly mechanism. A particle is first adsorbed onto a substrate, creating an EOF in the surrounding fluid and carrying an opposite charge to the particle, the fluid is drawn away from the substrate and then circulates back to the substrate surface. When a second particle is in the vicinity of the first particle, the lateral component of the circulating flow will carry the particle toward the first particle until it reaches its most favorable position adjacent to the initial particle. As the assembly progresses, more particles are incorporated into the lattice, forming 2D colloidal crystals. Using patterned substrates, assembly of ordered PSL microparticles into strip patterns can be achieved.[218]

Other than the EOF, Trau et al.[219,220] attributed the ordered monolayer particle assembly to the EHD flow, also known as induced charge electroosmotic flow. The EHD flow originates from the interaction of an electric field with charge induced in the electrical double layer. When a particle moves close to an electrode, it perturbs the otherwise uniform electric field, creating a tangential field component near the electrode. The action of the tangential field on the induced charge produces the EHD flow, entraining and carrying nearby particles toward the first assembled particle as shown in Figure 8a. Ristenpart et al.[221,222] further elaborated this mechanism by modeling the first assembled particle as a "point-dipole". They showed that the magnitude of the EHD flow and the corresponding assembly rate scale as the square of the applied electric field strength since the tangential field component and the induced charge are each proportional to the field strength.[221−223] Compared with the electric field strength, the effect of the frequency on the magnitude of the EHD flow is not straightforward. At high frequencies, ions in the suspension cannot respond fast enough to redistribute as the polarity of the field oscillates, causing negligible induced charge in the electrical double layer and thus negligible EHD flow.[224] Conversely, at low frequencies, the ions in the suspension have enough time to form the electrical double layer. In this situation, the applied electric field drops almost entirely across the electrical double layer, resulting in a near-zero electric field in the suspension and again ceasing EHD flow.[224] Only at intermediate frequencies, EHD flow exists and hence particle assembly occurs. In the range of frequency where the EHD flow is observed, the magnitude of the flow is inversely related to the frequency,[221,224,225] causing diminishing particle assembly as the frequency increases. Besides the electric field strength and the frequency, the type and the concentration of electrolytes can also affect the EHD flow-directed particle assembly.[226,227] Woehl et al.[228] studied the effect of twenty-six electrolytes and found that the same particles may not always assemble when an electric field is applied, depending on the choice of the electrolytes. The experiments showed trends between ionic strength, pH, ζ potential, and assembly rate. When electrolytes that reduce the ζ potential are used, the particles tend to be less stable in suspension and thus assemble easier. For negatively charged particles, acidic electrolytes facilitate assembly, while for positively charged particles, basic electrolytes promote assembly. Suspensions with high ionic strength from spectator ions that do not change the pH resulted in low ζ potentials for all particles and yielded a faster rate of assembly. When the concentration of ions is high, the dense double layer screens the applied electric field more effectively, causing diminishing EHD flow and decreased particle assembly.[224,229]

In most of the research mentioned above, the EHD flow arises from the perturbation of the applied electric field via assembled particles themselves. However, several results have indicated that inhomogeneity of the current density related to patterned electrodes can also perturb the electric field and hence induce the EHD flow.[230−233] In regions with a high current density, the induced charge in the electrical double layer is low, and vice versa, yielding a lateral electric field gradient and resulting in an EHD flow toward the high current density regions.[232] Gong et al.[234] used microscale photoresist patterns on an indium tin oxide (ITO) electrode and assembled 2,5,8,11-tetra-*tert*-butylperylene (TBPe) organic microparticles under an AC field. The presence of the photoresist layer creates inhomogeneity in the current density on the ITO electrode, wherein the photoresist covered regions possess a low current density and exposed regions possess a high current density. Inhomogeneity of the current density induces an EHD flow directed toward the regions of high current density, where the TBPe particles are assembled (Figure 8b). For the case of the organic TBPe particles, the electrostatic repulsion between particles will result in the decohesion of any assembled layer if the EHD flow is not maintained. Therefore, a DC pulse of 12 V was applied for 2 s to fix the assembled TBPe particles on the ITO electrode.[234] Besides causing nonuniformity in current density, Goel et al.[235] showed that the electrode patterning can also lead to nonuniformity of the electric field. This arises due to the concentrated field effect and manifests as a tangential electric field component and a localized high electric field at the edge of the patterns. The interaction of the tangential field with the induced charge in the electrical double layer induces an EHD flow, carrying particles toward the patterned areas.

The EHD flow is also observed when utilizing coplanar electrodes.[236−239] As illustrated in Figure 8c, the electric field applied to each pair of coplanar electrodes has a substantial tangential component. The tangential electric field is unidirec-
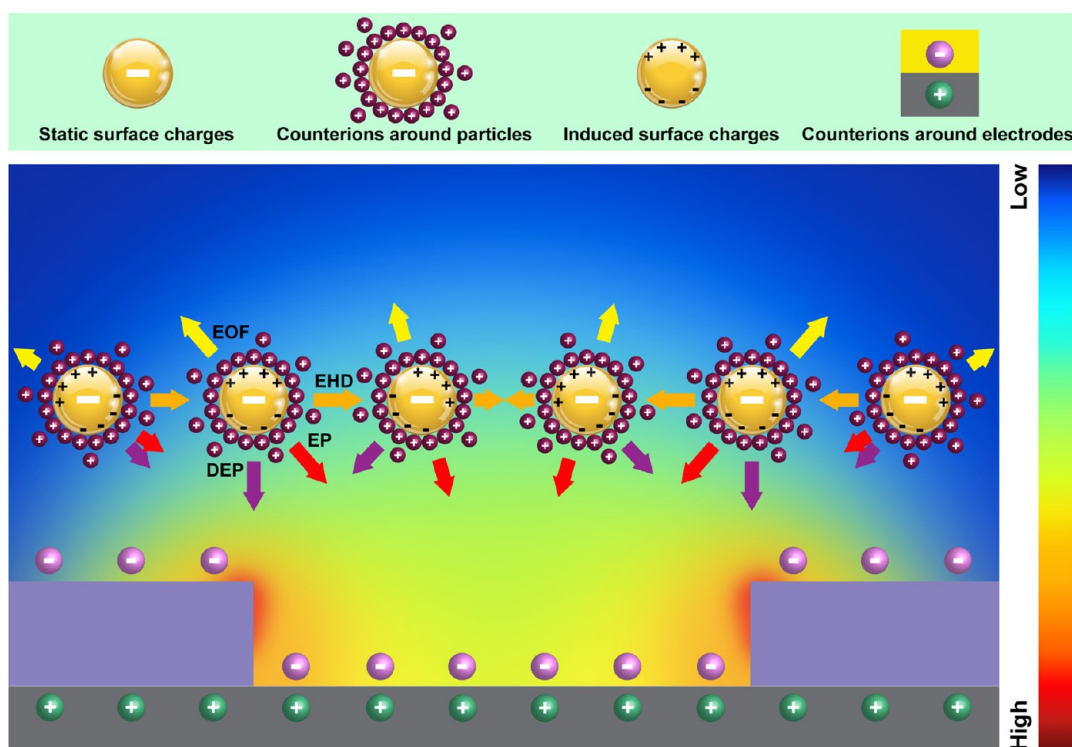
Figure 9. Schematic illustration of all electrokinetic phenomena occurring when an electric field is applied. Particles dispersed in a suspension possess static surface charges due to ionization of surface groups or adsorption of charged species. The polarizability difference between particles and a surrounding medium causes induced surface charges. In addition, charged particles and electrodes are always surrounded by counterions with opposite charges. The interaction of the electric field with the static charges on the particle surface, induced charges on the particle surface, counterions around the particle surface and counterions around the electrode surface causes EP, DEP, EOF, and EHD flow, respectively.

tional and directs from the positive to the negative electrode. Since the induced charge is negative on the positive electrode and positive on the negative electrode, (Figure 8c), the EHD flows generated from the interaction of the tangential electric field with the induced charge have opposite directions near each electrode, flowing along the electrode surface away from the center of the electrode gap, respectively. In view of the symmetry property of the coplanar electrode setup, the EHD flows are canceled at the center of the electrode gap, causing no net fluidic flow therein. This explains the channel-like assembled structures at the center of the electrode gap as mentioned above (Figure 8d).[172]

It should be noted that the EOF reverses its direction in concert with the alternating of the electric field polarity, causing no net fluidic flow and therefore no particle assembly in an AC field, whereas the direction of the EHD flow is independent of the field polarity because the signs of the electric field and the induced charge are coupled.[240] In the situation of a DC field, both EOF and EHD flow contribute to the particle assembly. Ristenpart et al.[240] demonstrated theoretically that the EHD flow predominates over the EOF in the far field, while near the as-deposited particles they are comparable in magnitude. Though the EOF is always attractive, the EHD flow changes from attractive to repulsive when moving close to the particles. However, since the magnitude of the attractive EOF is slightly larger than the EHD flow, a superposition of the two flows still exhibits attractive behavior.

Summary and Perspective for the Electric Field-Directed Assembly. As discussed above, when an electric field is applied to a suspension of charged particles, electro-

kinetic phenomena such as EP, DEP and electrokinetic flows (EOF and EHD flow) arise, leading to the assembly of the particles. In most of the previous studies, particle assembly is attributed to only one of the electrokinetic phenomena; however, in reality, all three electrokinetic phenomena arise simultaneously. The problem lies in the lack of detailed information about the process influencing parameters, magnitude and range of each electrokinetic phenomenon.

The electrokinetic phenomena originate from the response of the particle and medium to an electric field. Particles dispersed in a suspension possess static surface charges due to ionization of surface groups or adsorption of charged species. Besides static charges, the polarizability difference between particles and a surrounding medium causes net induced charges on the particle surface. In addition, charged particles and electrodes are always surrounded by counterions with opposite charges, forming an EDL. The interaction of the electric field with the static charges on the particle surface, induced charges on the particle surface, counterions in the EDL around the particle surface and counterions in the EDL around the electrode surface causes EP, DEP, EOF, and EHD flow, respectively. Figure 9 depicts a qualitative map about all electrokinetic phenomena exerted on particles. EP drives particles to patterned electrodes with opposite charges. DEP drives particles to regions where the electric field strength is high (positive DEP) or low (negative DEP). EOF and EHD flow carry particles along with the flows through Stokes drag force.

Parameters that can affect the electric field strength, the static and induced surface charges or the counterions in the EDL, as listed in Table 1, determine the magnitude and influence of each
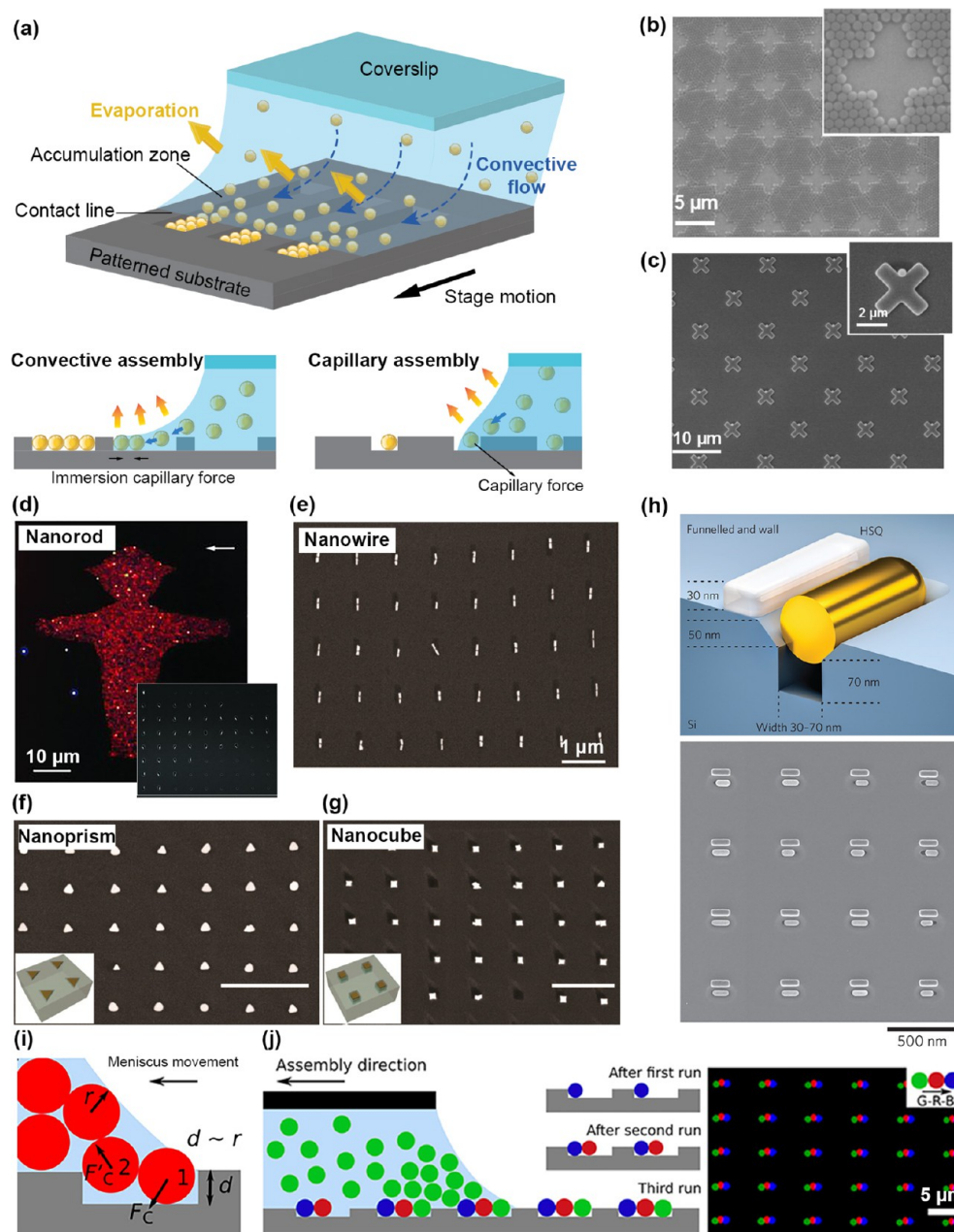
Figure 10. (a) Schematic illustration of two fluidic flow-directed assembly processes: convective assembly and capillary assembly. (b) A monolayer of PSL particles 500 nm in diameter fabricated by the convective assembly process. Reprinted with permission from ref 246. Copyright 2007, American Chemical Society. (c) Spaced arrays of PSL nanoparticles 500 nm in diameter fabricated by the capillary assembly process. Reprinted with permission from ref 246. Copyright 2007, American Chemical Society. (d) Array of aligned gold nanorods assembled by the capillary assembly process. Reprinted with permission from ref 279. Copyright 2012, Wiley-VCH. (e) Array of aligned nanowires assembled by the capillary assembly process. Reprinted with permission from ref 280. Copyright 2014, American Chemical Society. (f-g) Arrays of nanoprisms and concave nanocubes assembled by the capillary assembly process. Reprinted with permission from ref 281. Copyright 2014, American Chemical Society. (h) Schematic illustration of a gold nanorod assembled in a trapping pattern with a funneled cross-section and an auxiliary sidewall (top). An array of nearly perfect aligned gold nanorods. Reprinted with permission from ref 285. Copyright 2017, Nature Publishing Group. (i) Schematic illustration of the forces during the capillary assembly of two particles into one shallow pattern. From ref 287. Copyright 2016 Ni et al., some rights reserved; exclusive licensee AAAS. Distributed under a CC BY-NC 4.0 license http://creativecommons. org/licenses/by-nc/4.0/. Reprinted with permission from AAAS. (j) Schematic illustration of the sequential capillary assembly of different particles one by one in line-shaped patterns (left). Sequential assembly of three different fluorescent polystyrene particles into green-red-blue colloidal chains (right). From ref 287. Copyright 2016 Ni et al., some rights reserved; exclusive licensee AAAS. Distributed under a CC BY-NC 4.0 license http://creativecommons.org/licenses/by-nc/4.0/. Reprinted with permission from AAAS.

electrokinetic phenomenon. By increasing the electric field strength directly, all the electrokinetic phenomena are enhanced, which is beneficial to particle assembly. However, excessive electric field strength is often undesired as electrolysis may happen which causes damage to the assembled structures. The patterns directing particle assembly have the advantage of enhancing local electric field strength through the effect of electric field concentration. When decreasing the pattern area,

the enhancement of the local electric field strength becomes more significant because of the increased electric field concentration, resulting in more particle assembly in the patterned regions. The electric field strength is always high in the vicinity of pattern corners and edges and decays when moving away from the patterns, as illustrated in Figure 9. As a result, the magnitude of each electrokinetic phenomenon varies according to the spatial position of the particles. The pH and electrolyte concentration (ionic strength) of the suspension determines the effective static charges on the particle surface. The pH affects the effective surface charges via influencing the ionization of the surface groups. For negatively and positively charged particles, high and low pH result in more negatively and positively charged surfaces, respectively. The electrolyte concentration determines the extent of the surface charges screened by the counterions. A low electrolyte concentration leads to sparse counterions in the EDL around the particles which screen the surface charges less efficiently and cause more effective surface charges. As a result, the magnitude of the EP phenomenon which is proportional to the effective surface charges is enhanced. While the sparse counterions enhance the EP phenomenon, the EOF phenomenon becomes weak as the EOF arises from the interaction of the electric field with the counterions around the particles. Besides around the particles, counterions also exists in the induced EDL around the electrodes. Similarly, high and low electrolyte concentrations cause dense and sparse counterions around the electrodes, respectively. However, the influence of the electrolyte concentration on the EHD flow is relatively complex. While a high electrolyte concentration causes dense counterions, the applied electric field drops significantly across the EDL, resulting in diminishing EHD flow. Conversely, at a low electrolyte concentration, while the electric field does not drop much across the EDL, the counterions therein become sparse, likewise leading to diminishing EHD flow. Only at a medium electrolyte concentration, the EHD flow exists. Besides the electrolyte concentration, the frequency of the electric field also affects the amount of the counterions in the induced EDL. At a high frequency, ions in the suspension cannot follow the rapid alternation of the electric field, causing negligible amount of counterions and thus negligible EHD flow, while at a low frequency, ions have enough time to form dense regions, resulting in a near-zero electric field in the suspension and again ceasing EHD flow. Similar to the influence of the electrolyte concentration, the EHD flow exists only at a medium electric field frequency. Except for the counterions around the electrodes, the frequency of the electric field also affects the net induced charges on the particle surface. The net induced charges arise from the polarizability difference between particles and a surrounding medium. At a low frequency, the polarization is dominated by the material conductivity. With the increase of the frequency, the polarization becomes dominated by the permittivity. Because of the frequency-dependent polarizability, the net induced charges on the particle surface vary with the frequency, causing varied DEP forces.

Depending on the properties of the electric field, particle suspensions and patterns, the quantitative magnitude as well as the effective range of each electrokinetic phenomenon may differ by orders of magnitude. The direction of different electrokinetic phenomena may even be opposite, causing cancellation of the electrokinetic phenomena and thus cessation of particle movement. However, systematic investigation in these aspects is currently lacking. Although more than one electrokinetic phenomenon is considered in some articles,[91,133,173,224,235] systematically addressing the effect of all the electrokinetic phenomena on the particle assembly is generally lacking. In addition, local Joule heating caused by the electric field gives rise to an additional electrokinetic phenomenon in the form of electrothermal flow acting on the particles.[155,156] Establishing equations combining all the electrokinetic phenomena or setting up criteria for judging which electrokinetic phenomenon is dominant is a fertile field worthy of in-depth studies.

FLUIDIC FLOW-DIRECTED ASSEMBLY

Convective Assembly and Capillary Assembly. In this section, the focus will be on solvent evaporation-induced fluidic flow.[243−245] A schematic illustration of the fluidic flow-directed assembly process is shown in Figure 10a. When a drop of nanoparticle suspension is injected between a patterned substrate and a stationary coverslip, a meniscus is formed at the three-phase (air-solvent-substrate) contact line. As the solvent evaporation rate at the three-phase contact line is normally higher than that in the bulk suspension, preferential evaporation of the solvent at the contact line occurs, which induces a convective flow from the interior of the suspension toward the contact line to replenish the lost solvent. The convective flow carries particles to the contact line where they are then deposited. Depending on the wetting behavior of the patterned substrate, either convective assembly or capillary assembly may occur.[246]

In the case of the convective assembly process,[247−253] also known as slow fluidic assembly,[254−256] the patterned regions are hydrophilic with a contact angle below ∼20° (Figure 10a).[246] Because of the high hydrophilicity, the meniscus tends to spread onto the patterned regions. As the solvent evaporates, the meniscus becomes thinner and once the thickness of the meniscus film approaches the diameter of the particle, the assembly process is initiated. The protrusion of the particles above the liquid surface acts to deform the surface of the meniscus film, inducing a so-called immersion capillary force[257−260] between adjacent particles, under which the particles assemble into ordered mono or multilayer structures (Figure 10b). To achieve assembly by this method, a solution can be allowed to dry slowly on the patterned substrate, or the meniscus can be forced to move at a controlled rate by dip-coating or through the use of a coverslip that moves relative to the substrate. The latter method is preferred as it offers better control over the assembly. The substrate temperature, relative humidity of the atmosphere, substrate velocity, pattern dimensions, and ionic strength are key variables in the convective assembly process.[246,250,261] The substrate temperature and the relative humidity affect the assembly process by influencing the solvent evaporation rate.[246] At a higher substrate temperature or a lower relative humidity, the solvent evaporation rate becomes higher, resulting in a greater flux of nanoparticles toward the contact line and thus a larger assembly efficiency. Compared with controlling the relative humidity, controlling the substrate temperature is relatively simple and therefore it is often used to adjust the assembly process. It has been recognized that a substrate temperature higher than the dew point temperature (T_{dew}) is essential to triggering the assembly process.[246] At the dew point, the solvent evaporation rate at the contact line is almost zero. The nanoparticle influx toward the contact line is suspended and therefore the assembly process stops. Below the dew point, condensation of the solvent

takes place. Instead of generating a convective flow toward the contact line, a recirculation flow from the contact line to the bulk suspension is induced, causing disassembly of nanoparticles. On the other hand, even though a higher substrate temperature is beneficial with regard to accelerating the particle assembly, the temperature should not be excessive since a high rate of evaporation makes the assembly process uncontrollable. Typically, the substrate temperature is in the range of 30 to 50 °C.[75] The velocity of the substrate controls the assembly process by influencing the solvent evaporation time. At a lower velocity, there is more time for evaporation to occur and thus greater particle concentration close to the contact line. As a consequence, a thicker particle assembly can be obtained. If the hydrophilic patterns on the substrate are not large enough, the solvent cannot wet the patterns effectively, causing decreased particle assembly with the decreasing pattern size.[250]

As was the case for electrophoretic assembly, the ionic strength plays a role in the rate of assembly for fluidic methods. In this case, however, a greater ionic strength may lead to more particles being deposited at the receding meniscus. Few studies can be found that directly investigate the relationship between the ionic strength and substrate velocity (such as in dip-coating efficacy). However, there are several that explore the topic of particle adsorption and agglomeration at increased ionic strength, and this can be used to surmise the effect of ionic strength on deposition at a receding meniscus. Bizmark et al. found that the formation of a layer of hydrophobic ethyl cellulose nanoparticles at a liquid/air interface was not influenced by a change in ionic strength when operating in the range of ionic strength usually found in dip-coating processes.[139] The particles did become unstable when the NaCl concentration reached 0.05 M at pH 4. Three other studies that used similar methods showed that a high ionic strength can allow greater deposition of nanoparticles onto a submerged surface.[137,262,263] For example, Winkler et al. studied the adsorption of gold nanoparticles on glass and silicon as a function of ionic strength ranging from 0 to 4.6 M of added NaCl.[263] Four different regimes were delineated. In a regime with a concentration <0.5 M, the particles were stable due to electrostatic repulsions, but agglomerated for concentrations from 0.6 to 1.75 M. Surprisingly, for higher concentration from 2 to 3 M, the particles became stable once more due to hydration forces brought about by the Na$^+$ and Cl$^-$ ions. This regime also showed much greater particle deposition on the submerged substrate surface. For even higher concentration, the particles were stable, but did not deposit on the substrate. These studies point to the possibility of using a high ionic strength to advantage when using convective and fluidic assembly methods to increase the amount of particles deposited. Due to the screening effect of a higher ionic strength, the repulsive force between particles is diminished, leading to less steric hindrance when depositing in the absence of an electric field, although the high ionic strength may be detrimental for dip-coating due to the precipitation of salt during the drying process.

Using the fluidic/convective assembly process, Abbasi et al.[109] fabricated silver grid electrodes with a high resolution (line width 2 μm) over centimeter-sized flexible poly(ethylene terephthalate) (PET) substrates. Because of the narrow line width, light can pass through with a high average transmittance of >92% in the visible light range. To test the scalability and precision of the fabrication process, a grid electrode with a line width down to 300 nm on a glass substrate was also demonstrated. Chai et al.[179] assembled highly aligned SWCNTs using the fluidic assembly process. The authors found that the degree of alignment depends on the relative size between the length of the SWCNTs and the width of the channel patterns. Only when the channel width is smaller than the SWCNT length, unidirectional alignment of SWCNTs can be achieved. The pattern geometry-dependent alignment was ascribed to the curvature of the contact line as the assembled SWCNTs typically align along the contact line of the meniscus. Due to the contrast in wettability between the pattern and photoresist, the contact line is not linear across the channel, but rather it is parallel to the channel wall at the edge of the channel and perpendicular to the channel walls in the center. For a channel width much larger than the SWCNT length, the orientation of assembled SWCNTs resembles the shape of the contact line, while for channels with width smaller than the SWCNT length, the assembled SWCNTs align mainly along the channel. Besides the contact line confinement, the capillary force is deemed to be responsible for the SWCNT alignment. For narrow channels, anchoring one end of the SWCNTs in the pattern areas while leaving the other end floating in the suspension is likely to happen. The capillary force exerted by the meniscus can stretch the floating end of SWCNTs, resulting in their alignment.

As the hydrophobicity of the patterned regions increases, the assembly process comes into the capillary assembly regime (Figure 10a).[264−270] For the capillary assembly process, the contact angle typically ranges between 50° and 60°.[271,272] At such a high contact angle, the meniscus does not spread on the patterned regions and the particles are no longer confined to a thin meniscus layer. In this case, the meniscus moving over the substrate acts as a doctor blade, exerting a lateral capillary force on the particles and dragging the particles to move along with it until the particles are trapped by the recessed areas of the patterned substrate (Figure 10c). Other than forming close-packed ordered mono or multilayer structures as the convective assembly process, the capillary assembly process is also capable of accurately placing individual particles or a few particles in the patterned regions (Figure 10c).[273−277] The assembly efficiency as a function of the parameters is similar to the convective assembly process. A higher substrate temperature, a lower relative humidity and a lower substrate velocity result in a higher assembly efficiency. The formation of an accumulation zone at the frontier of the contact line is deemed to be critical for the initiation of the capillary assembly process.[246,278] The accumulation zone consists of highly concentrated and close-packed nanoparticles of solid or liquid-crystalline nature. Because of the high particle concentration, mutual confinement between adjacent particles becomes strong, suppressing the effects of Brownian motion. As a consequence, the mobility and fluctuations of the nanoparticles in the accumulation zone is drastically reduced, causing an increased trapping efficiency in the assembly sites. Dedicated geometric design of the trapping patterns plays an important role in controlling the capillary assembly process. By tailoring the trap geometry, controlled assembly of nanoparticles with various shapes, such as rods,[279] wires,[280] cubes,[271,281] and nanoprisms,[281] can be achieved on the single particle level (Figure 10d−g). The assembly efficiency and the angular distribution of these anisotropic nanoparticles are very sensitive to the lateral dimensions of the trapping patterns. For efficient particle assembly, the lateral dimensions of the patterns should be large enough to house an individual nanoparticle enveloped by surface ligands or its electrical double layer.[282−284] In addition, large patterns not only result in a sufficient capillary force to trap the nanoparticles but also
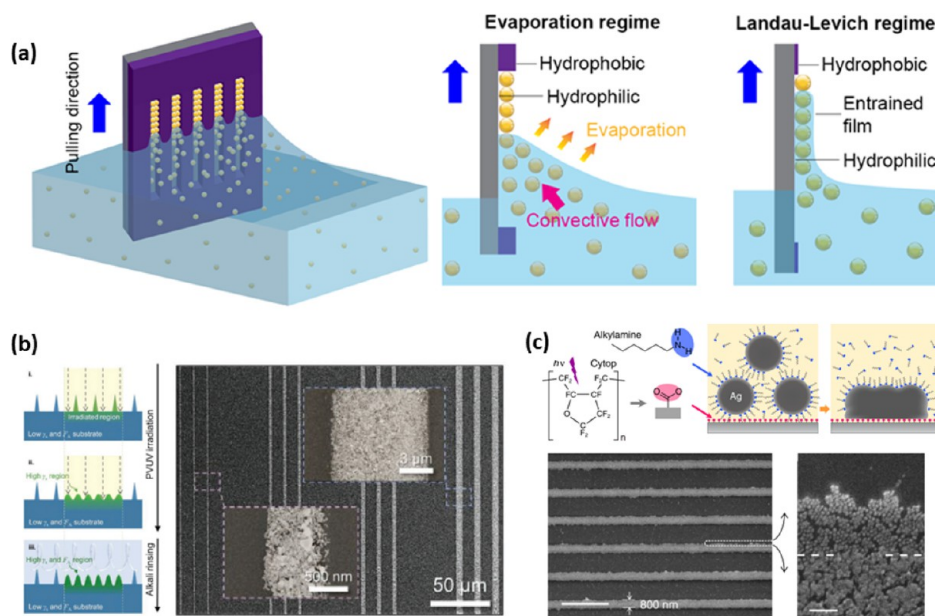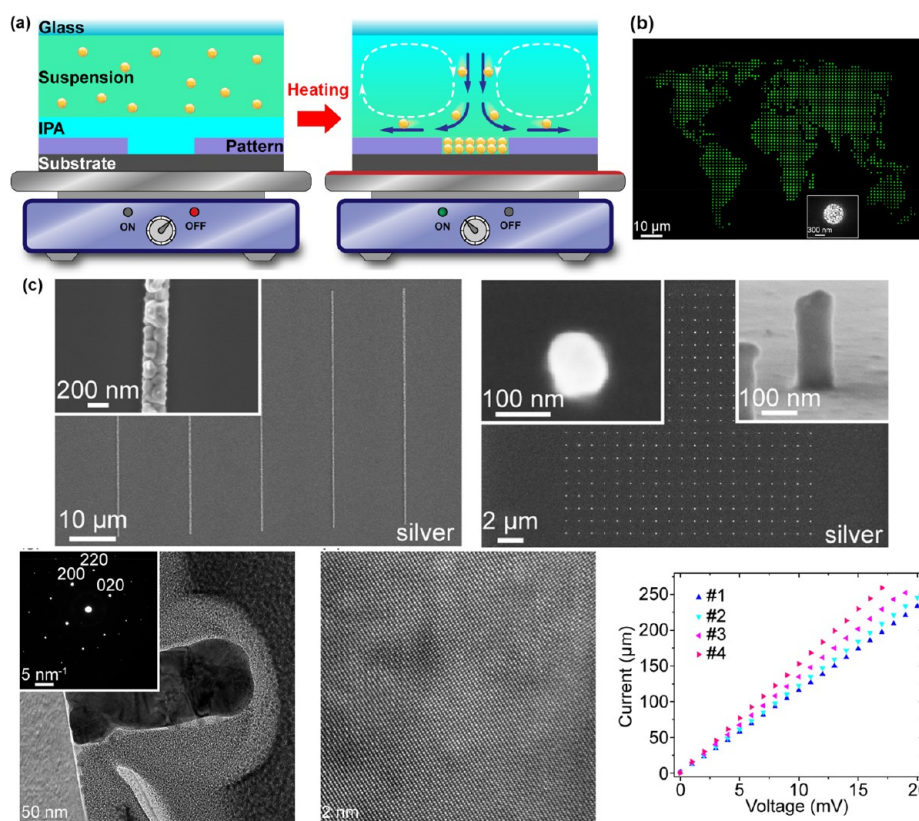
Figure 11. (a) Schematic illustration of the convective/fluidic assembly and fast fluidic assembly processes which work in the evaporation regime and Landau−Levich regime, respectively. (b) Photoirradiation and chemical polarization treatments to the substrate in order to enhance the surface adhesion force. As a result, a 600 nm high resolution was achieved. Reprinted with permission from ref 303. Copyright 2021, Wiley-VCH. (c) Utilizing the strong chemisorption between the carboxylate groups and bare silver nanoparticles to increase the adhesion force. A line width of 800 nm was obtained. Reprinted with permission under a Creative Commons CC BY 4.0 License https://creativecommons.org/licenses/by/4.0/ from ref 305. Copyright 2016, Nature Publishing Group.

provide extra space for the nanoparticles to adjust their orientations.[280,281] However, patterns of larger size capture multiple particles and do not allow for control of particle orientation.[284] In order to achieve high efficiency in assembly and a narrow angular distribution, the pattern dimensions must be optimized. Besides optimizing the pattern dimensions, Flauraud et al.[285] enhanced the assembly efficiency and the particle orientation through adjusting the pattern geometries. Four trap geometries; straight-edged, funneled, straight-edged with auxiliary sidewall, and funneled with auxiliary sidewall, were designed and used to investigate the assembly behavior of gold nanorods. For the commonly used straight-edged traps, a larger pattern width gave a higher assembly yield at the expense of a wider angular distribution. When adding a funnel structure to the straight-edged traps, the acceptance area for the nanorods enlarged, which increased the probability of particle capture. Additionally, as the bottom trench was narrower than the nanorod diameter, the nanorods were mechanically locked at the center of the trap during solvent evaporation. These two geometric factors resulted in a greatly increased assembly efficiency and a much narrower angular distribution. One problem is that the assembled nanoparticles are prone to removal when they lie nonparallel to the receding contact line. In order to counter particle removal during the assembly, the authors placed a vertical barrier along a single edge of the funneled traps, as shown in Figure 10h. By doing so, the optimal assembly yield and angular distribution were achieved. Other than the lateral dimensions and the pattern geometry, the vertical dimension can also affect the capillary assembly process. Ni et al.[286,287] demonstrated that the pattern depth plays an important role in determining how many particles can be assembled in individual trap sites during a single assembly step. As depicted in Figure 10i, when assembly occurs over shallow patterns, the nanoparticles at the front of the contact line (particle 1) interacts directly with the meniscus, experiencing a

downward capillary force perpendicular to the meniscus. This capillary force is partially transmitted to the nanoparticle at the rear of the contact line (particle 2), applying an upward force to particle 2 and pushing particle 2 out of the pattern. Particle 1 is then deposited at the rear of the pattern. When the pattern depth increases, the upward force applied to particle 2 is not sufficiently strong to push the particle out and therefore both particles 1 and 2 stay in the pattern. This phenomenon was subsequently utilized by the authors to sequentially assemble different particles in the shallow patterns to form hybrid nanoparticle clusters during a multistep capillary assembly process (Figure 10j).[287,288]

Fast Fluidic Assembly. The capillary and fluidic assembly processes rely on a convective flow induced by solvent evaporation to direct particle assembly. To match the rate of evaporation, extremely slow motion of the substrate at a few micrometers per second is required,[75] which poses an enormous obstacle to the scalability and consequently the practical application of these two processes. If the velocity of the substrate is much greater than the rate of evaporation, a transition from the evaporation regime to the Landau−Levich regime takes place (Figure 11a).[289−293] In the Landau−Levich regime, the adhesion force, also known as the static friction force, imposed by the substrate on the nanoparticle suspension becomes dominant. As a consequence, a film of the suspension is entrained on the surface of the substrate that will then dry and leave behind the nanoparticles within. Utilizing a substrate with patterned wettability, site-selective assembly of nanoparticles can be achieved. This is referred to as the fast fluidic assembly method by Busnaina and co-workers.[294] The fast fluidic method requires suspensions with a high concentration of solids if an even coating is desired once the suspension dries. In the previous sections on the topics of electric field and fluidic flow driven assembly, the concentration of the suspensions can be relatively low, typically 0.5 wt % or less. However, the suspensions used in

Figure 12. (a) Schematic illustration of the interfacial convective assembly process. (b) Assembly of silica nanoparticles into an array of vias 600 nm in diameter, forming a microscale world map. (c) Assembly of 5 nm silver nanoparticles into arrays of sintered nanowires and nanorods (top). The assembled nanorods exhibit a single crystal structure (bottom, left and middle). *I–V* curves of four assembled silver nanorods (bottom, right). Reprinted with permission from ref 317. Copyright 2020, Wiley-VCH.

the fast fluidic method often have solids in excess of 10 wt %. The viscosity and surface tension of the suspensions are similar to inks used for inkjet printing, although liquid media of a wide range of viscosities can be used from water to ethylene glycol or even much higher. This often necessitates the use of organic solvents, binders, and surfactants in the suspension that can dissolve the photoresists typically used as templates for nanomaterial assembly. Because of this limitation, a surface functionalized with a hydrophobic self-assembled monolayer (SAM) can be used instead of a photoresist as a template. The SAM provides a high contrast in wettability between the pattern and the surrounding substrate area and allows confinement of assembly solely within the patterned hydrophilic areas.[250,295,296] The detailed process of functionalizing the substrate with a SAM can be found in previously published articles.[297−299] Currently, the fast fluidic assembly process is mostly used to fabricate patterns with dimensions in millimeter or submillimeter scale.[300−302] This is because the viscous force from the substrate diminishes with the dimensions of the pattern.[303,304] Li et al.[303] enhanced the surface adhesion force through photoirradiation and chemical polarization treatments to the substrate. As a result, a submicrometer (600 nm) resolution was achieved (Figure 11b). Yamada et al.[305] functionalized a patterned surface with carboxylate groups and utilized the strong chemisorption between the patterns and bare silver nanoparticles to increase the adhesion. A line width of 800 nm was obtained (Figure 11c). Besides the physical and chemical properties of the substrate, adjusting the properties of the nanoparticle suspension and the speed of the meniscus could be another solution to increase the adhesion force. According to a modified Landau−Levich−

Derjaguin equation, the maximum thickness of the entrained film on a substrate can be calculated by[306−308]

$$h_{max} = kwCa^{1/3} \qquad (19)$$

where k is a constant depending on the assembly set up, w is the width of the pattern, $Ca = \mu V/\gamma$ is the capillary number, μ and γ are the viscosity and surface tension of the nanoparticle suspension, and V is the speed of the meniscus. By increasing the viscosity and meniscus velocity and decreasing the surface tension, the thickness of the entrained film increases.[309,310] However, the realization of high resolution assembly by adjusting those three parameters is rarely reported.

Contrary to other assembly methods covered in this review, fast fluidic assembly suffers from the coffee ring effect where the rate of evaporation at the edge of the deposited liquid film is greater than at the center.[311] The preferential solvent evaporation induces a flow of the suspension toward the edge to compensate for the lost solvent and results in greater deposition of nanoparticles at the edge. The existence of the coffee ring effect can influence the uniformity of thickness as well as the consistency of electrical properties of the fabricated electronics and sensors. The coffee ring effect can be minimized through adjusting the composition of the nanoparticle suspension.[312] Kim et al.[313] added ethylene glycol (EG) with a high boiling point and low surface tension to a water-based nanoparticle suspension and studied the drying behavior of a droplet under ambient conditions. At the edge of the droplet, preferential evaporation of water takes place, leaving behind increased fraction of high boiling point EG and decreased

surface tension therein, while the center of the droplet has more water with a high surface tension. The surface tension gradient induces an inward Marangoni flow from the edge to the center of the droplet which cancels the outward capillary flow and thus reduces the coffee ring effect. In addition, adding surfactants to the nanoparticle suspension can also induce the Marangoni flow and reduce the coffee ring effect.[314−316]

Interfacial Convective Assembly. In order to improve throughput, Chai et al.[317] used a fluidic flow-directed assembly process known as interfacial convective assembly that uses a substrate heating-induced convective flow to drag nanoparticles toward patterned substrates where particles are bound to the patterned areas through van der Waals interactions and geometrical confinement (Figure 12a). Isopropyl alcohol and an aqueous nanoparticle suspension are mixed during the assembly process to generate a solutal Marangoni-dominated convective flow. The authors demonstrated both experimentally and theoretically that the solutal Marangoni convective flow is at least 2 orders of magnitude stronger than a thermal Marangoni convective flow generated from a monocomponent solvent (water), enabling efficient assembly of the nanoparticles over centimeter scale substrates within a few minutes (2 orders of magnitude faster than the conventional convective assembly process). Increasing the substrate temperature, the particle concentration and the assembly time can lead to an increased assembly yield. Using the interfacial convective assembly process, various nanoparticles such as PSL, silica, gold, and silver were assembled in patterns with a variety of geometries such as trenches, diamonds, or circles (Figure 12b) with a high resolutions down to 25 nm. This method is particularly useful for the scalable production of electronics with multiple layers of materials. Vias are a critical component of multilayer electronics that serve as connections between layers, and they can be assembled using this method on any substrate regardless of conductivity. The solutal Marangoni convective flow can obtain a high velocity in the range of meters per second. When nanoparticles are carried by the flow to circulate in the suspension, collision and coalescence of the nanoparticles occurs. The authors found that self-annealing occurs during the assembly of 5 nm silver nanoparticles, forming sintered nanopillars and nanorod structures (Figure 12c). The silver nanorods exhibited a single crystal structure with a low resistivity of 8.58×10^{-5} Ω cm, showing great potential to be used as 2D and 3D interconnects in complementary metal−oxide−semiconductor (CMOS) devices. Although high assembly efficiency and self-annealing to produce single crystal structures using the interfacial convective assembly process have been demonstrated, more in-depth studies of the mechanism and the controlling parameters of the solutal Marangoni flow are still needed to develop a better understanding and control of the process.

Self-annealing was also observed during electrophoretic assembly.[121] In this case, the phenomenon occurred when assembling 5 nm gold nanoparticles. By considering the contact radius caused by deformation during assembly and the current passing through the particles, it was calculated that the temperature can increase by nearly 600 °C for 5 nm gold particles during DEP assembly with typical parameters of 12 V_{AC}, 2 V_{DC} offset, and 50 kHz. When these parameters were applied to particles 20 nm in size, only partial fusing was observed, while 50 nm particles showed no fusing at all. It was also calculated that for such small particles, even the van der Waals force between them is enough to cause a large deformation.

Summary and Perspective for the Fluidic Flow-Directed Assembly. Although the convective and capillary assembly processes are applicable to all kinds of nanomaterials and have demonstrated controlled assembly on centimeter scale, their practical application faces two main problems. First, assembly only happens at the three-phase contact line where the particle concentration is high. Second, a very slow motion of the substrate at a few micrometers per second is required in order to match the slow solvent evaporation.[75] The solvent evaporation can be accelerated by increasing the substrate temperature. However, a high temperature increases the particle concentration in the bulk suspension during the assembly process and thus makes the assembly process uncontrollable.[246] Although a high particle concentration may also allow a fast assembly, the particle concentration has an upper limit if the stability of the nanoparticle suspension is to be maintained. Therefore, the throughput of the convective assembly and capillary assembly processes is a major challenge. A possible resolution to this issue will be explored in the next section which covers the topic of assembly through combined use of electric fields and fluidic flow methods.

The fast fluidic assembly process can realize a high efficiency of tens of millimeters per second. However, typically, the dimension of patterns fabricated is in the millimeter or submillimeter scale. The reason lies in insufficient adhesion of the nanoparticle suspension to the patterned areas. Through adjusting the physical and chemical properties of the substrate, a high resolution in submicrometer scale has been achieved. Further increasing the resolution by tuning the properties of the nanoparticle suspension and the meniscus moving speed is highly desirable. Another issue of the fast fluidic assembly process is that it is almost impossible to fabricate loop structures.[318] This is because the three-phase contact line cannot dewet in the enclosed hydrophobic areas. Therefore, loop structures must be avoided.

The interfacial convective assembly process has shown promise for rapid assembly of various nanoparticles in arbitrary patterns. However, the interfacial convective assembly method is still in the initial stage of development. More in-depth studies of the origination and the controlling parameters of the solutal Marangoni flow are needed to develop a better understanding and control of the process.

Combined Use of Electric Fields with Convective Fluidic Flow. The methods of electric field driven assembly and fluidic assembly can be combined to increase the rate of assembly. While it is true that any sample submerged in suspension while using EP or DEP must be removed from the suspension after the assembly takes place, it is assumed that any fluidic assembly that occurs during removal of the sample is negligible. For the combined method, a bias can be applied while a patterned substrate is undergoing convective or capillary fluidic assembly to increase the forces of assembly. This can help to circumvent the slow speeds usually required for convective and capillary assembly, and also leads to improved assembly efficiency overall. Using this electro-fluidic approach, Sirman et al. demonstrated the controlled assembly of nanomaterials that are conducting, semiconducting, and insulating including nanoparticles and SWCNTs in different patterns down to 100 nm.[122,319] This assembly can also be accomplished on insulating substrates by using a gold layer with a thin coating of patterned SiO$_2$ serving as the assembly surface, although highly doped silicon can also serve as the conductive layer. The bias leads to accumulation of the particles near the substrate surface, thus
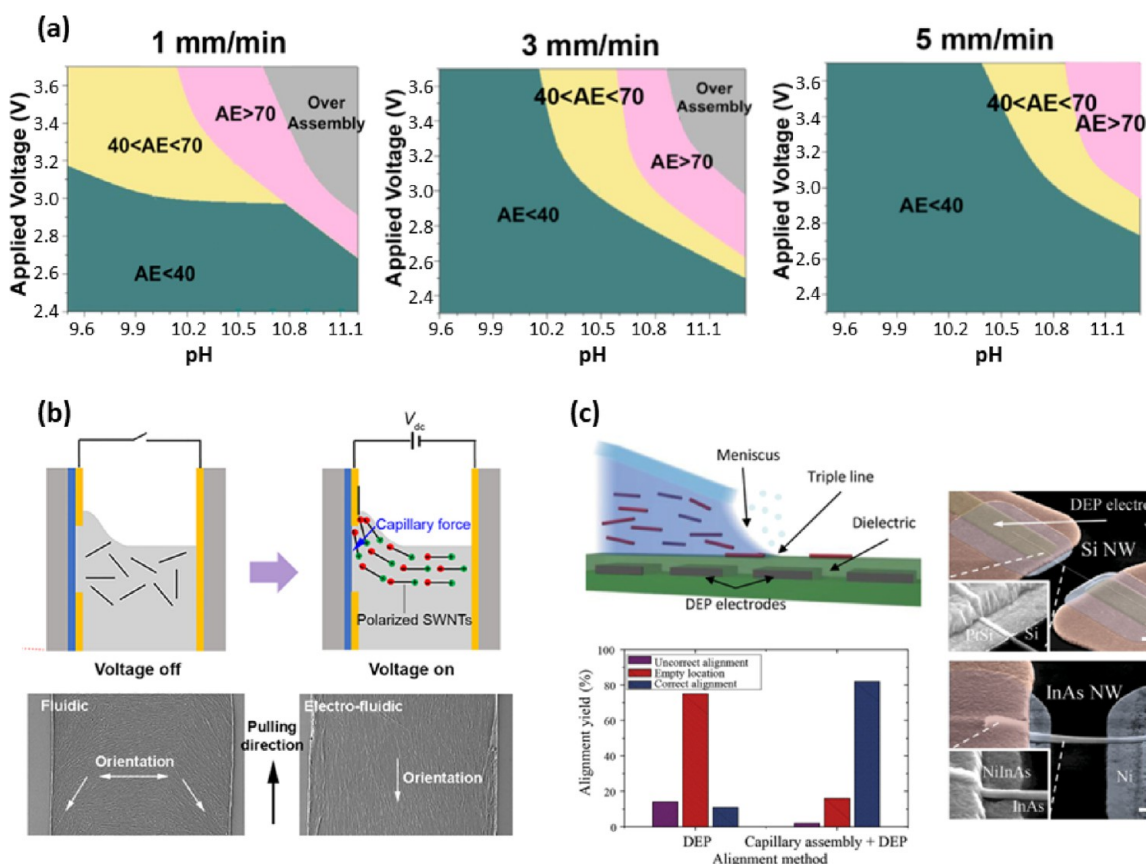
Figure 13. (a) Measurements of assembly efficiency as a function of voltage, pH, and withdraw speed. Reprinted with permission from ref 122. Copyright 2017 American Chemical Society. (b) Assembly of aligned SWCNTs using the electro-fluidic assembly process. In contrast to fluidic assembly, the alignment of the SWCNTs in electro-fluidic assembly is geometry-independent. Reprinted with permission from ref 179. Copyright 2018, American Chemical Society. (c) Assembly of aligned single Si or InAs nanowire between patterned electrodes by combining the DEP assembly and capillary assembly. Reprinted with permission from ref 320. Copyright 2015, Wiley-VCH.

increasing their concentration and allowing for increased deposition during capillary assembly. The efficiency of assembly for the PSL particles was measured as a function of applied voltage and pH at three different withdraw speeds (Figure 13a).[319] The results show that even for the relatively fast speed of 5 mm min^{-1}, an assembly efficiency of greater than 70% can be achieved. Near 100% assembly can be achieved at lower speeds, but overassembly can occur at higher voltages. This demonstrates that the electro-fluidic method could be a pathway for scalable assembly of nanoscale devices using EP. In similar fashion, Cho et al. used the electro-fluidic method to assemble various particles and CNTs by dip coating at 3−15 mm min^{-1} with an applied bias of 2−5 V.[321] Chai et al. also used this method to assembled multiwalled carbon nanotubes (MWCNTs) and SWCNTs, with the added benefit of aligning the SWCNTs.[179,322] The electric field polarized the SWCNTs in the suspension and exerted a DEP force which anchored the SWCNTs to the patterned substrate with a perpendicular orientation (Figure 13b). When the substrate was withdrawn from the suspension, the free ends of the SWCNTs were held by the capillary force, thus aligning the SWCNTs parallel to the pulling direction. SWCNTs with an average length of 1.5 μm were assembled and aligned in channels with widths from 1 to 100 μm. Similarly, Collet et al.[320] assembled and aligned single silicon and InAs nanowires at large scale by combining DEP and capillary assembly (Figure 13c). Because of the additional DEP

force, the assembly yield was improved by 5-fold and the alignment accuracy was improved by 8-fold.

Assembly on an insulating substrate. Thus, far it has been assumed that a conductive substrate is required for EP, but this is not true. Work has been done on conducting EP assembly on an insulating SiO$_2$ layer (Figure 14 (a)).[122,319] The caveat is that the SiO$_2$ must have a conductive layer beneath it with which to produce an electric field. SiO$_2$ layers of 50, 150, and 1000 nm in thickness were evaluated. The assembly was conducted at 3 V, pH 11.1, and a withdrawal speed of 3 mm min^{-1} using PSL particles. Using these parameters, the 50 nm SiO$_2$ layer showed over assembly while the 1000 nm SiO$_2$ layer had little assembly. However, the 150 nm SiO$_2$ layer showed good assembly.

Through the experiments on insulating substrates, it was also confirmed that the combined electro-fluidic method works well even if the pattern to be filled is not withdrawn along its major axis. This was demonstrated for patterns withdrawn at 0°, 90°, (represented by a cross) and 45° with respect to the withdraw direction. The speed was set to 3 mm min^{-1} and the pH was maintained at 10.9. Figure 14 (b) shows that each of the patterns were well filled when a bias of 3.3 V was applied. The cross was found to be problematic in that the central area was more difficult to fill than a linear pattern, but 3.3 V was sufficient to ensure full assembly.

Directed Assembly and Transfer. Busnaina and co-workers[321−323] used directed assembly methods for a nanoscale offset printing process, as shown in Figure 15a. In this process, a
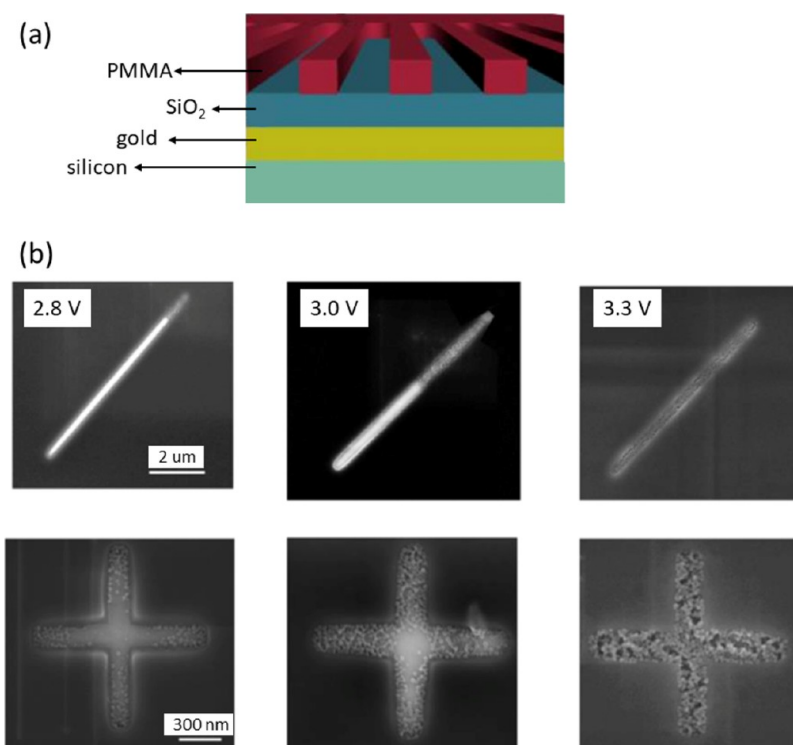
Figure 14. (a) Cross sectional depiction of the substrate used for field-driven assembly on an insulating surface. High efficiency of assembly was found for an SiO$_2$ thickness of 150 nm at a voltage of 3.3 V. (b) SEM images of assembly performed while the pattern was withdrawn at certain angles from the PSL suspension. The dark areas show a high density of particles. Reprinted with permission from ref 122. Copyright 2017, American Chemical Society.

substrate with patterned conductive and hydrophilic areas is first fabricated using conventional lithographic methods. When an electric field is applied, elements are assembled on the patterned areas under an electrophoretic force. The assembled elements are then transfer printed onto a flexible substrate with the assistance of elevated temperature and pressure, forming functional micro/nanoscale structures. The offset printing process was utilized by Chai et al.[322] to fabricate organic field effect transistors with source/drain electrodes fabricated from CNTs via directed assembly and subsequent transfer printing (Figure 15b). Wang et al. used this method of transfer printing to create all carbon FETs where the channel is composed of semiconducting SWCNTs and the source/drain electrodes are composed of MWCNTs (Figure 15c). More than 70% of the devices tested had an on/off ratio of 10^3 or greater and some showed mobilities of 8.84 cm^2 V^{-1} s^{-1}, which is comparable to other devices made from printed CNTs. A recent analysis of the cumulative energy demand for this printing method has also been made.[324] The analysis by Abbasi et al. considers the energy required to produce FETs using typical lithography and deposition methods of a modern fabrication facility compared to the energy required to produce the same FETs using nanomaterials. The analysis shows that electronics made using bottom-up methods such as offset printing nanomaterials can reduce energy consumption by an order of magnitude or more.

Here, we have only considered the interaction of electrophoretic forces with fluidic flow. However, in most studies nanoparticle assembly is attributed to only one field-induced effect, such as EP, dielectrophoresis, or electrokinetic flow. In reality, each effect mentioned above contributes to the motion of the nanoparticles. Although more than one effect is employed or considered in some articles,[91,133,173,235] systematically address-

ing the influence of all the effects on the particle assembly is generally lacking. The significance of each force under various assembly parameters, such as electric field strength, frequency, particle size, dielectric constant and conductivity of the nanoparticles and the medium, solvent type, pH, electrolyte type and concentration, and pattern geometry, is a fertile field worthy of in-depth study.

MAGNETIC FIELD-DIRECTED ASSEMBLY

Magnetophoretic-Directed Assembly. Magnetic fields are another widely used means of particle assembly.[325−334] In the presence of an external magnetic field, particles in a suspension experience a magnetic force because of the magnetophoresis phenomenon,[335−338] which arises from a combined effect of the magnetic field gradient and the mismatch in magnetic susceptibility between the particles and the surrounding medium (Figure 16a). For a superparamagnetic nanoparticle that is only magnetized in the presence of a magnetic field, the magnetophoretic force acting on a particle in suspension can be calculated as[338−340]

$$F_{\text{mag}} = \frac{V_p(\chi_p - \chi_m)}{\mu_0}(B \cdot \nabla)B$$

(20)

where μ_0 is the permeability of free space ($4\pi \times 10^{-7}$ T·m A^{-1}), V_p is the volume of the particle, B is the magnetic flux density, and χ_p and χ_m are the dimensionless volume magnetic susceptibilities of the particle and the medium, respectively. Nanoparticles with permanent magnetic dipoles can also be manipulated by this method, though they will tend to cluster together even in the presence of a strong external field, thus making them less suitable for precise assembly.
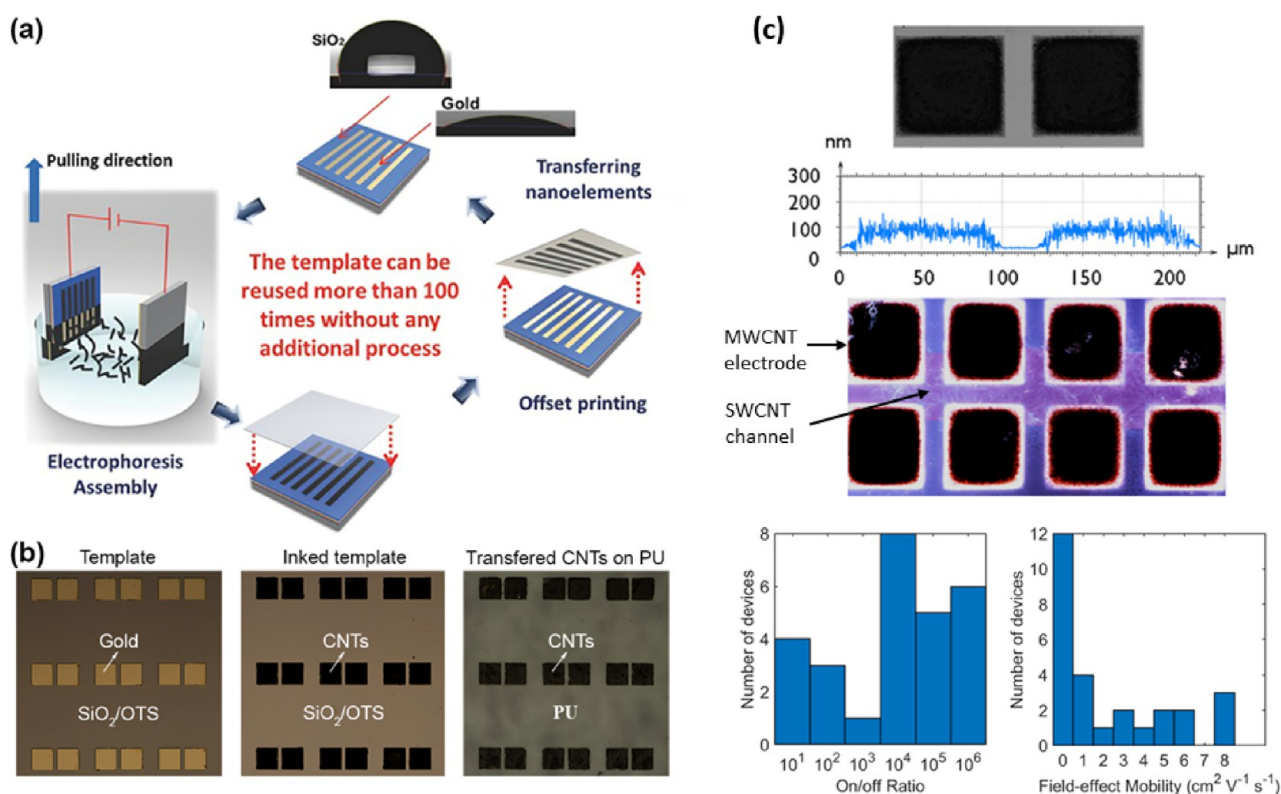
Figure 15. (a) Schematic illustration of the nanoscale offset printing process. Reprinted with permission from ref 321. Copyright 2015, Wiley-VCH. (b) Damascene template before (left) and after (middle) EP assembly of CNTs. Transfer printed CNT patterns on a polyurethane film (right). Reprinted with permission from ref 322. Copyright 2019, AIP Publishing. (c) (top) Height profile of printed MWCNT contacts. (Middle) Printed SWCNT channel with MWCNT contacts. (Bottom) Device characteristics of printed all CNT FETs. Reprinted with permission from ref 323. Copyright 2020, AIP Publishing.
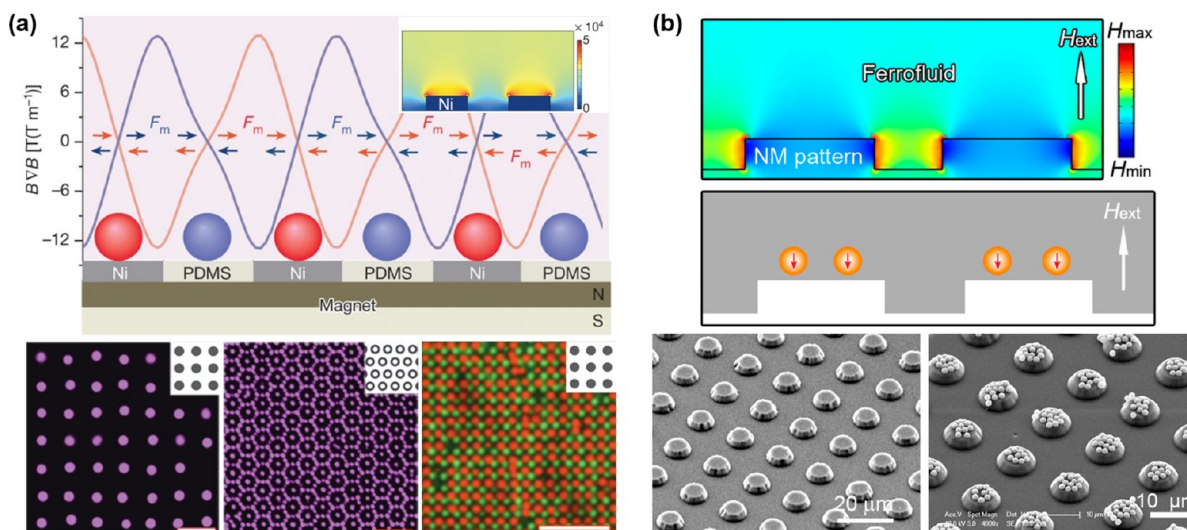
Figure 16. (a) Scheme of calculated magnetophoretic force profiles for a patterned nickel grid embedded in a thin film of PDMS. The magnetophoretic force positions paramagnetic particles (red) onto the nickel grid and diamagnetic particles (blue) in the voids of the grid (top). The inset illustrates the magnetic field strength profile above the nickel grid placed on a permanent magnet. Paramagnetic particles 2.85 μm in diameter assembled on a square grid of nickel islands (bottom, left). Diamagnetic particles 1.2 μm in diameter assembled in the voids of a hexagonal grid of nickel rings (bottom, middle). Paramagnetic particles (red, 1 μm in diameter) and diamagnetic particles (green, 1.2 μm in diameter) assembled into an AB lattice on the underlying square grid (bottom, right). Scale bars, 10 μm. Reprinted with permission from ref 365. Copyright 2013, Nature Publishing Group. (b) Simulated magnetic field distribution around a nonmagnetic PU template immersed in a magnetized ferrofluid (top). Schematic illustration of magnetophoretic assembly of colloidal spheres on the PU template (middle). SEM image of the PU template before (bottom, left) and after (bottom, right) particle assembly. Reprinted with permission from ref 366. Copyright 2013, American Chemical Society.

A difference in magnetic susceptibility is a prerequisite for the induction of the magnetophoretic force. When the magnetic susceptibility of the particle (χ_p) is greater than that of the medium (χ_m), such as a magnetic particle suspended in a diamagnetic medium, a positive magnetophoretic force is induced, which drives the particle toward the maximum of the magnetic field. On the other hand, when a diamagnetic particle is suspended in a magnetic medium, a negative magnetophoresis occurs, in which case the particle is drawn toward the magnetic field minimum.[341,342] A diamagnetic particle is supposed to have no magnetic field effect due to its negligible induced magnetic moment. However, when suspended in a magnetic medium, the diamagnetic particle serves as a magnetic hole with an effective magnetic moment in the opposite direction of the magnetic field.[343] Typical magnetic fluids are ferrofluids (such as magnetite (Fe_3O_4) nanoparticles with a diameter in the range of 10 to 20 nm suspended in water) and paramagnetic salt solutions (such as manganese chloride ($MnCl_2$)).[344,345] The ferrofluids are superior to the paramagnetic salt solutions in that they require much smaller magnetic fields for effective manipulation.[341]

Based on eq 20, the magnetic field gradient is another requirement for the induction of the magnetophoretic force.[346−348] The magnetic field gradient can be generated by utilizing patterned field modulators or photolithographically patterned micromagnets.[349−356] Kimura et al.[357−359] used magnetic field modulators consisting of alternating aluminum and iron sheets 100 or 300 μm in thickness during particle assembly. As the magnetic flux is selectively absorbed by the iron layers, the flux density over the iron layers is lower than that over the aluminum layers. When placing the modulators in a uniform horizontal magnetic field, a modulated magnetic field with a higher magnetic flux density over the aluminum layers is created, generating a magnetic field gradient. Under the magnetic field gradient, various particles such as PSL and mouse osteoblast cells were successfully assembled. Because the thickness of the aluminum and iron sheets used for the modulator fabrication ranges up to several hundred micrometers, the modulated magnetic field pattern generated is also on the scale of one hundred micrometers, which limits the resolution of the assembled structures. High-resolution magnetic field-directed assembly can be achieved using patterned micromagnets.[360−364] In this circumstance, ferromagnetic microstructures are defined using standard photolithography and lift-off processes on diamagnetic substrates such as silicon and glass wafers. Demirörs et al.[365] fabricated nickel patterns embedded in a poly-(dimethylsiloxane) (PDMS) film with a dimension down to ~1 μm (Figure 16a). The patterned nickel microstructures alter the otherwise uniform external magnetic field in their vicinity, generating the desired magnetic field gradient to drive particle assembly. Using the modulated magnetic field, the authors assembled both paramagnetic and diamagnetic particles simultaneously. A paramagnetic salt ($Ho(NO_3)_3$) with a fine-tuned concentration was added to the particle suspension so that the magnetic susceptibility of the suspending medium is smaller than that of the paramagnetic particles and larger than that of the diamagnetic particles. By doing so, the paramagnetic particles were attracted to the nickel patterns where the magnetic field strength is high, while the diamagnetic particles were attracted to the PDMS regions where the magnetic field strength is low, as shown in Figure 16a. Patterning micromagnets on solid substrates takes several steps and requires the use of sophisticated instruments. To avoid this, He et al.[366] utilized a soft lithography process to fabricate nonmagnetic polymer templates. An oligomer solution was poured onto a PDMS master and then cured by UV-polymerization, creating polyurethane (PU) patterns that replicate the design of the PDMS master. The nonmagnetic PU patterns in a ferrofluid behave as reverse micromagnets when exposed to an external magnetic field owing to the mismatch of the magnetic susceptibility, inducing a large magnetic field gradient at the edge of the patterns (Figure 16b). The magnetic field gradient provides an attractive magnetic force that allows controlled placement of particles on the top of the patterned features during assembly. The authors demonstrated that the pattern geometry determines the assembly behavior through affecting the local magnetic field distribution. For a pattern with a small diameter of <9 μm, the magnetic field minimum appears at the center of the pattern, while for a pattern with a large diameter, two areas of magnetic field minima are located at the edge of the pattern. As a consequence, particles are trapped at the center of the small pattern and at the edge of the large pattern under the negative magnetophoretic force. For patterns with the same shape and aspect ratio, a larger pattern affects the magnetic field distribution over a greater range, causing a more efficient particle assembly.

Besides interacting directly with the magnetic field, a particle in a suspension interacts with adjacent particles due to the magnetic dipole−dipole interaction.[367] Upon exposure to an external magnetic field, a magnetic dipole is induced in a magnetic particle along the direction of the magnetic field (the direction of the induced magnetic dipole is opposite to the magnetic field in the case of a diamagnetic particle). The dipole force experienced by a second particle induced by the first particle can be expressed as[325,367]

$$F_{\text{mag-dip}} = \frac{3r(1 - 3\cos^2 \alpha)m^2}{d^4} \tag{21}$$

where α is the angle between the direction of the external magnetic field and the line connecting the centers of the two particles, r is the unit vector pointing from the first particle to the second, d is the center-to-center distance between the two particles, and m is the induced magnetic dipole moment. The magnitude and direction of the magnetic dipole force depends on the angle between the dipole moments of the two particles, where m of the first particle is taken as parallel to the external magnetic field. At the critical angle of $\alpha = 54.09°$, the magnetic dipole force is zero. For $0 < \alpha < 54.09°$, the dipole force is attractive and for $54.09° < \alpha < 90°$, it is repulsive. The dipole−dipole interaction tends to cause a chaining together of the particles similar to the effect seen in DEP where assembly is aligned along the dipole moment. These 1D particle chains have potential applications in optical devices where the orientation of the particle chain can be controlled by varying the magnetic field direction.[368−370]

Typically, magnetophoretic assembly will rely on the use of superparamagnetic nanoparticles where a particle behaves as if it is a single magnetic domain. This is an important property for the particles to possess if they are to properly respond to the applied magnetic fields used for assembly, but there is an upper size limit beyond which the particles lose their superparamagnetic properties. For example, the superparamagnetic size limit of Fe_3O_4, one of the most commonly used particles for magnetic assembly, is ~30 nm, beyond which the property fades. Because of this, there is an imposed size limit on the particles
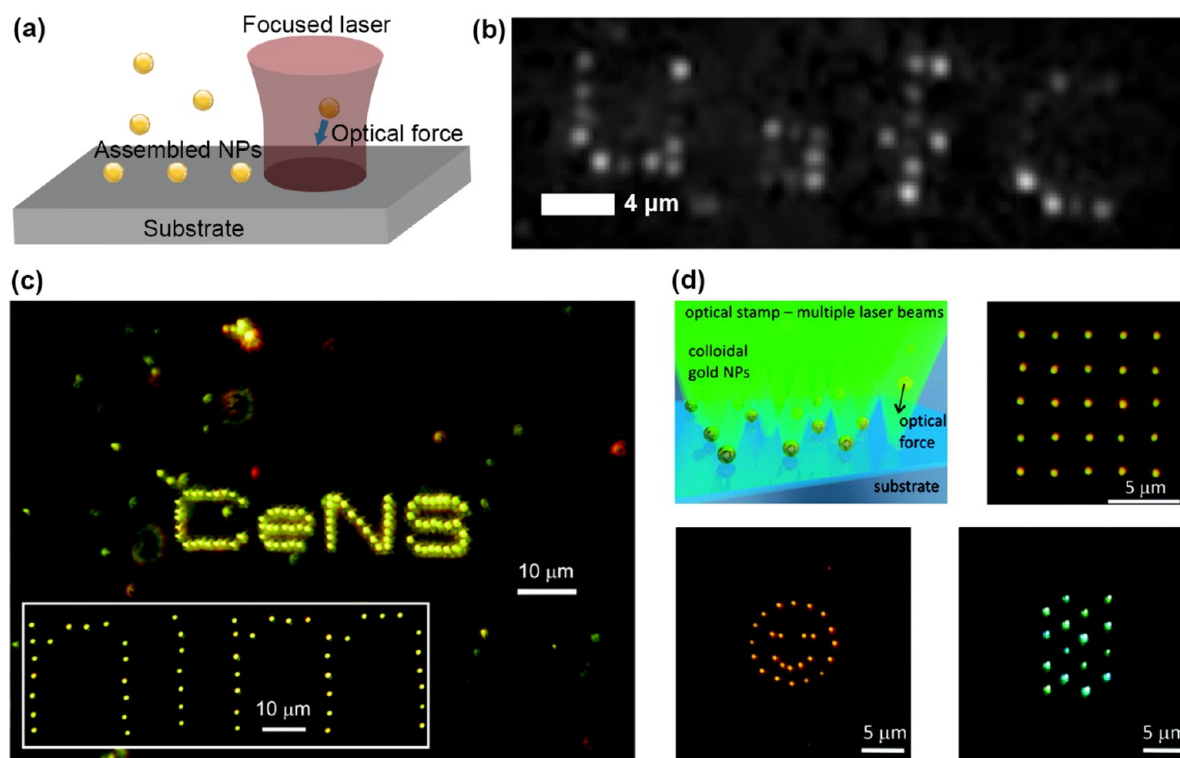
Figure 17. (a) Schematic illustration of the optical force-directed assembly process. (b) Optical tweezer-based manipulation of individual gold nanoparticles into a "U of C" pattern. Reprinted with permission from ref 391. Copyright 2010, American Chemical Society. (c) Optical printing of individual gold nanoparticles into "CeNS" and "nim" patterns. Reprinted with permission from ref 398. Copyright 2010, American Chemical Society. (d) Schematic illustration of the optical force stamping process and various stamped patterns comprised of single gold nanoparticles 80 nm in diameter. Reprinted with permission from ref 400. Copyright 2011, American Chemical Society.

used for assembly. If larger particles are desired, the limitation can be overcome by synthesizing a superparamagnetic core particle with a shell of a different material such as SiO_2.

One method that could prove very amenable to nanomanufacturing is the assembly of particles through use of the magnetic bits used for storing data.[347,371−374] Magnetic storage media, such as a hard disk drive or magnetic tape, is composed of bits with a spatial region as small as 25×25 nm^2 with the boundary between bits being ∼3 nm.[347] This small separation between magnetic domains creates a very strong magnetic field gradient that can be used to attract magnetic particles to the lines which separate the domains. The pattern of the magnetic field imprinted into the storage media can be written using commercially available read/write heads such as those used to record information to a hard disk. By writing the desired pattern onto the storage media, magnetic nanoparticles can be made to form any pattern that is desired simply by submerging the medium into a suspension of magnetic particles. Patterned lines less than 100 nm wide can be made with relative ease using this method without the need for lithography. Chains of single particles could also be made if the deposition parameters are properly optimized.[347] Once assembled, the particles can then be printed onto a different substrate for practical applications. Henderson et al. have demonstrated this by first assembling particles on the magnetic storage medium and spin-coating the surface with polymer to yield a film of 200−500 nm in thickness.[372] After curing, this thin film can be removed while retaining the deposited particles, yielding thin-film diffraction gratings in this case.

Magnetophoretic assembly can also be combined with electric fields to improve the precision of assembly. Singh et al.[375] assembled aligned single nickel nanowires between patterned electrodes with a high positioning accuracy of 25 nm by combining magnetic and electric fields. The electric field exerted a DEP force on the nickel nanowire and attracted the nanowire close to the electrodes where the magnetic field took effect, capturing the nanowire and placing the nanowire precisely on top of the electrodes.

Summary and Perspective for the Magnetic Field-Directed Assembly. As overviewed above, magnetic field-directed assembly utilizes magnetophoresis to direct particle assembly. Typically, the particles to be assembled should be either magnetic or suspended in a magnetic medium. The magnitude of the magnetophoretic force depends on the volume of the particles, the susceptibility contrast between the particles and the surrounding medium, and the magnetic field gradient. Although magnetic field-directed assembly has been extensively studied, most of the studies focus on the assembly of micro or submicron scale particles.[356] This is because the magnetophoretic force is a function of particle size. Since the magnetophoretic force scales with the particle volume, micro-scale particles with a large diameter tend to possess a large magnetophoretic force and thus are more easily manipulated. According to eq 20, one way to increase the magnetophoretic force is to increase the difference in magnetic susceptibility between the particle and the suspending medium. This method has been attempted by He et al. for the assembly of nanoscale diamagnetic particles.[370] The authors employed magnetite nanoparticles with a high surface charge and produced a stable and highly concentrated ferrofluid. As the high magnetite nanoparticle concentration increases the magnetic susceptibility of the medium, a high contrast in magnetic susceptibility is
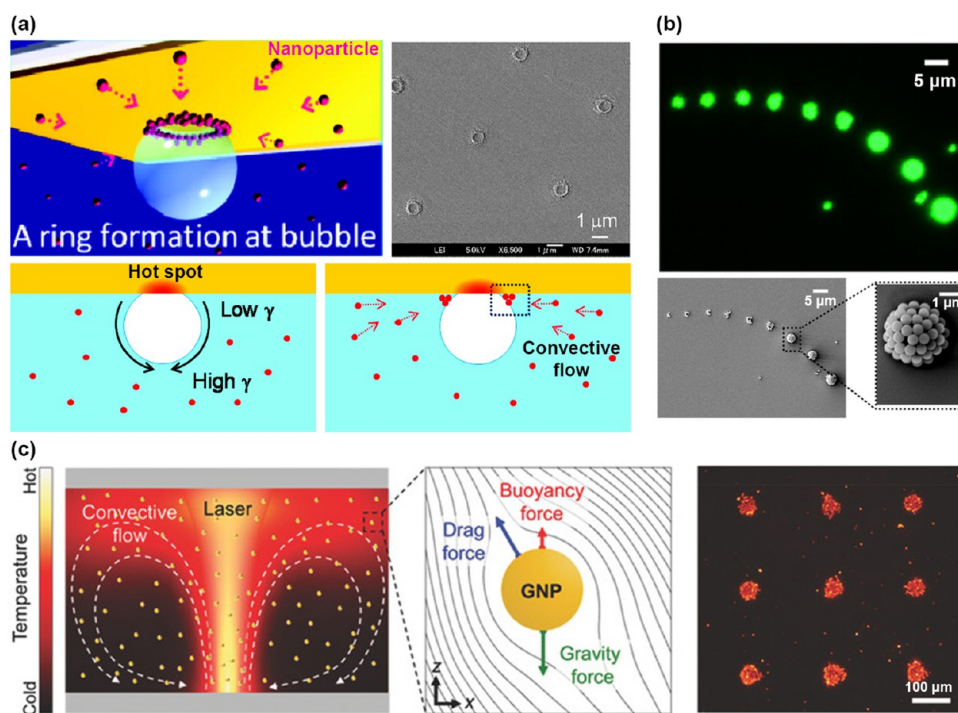
Figure 18. (a) Schematic illustration of the bubble printing process. The SEM image shows an array of ring structures composed of quantum dots fabricated by the bubble printing process. Reprinted with permission from ref 405. Copyright 2011, American Chemical Society. (b) Fabricated 3D hollow structures replicating the whole microbubbles. Reprinted with permission from ref 406. Copyright 2016, American Chemical Society. (c) Schematic illustration of the natural convective flow-directed particle assembly and the resulting array of gold nanorod assemblies. Reprinted with permission from ref 420. Copyright 2018, Wiley-VCH.

created, leading to a large magnetophoretic force. Using this approach, assembly of nanoparticles with a diameter down to 185 nm has been demonstrated. Further increasing the concentration of magnetite nanoparticles in the ferrofluid may allow the assembly of even smaller nanoparticles. Another way to increase the magnetophoretic force is to increase the magnetic field gradient. This may be realized by tuning the magnetic field distribution via adjusting the design of the micromagnets. It remains to be seen which method could yield nanoscale particle assembly under a magnetic field.

Many of the magnetic assembly methods previously mentioned are not amenable for applications related to electronics and sensors. For example, applying a magnetic field to a colloidal suspension of magnetic particles is useful for creating photonic crystals, and using magnetic fields can be useful for separating particles for biological applications, but this is not as useful for assembly where particles need to be arranged into patterns which have no periodicity. To do this, magnetic substrates must be prepared which demonstrate strong magnetic field gradients when an external field is applied. This could prove difficult for assembly at scale where an entire wafer would need to be exposed to a uniform magnetic field within a ferrofluid. The most promising method for electronics and sensors is assembly via magnetic recording media which can be used for transfer printing. Additionally, this method does not require the use of photolithography or etching. With further development, this method could allow single-file lines of nanoparticles to be assembled.

OPTICAL FIELD-DIRECTED ASSEMBLY

Optical Force-Directed Assembly. In addition to flow, electric, and magnetic fields, light can also provide a force to

direct particle assembly.[376−379] The manipulation of particles by optical force was used by Ashkin et al. at AT&T Bell Laboratories in 1986.[380] The authors demonstrated that dielectric particles with size from 10 μm down to ∼25 nm could be successfully trapped by the optical field. Since then, interest in the optical manipulation of particles has been growing. In 1994, Svoboda et al.[381] demonstrated that metallic nanoparticles could also be manipulated through the optical force. Gold nanoparticles 36 nm in diameter were shown to experience a larger optical force than dielectric latex nanoparticles 38 nm in diameter. Later on, Hansen et al.[382] expanded the size of trapped gold nanoparticles to 18−254 nm in diameter. The manipulation of silver nanoparticles,[383,384] Au nanorods,[385] Au bipyramidal nanoparticles,[386] and quantum dots[387] was also demonstrated.

The optical force, including the scattering force and the gradient force, arises from the interaction of strongly focused light on the particles (Figure 17a).[388] For particles with diameters much smaller than the wavelength of the light, electric dipole moments are induced across the particles in response to the light's electric field.[389,390] Because the incident light is focused using an objective lens of large numerical aperture, the local electric field is very nonuniform, resulting in the gradient force that directs the polarized particles toward the focal point where the light intensity is greatest. Moreover, the incident light can be absorbed or re-emitted by the particles. The momentum of the light is thus partially transferred to the particles, causing the scattering force and pushing the particles along the direction of light propagation. The gradient force is proportional to the gradient of light intensity, while the scattering force is proportional to the light intensity.

When the wavelength of the incident light is far above the surface plasmon resonance wavelength of the particles, the optical force is dominated by the gradient force, which tends to attract the particles toward the focal region.[382,383] As soon as the position of the focal point is changed, the particles move to the new focal point promptly. This technique of using highly focused light for the manipulation of particles is often called optical tweezers or an optical trap. Guffey et al.[391] utilized the optical tweezer method to place single gold nanoparticles 40 nm in diameter on glass substrates with a subwavelength precision (∼100 nm standard deviation). Single particles were first trapped in a bulk suspension by a highly focused light, and then brought into contact with the substrates by manually changing the fine focus of the microscope. By controlling the sample position using a piezoelectric translation stage, a "U of C" pattern made of gold nanoparticles was fabricated in ∼1 h (Figure 17b).

To enhance the interaction between the incident light and the particles, light of a wavelength comparable to the plasmon resonance of the particles can be utilized for particle manipulation.[392] As the incident light is mostly absorbed by the particles, the scattering force becomes dominant.[382,383] Instead of attracting particles, the scattering force pushes the particles along the beam path away from the focal area. The fabrication process using the scattering force as the driving force is termed as optical printing.[393−399] Employing the optical printing method, Urban et al.[398] fabricated "CeNS" and "nim" patterns by sequentially printing individual gold nanoparticles 80 nm in diameter (Figure 17c). The authors noticed that using a lower laser power led to a higher positioning precision with a compromise of a lower printing throughput. In order to achieve a higher fabrication throughput, a spatial light modulator (SLM) is used to split a single beam into several beams for manipulating multiple nanoparticles in parallel.[400] The fabrication of a 5 × 5 array of equally spaced 80 nm gold nanoparticles took only 10 s (Figure 17d). As a parallel process, the time needed to fabricate a pattern is almost independent of the pattern size. Fabricating an 8 × 8 pattern took roughly the same time (11 s). By modifying the image displayed on the SLM, rapid and precise fabrication of arbitrary patterns can been achieved.

Compared with the optical tweezer method, optical printing allows for rapid fabrication but has limited control over the particle orientation. Do et al.[401] utilized two lasers with different wavelengths to achieve orientation control of gold nanorods. The laser that is not resonant to the surface plasmon resonance of the nanorods was used to trap and align the nanorods, while the other laser that is resonant was used to rapidly deposit the aligned nanorods. This two color optical printing process enabled gold nanorod patterns with an angular orientation of ±16°.

Optofluidic Flow-Directed Assembly. Besides generating the optical force, the interaction of an incident light with particles or substrates can cause an optofluidic flow that can be used to direct particle assembly.[402−404] Fujii et al.[405] utilized the Marangoni convection flow around a laser-induced microbubble to assemble nanoparticles (Figure 18a). The microbubble can be generated by using a continuous wave laser to heat a light absorbing substrate such as a 10−30 nm-thick gold film. There must be a target to absorb the heat of the incident laser such that the bubbles may form. This can be implemented in the form of a thin metal film or adsorbed plasmonic nanostructures that have strong absorbance at the wavelength of incident light. The formation of the microbubble is accompanied by a temperature

gradient, hotter at the base of the bubble and cooler at the top. As the hotter medium has a lower surface tension, a surface tension gradient along the surface of the microbubble is established, inducing a Marangoni convective flow that drives the medium to flow toward the top of the microbubble. To compensate for the upward Marangoni convective flow, a flow toward the bottom of the microbubble is generated, carrying nanoparticles toward the substrate-liquid-bubble interface where they assemble. The assembled structures resemble the shape of the microbubble. When the optical power is low and the assembly time is short, a small number of particles are assembled and a ring-shaped structure is formed (Figure 18a). By increasing the optical power or the assembly time, more particles are assembled and a 3D hollow structure replicating the whole microbubble is generated (Figure 18b).[406] Given the microbubble involved, the photothermal Marangoni convective flow-directed assembly process is usually referred to as bubble-pen lithography (BPL)[406] or bubble printing.[407,408] The resolution of the bubble printing process depends on the bubble size.[408] According to the power of the incident laser, the bubble size can vary from submicrometer to a few micrometers, implying a submicrometer resolution of this process. Bubble generation is also a function of the liquid components. Kim et al. included perfluoropentane in water to create a biphasic mixture. The perfluoropentane micelles have a much lower boiling point than water and have a higher gas solubility, so they act as sites of facile bubble generation requiring much less incident power.[409] The lower power input was ideal for capturing proteins that would otherwise be damaged by an intense laser. This method has been used to good effect for the creation of plasmonic aggregates of nanoparticles for biosensor applications.[410,411] Degassing the nanoparticle suspension before the bubble printing process could be a solution to achieve a smaller bubble size and thus a higher resolution.[412] By translating the microbubble or the sample stage, continuous patterns of nanoparticles can be created according to the trajectories of the bubble or the stage movement.[407,413,414] Armon et al. modulated the intensity of the laser incident on the moving substrate to create a continuous deposition of silver nanoparticles. They achieved a minimum line width of 1.4 μm at a translation speed of 30 μm s^{-1}. The particles were sintered following deposition to create conductive pathways.

In addition to the Marangoni convective flow,[415−419] another optofluidic flow, natural convective flow, can be induced when heating plasmonic particles or substrates.[420] The convection originates from the buoyant force generated by the density difference across the suspension in the temperature gradient. Utilizing the natural convective flow, Jin et al.[420] demonstrated the assembly of three types of colloidal gold nanoparticles with various shapes (rod, star, and sphere) at the focal point of the incident light (Figure 18c). Controlling the size of the assembled structures was achieved by adjusting the light intensity and the illumination time.

Summary and Perspective for the Optical Field-Directed Assembly. The optical force-directed assembly enables direct fabrication of arbitrary patterns without the need for a template on the substrate. However, the patterns fabricated by optical force-directed assembly are often confined to arrays consisting of isolated individual nanoparticles, which limits its versatility. In addition, the optical force-directed assembly process usually requires a strongly focused laser with a high power, which may damage the nanoparticles and thus further limits its capabilities.
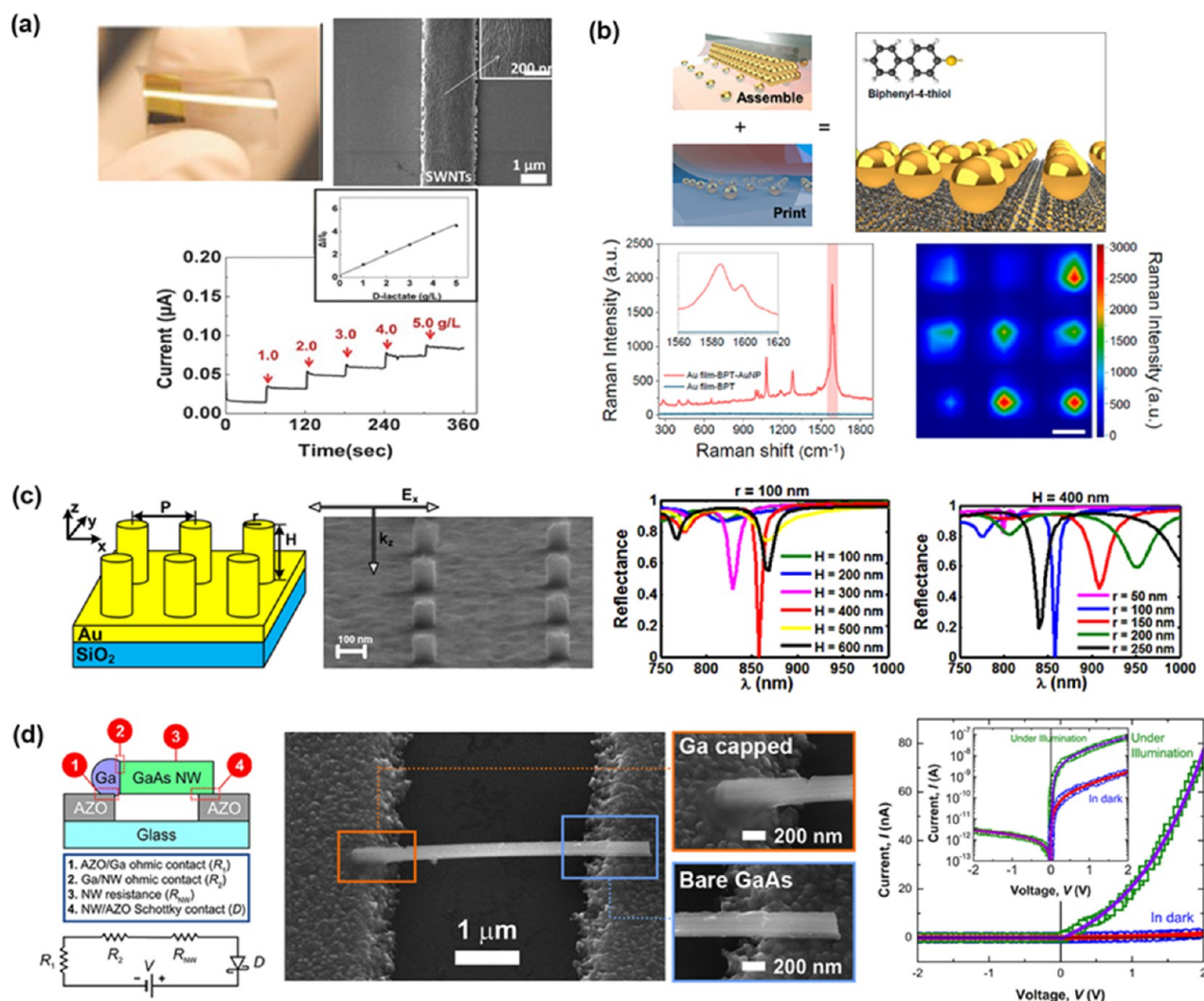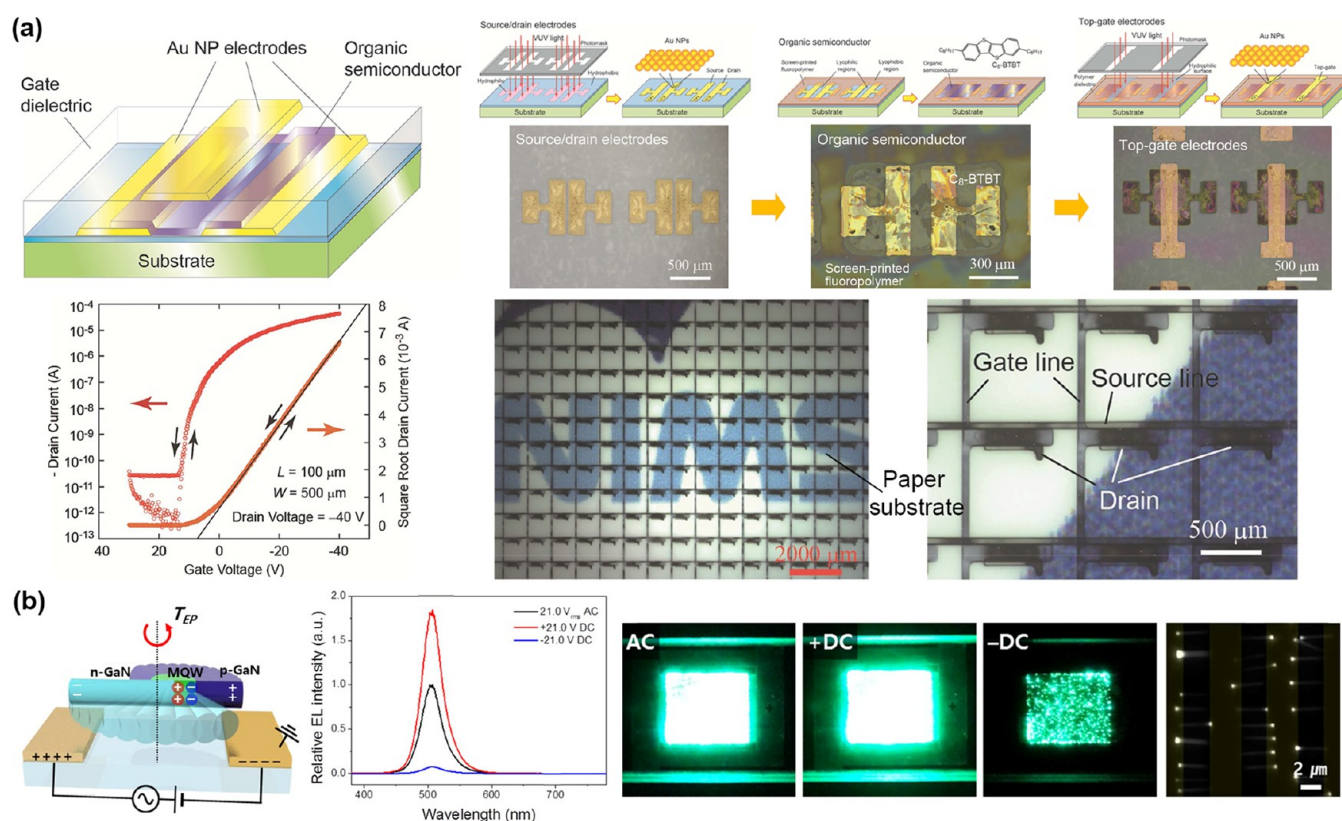
Figure 19. Sensors fabricated utilizing directed assembly processes. (a) Fabrication of flexible biosensors using SWCNTs and the electro-fluidic assembly process. Reprinted with permission from ref 321. Copyright 2015, Wiley-VCH. (b) Fabrication of arrayed gold nanoparticles by combining capillary assembly and transfer printing processes for SERS detection of BPT monolayer. Reprinted with permission from ref 436. Copyright 2020, American Chemical Society. (c) Fabrication of gold antenna array by DEP assembly process for optical trapping. Reprinted with permission from ref 208. Copyright 2011, AIP Publishing. (d) Fabrication of GaAs nanowire-based photodetectors using the DEP assembly process. Reprinted with permission under a Creative Commons CC BY 4.0 License https://creativecommons.org/licenses/by/4.0/ from ref 189. Copyright 2020, IOP Publishing Ltd.

Like the optical force-directed assembly process, the optofluidic flow-directed assembly allows direct fabrication of arbitrary patterns without prepatterning of substrates. One advantage is that the optofluidic flow-directed assembly can be realized through a weakly focused laser with a low laser power which avoids damage to the colloidal nanoparticles. However, the resolution of the optofluidic flow-directed assembly is limited to micro or submicroscale. This could be addressed by combining the method with physically or chemically patterned substrates.

Other methods for particle manipulation are available which rely on thermal flows caused by optical heating, but these will not be covered here as they require the use of elaborate methods that are not amenable to scalable production. These methods can be found in other review articles specifically about the optical manipulation of nanoparticles.[376] The optical methods discussed here can achieve molecular precision and can be used to assemble particles in arbitrary shapes without the need for conventional lithography, which is useful for the creation of

sensors that rely on a plasmonic response. For instance, BPL can produce rings of particles that display a precise plasmonic resonance to be used as sensors.[415] However, the scalability of the optical methods is hindered by the in-series nature of the laser-guided assembly and the complexity of the apparatus involved. The scalability can be improved somewhat through the use of beam splitters as demonstrated by Nedev et al.[400] Also at issue is the requirement of the proper substrate for optofluidic methods that rely on heating and cavitation for particle manipulation. These methods require a substrate than can be heated through absorbing the incident laser light, and thus must be made from a metallic thin film, plasmonic assembly of islands or particles, or have plasmonic particles in close proximity to the surface. Resolution may be limited to ~300 nm between particles due to the optical absorbance and heating of previously deposited particles causing repulsive photothermal flows which could be overcome if the substrate is very efficient at spreading heat.[394] The heating itself may be an issue if biological molecules are involved that can be damaged by the laser. Overall, the

Figure 20. Electronics fabricated utilizing directed assembly processes. (a) Schematic illustration of a TFT consisting of a semiconducting channel, source/drain electrodes, a dielectric layer and a gate electrode. TFT arrays were fabricated via sequential assembly of each layer. An OTFT active-matrix array assembled on a paper substrate was also demonstrated. Reprinted with permission from ref 443. Copyright 2014, Wiley-VCH. (b) Fabrication of LEDs via EP and DEP-directed assembly of p/MQW/n InGaN nanorods between planar electrodes. Reprinted with permission from ref 446. Copyright 2017, American Chemical Society.

optical assembly methods can be very useful for producing sensors that rely on plasmonics. It is also possible to print metal using the optothermal methods shown here,[421] but we have chosen to focus on methods that demonstrate the assembly of particles as opposed to the photochemical reactions.

Devices Made Using Directed Assembly. In this section, we give examples of devices fabricated using the assembly methods reviewed above in addition to the examples already mentioned in brief.

Sensors. Owing to the merits of high surface-to-volume ratio, high surface energy, and high reactivity, nanoelements have stimulated increasing interest in the construction of gas sensors,[422] chemical sensors,[423] and biosensors.[321,424] Jung et al.[422] fabricated hydrogen sulfide (H_2S) sensors using assembled SWCNTs as active layers. A concentration of H_2S in the range of 10 to 100 ppm were successfully detected. They found that the 2,2,6,6-tetramethylpiperidine-1-oxyl used to functionalize the SWCNTs and water in the humid air were significant in promoting redox reactions that allowed detection of the H_2S. At a relative humidity of 60%, a very high sensitivity of 420% was achieved. Similarly, Yilmaz et al.[122] used assembled SWCNTs to detect nitrogen dioxide (NO_2) with a concentration down to 1 ppm. Cho et al.[321] fabricated flexible biosensors using SWCNTs as active layers (Figure 19a). The SWCNTs were assembled via the electro-fluidic assembly process and then functionalized with lactate oxidase (LOD). The LOD can oxide lactate into pyruvate, producing an electrocatalytic current which is transferred to the SWCNTs and affects their conductivity. By detecting the change in conductivity, the concentration of

lactate in the range of $1-5$ g L^{-1} was detected. The three types of sensors mentioned above are all based on assembled SWCNTs. However, detection of a particular substance was achieved due to functionalization of the SWCNTs, meaning the possibility of fabricating an integrated platform capable of sensing many different chemicals for the emerging applications of wearable healthcare-related devices. Besides CNTs, tin oxide (SnO_2) nanoparticles,[425] palladium nanoparticles,[81] InAs nanowires,[192] tungsten oxide nanowires,[426] and graphene oxide nanostructures[86] have been assembled and employed as sensing layers.

Nanoelements composed of noble metals, especially gold and silver, exhibit strong light scattering and absorption on account of their localized surface plasmon resonance properties.[427] Assembly of individual nanoelements into clusters such as dimers, trimers, and oligomers[267,275,428] leads to enhanced light scattering and absorption as well as a shift of plasmonic resonances because of near-field coupling of LSPs between adjacent nanoelements, while assembly of individual nanoelement or their clusters into ordered arrays with spacing comparable to the wavelength of the incident light leads to drastic narrowing of plasmon resonances due to far-field coupling of LSPs.[427,429,430] The optical properties of the nanostructures have drawn enormous attention in applications such as surface-enhanced Raman scattering (SERS),[277,280,281,431,432] antennas,[208,433] plasmonic pixel arrays,[130,434] and information encryption.[279,435] Lee et al.[436] fabricated arrayed gold nanoparticles by combining capillary assembly and transfer printing for SERS detection of a biphenyl-4-thiol (BPT) monolayer (Figure 19b). A BTP coated gold film
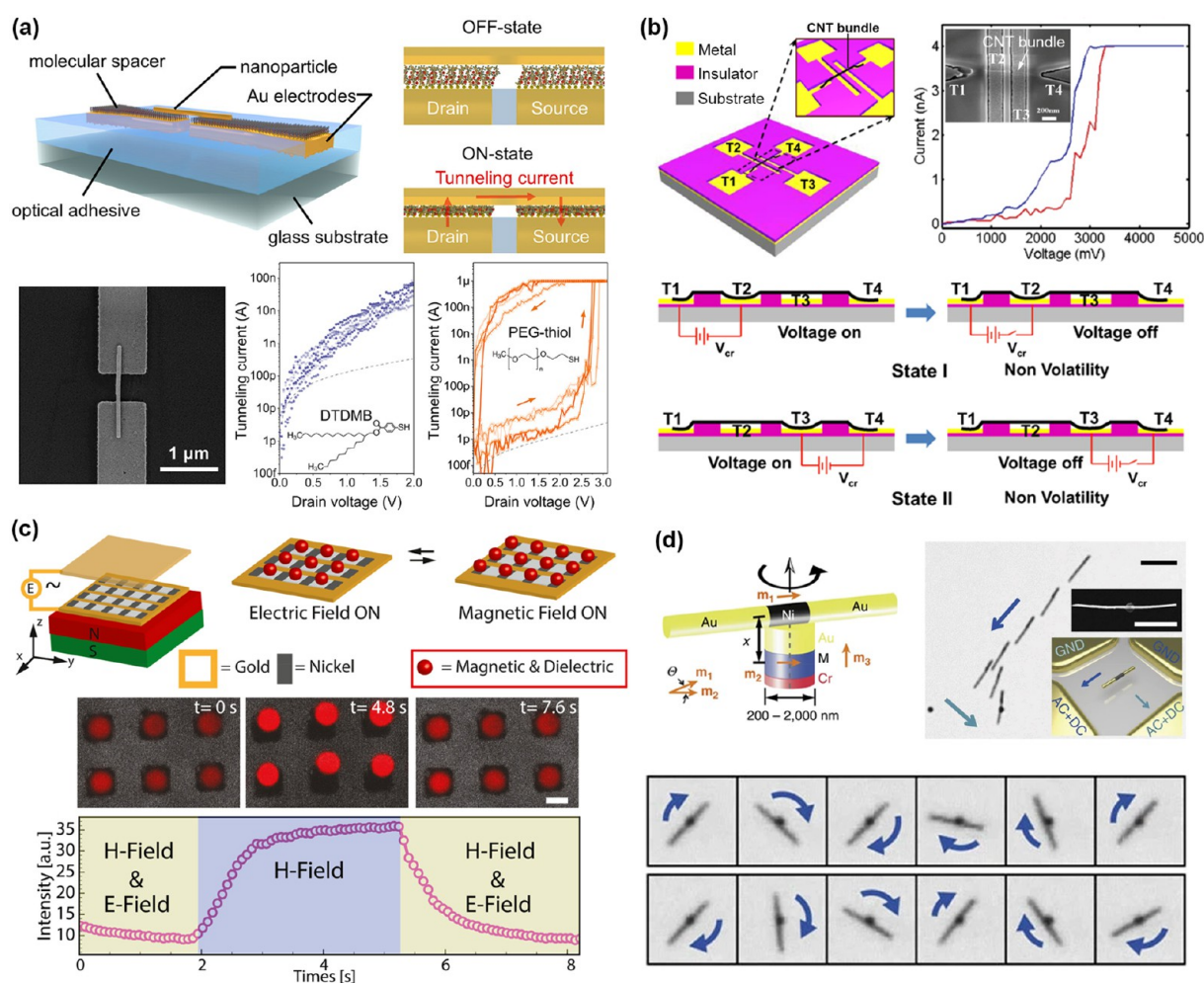
Figure 21. NEMS fabricated utilizing the directed assembly process. (a) Fabrication of NEM switches using DEP assembled gold nanorods as active components. Reprinted with permission from ref 448. Copyright 2021, American Chemical Society. (b) Fabrication of bistable switches using DEP assembled aligned SWCNTs as active components. Reprinted with permission from ref 185. Copyright 2020, IOP Publishing. (c) Fabrication of optical switches via assembly of colloidal particles between the magnetic and electric potential minima. Reprinted with permission from ref 360. Copyright 2017, American Chemical Society. (d) Fabrication of ultrahigh-speed rotary nanomotors utilizing assembled Au/Ni/Au nanowires as rotors. Reprinted with permission from ref 451. Copyright 2014, Nature Publishing Group.

Table 1. Selected References Regarding Influencing Parameters of Each Electrokinetic Phenomenon

	Influencing parameters	EP	DEP	EOF	EHD flow
Electric field parameters	DC or AC	140, 144	146	N/A	220, 240
	Field strength	122, 133	171, 173	119	221, 224, 235
	Frequency	142, 143	83, 171, 173	N/A	172, 224, 235
	Particle size	131	161, 169	N/A	224, 234, 235
	Conductivity and permittivity of particles	N/A	148, 205	N/A	N/A
Suspension properties	Conductivity and permittivity of a medium	N/A	171, 241	N/A	N/A
	pH	122, 138	N/A	N/A	228
	Electrolyte concentration	117, 130	N/A	119, 242	224, 229, 235
	Pattern geometry	129, 133	121, 161, 176	218	224, 234, 235

sample was used as a comparison. The results revealed that two characteristic peaks for BTP at 1580 and 1600 cm^{-1} were detected when the array of gold nanoparticles was present. Cetin et al.[208] fabricated gold nanopillar antenna arrays using the DEP assembly process (Figure 19c). The authors demonstrated that the resonance behavior of the nanopillars depends strongly on the height, radius and periodicity of the nanopillars.

As sensors for light detection, photodetectors can have numerous applications including thermal imaging, remote sensing, night vision, medical imaging as well as virtual reality and augmented reality displays. Fabrication of photodetectors using the directed assembly process has also been demonstrated.[186,189,437,438] García Núñez et al.[189] used DEP to fabricate photodetectors from GaAs nanowires (Figure 19d). Individual GaAs nanowires 35−50 nm in radius and 3−5 μm in length were assembled between patterned electrodes at a high assembly yield of >90% and alignment yield of >95%. One end of the GaAs nanowires were capped with gallium which formed

Table 2. Summary of the Main Directed Assembly Techniques

Assembly techniques	Driving forces	Influencing parameters	Advantages	Disadvantages
Electric field-directed assembly — Electrophoretic	Electrophoretic force	(1) Electric field parameters: type of electric field, field strength and gradient, and frequency	(1) High scalability: without dimension limitation	(1) Systematic studies of the effect of electrokinetic phenomena on the particle assembly is lacking
Dielectrophoretic	Dielectrophoretic force	(2) Suspension parameters: particle size, conductivity and permittivity of particles and medium, pH, electrolyte concentration	(2) High throughput: parallel process, rapid assembly within 1 min	(2) Conductive substrates are usually required
Electrokinetic flow	Electroosmotic flow; Electrohydrodynamic flow	(3) Pattern geometry	(3) High resolution: single nanoparticle level (4) Multiscale: from nano to micro (5) Material independent: zero, one and two-dimensional, insulating, semiconducting, and conducting	
Magnetic field-directed assembly — Magnetophoretic	Magnetophoretic force	(1) Magnetic field gradient (2) Suspension parameters: particle size, susceptibility contrast between particles and medium (3) Pattern geometry	(1) High scalability: without dimension limitation (2) High throughput: parallel process	(1) Particles need to be either magnetic or suspended in a magnetic medium. (2) Low resolution: submicron
Optical field-directed assembly — Optical force	Gradient force; Scattering force; Marangoni convective flow	Difference between the wavelength of incident light and the surface plasmon resonance wavelength of particles	(1) High resolution: single nanoparticle level (optical force-directed assembly)	(1) Low scalability (2) Low throughput: serial process (3) High light power needed (optical force-directed assembly)
Optofluidic flow	Natural convective flow	(1) Power of the incident laser (2) Liquid component	(2) Material independent (3) No need to prepattern substrates	(4) Low resolution: submicron (optofluidic flow-directed assembly)
Fluidic flow-directed assembly — Convective assembly	Convective flow and immersion capillary force	(1) Patterned substrate: wetting behavior, geometry	(1) High resolution: single nanoparticle level	(1) Low scalability
Capillary assembly	Convective flow and capillary force	(2) Environment parameters: substrate temperature, relative humidity	(2) Multiscale: from nano to micro	(2) Low throughput: serial process, parallel in the direction perpendicular to the meniscus moving direction
Fluidic assembly	Convective flow, immersion capillary force, and capillary force	(3) Material independent	(3) Meniscus moving speed	
Fast fluidic assembly	Surface adhesion force	(1) Patterned substrate: wetting behavior, functional groups, geometry (2) Suspension parameters: viscosity, surface tension (3) Meniscus moving speed	(1) High scalability: without dimension limitation (2) High throughput: meniscus moving speed in tens of millimeters per second (3) Material independent	(1) Low resolution: millimeter or submillimeter (2) Difficult to fabricate loop structures
Interfacial convective assembly	Solutal Marangoni convective flow	(1) Solvent component of the nanoparticle suspension (2) Substrate temperature	(1) High scalability: without dimension limitation (2) High throughput: parallel process (3) High resolution: single nanoparticle level (4) Multiscale: from nano to micro (5) Material independent	More in-depth studies of the origination and the controlling parameters of the solutal Marangoni flow are needed.

Table 3. Selected References in Electrophoretic Assembly

Ref	Type	Material	Assembly parameters	Application
123	aligned nanorods, 40 nm in length	CdS, CdSe, in toluene	30−50 V for 10−15 min	
124	Quantum dots	CdSe/ZnS	20 V for 5 min	LED
125	Aligned nanorods	MnO2	800 V for 30 s	Redox capacitors
126	Quantum dots	CdSe	200 V for 2 h	Photovoltaics
127	Particles 150−450 nm in size	PSL	5−20 V for 1−10 min	Sensor, oxygen
128	Quantum dots, microtrenches	ZnO	20−100 V for 1−60 min	
129, 256	Nanoparticles, microtrenches	PSL and silica	2 V for 90 s	
130	Nanoparticles and nanorods, nanoscale patterns	Au	0.5−2.5 V mm^{-1} up to 16 s	
131	50−200 nm in size, nanoscale patterns	PSL	2−3 V for 1−2 min	Sensor, bio
132	10−20 nm in size, film	Au	1.2 V	SERS platform
133	2 μm particles, microscale patterns	PSL	10−17.5 V cm^{-1}	
136	10 nm particles, film	ZnO	<5 V	
140	0.5 and 1 μm particles, microscale patterns	PSL	270 V cm^{-1} for ms pulses	Sensor, bio
141	80 nm particles	Alumina	20−100 V cm^{-1} for 10−70 min	

an ohmic contact with Al-doped ZnO (AZO) electrodes, while the other ends were bare GaAs which formed Schottky contacts with the AZO electrodes. The fabricated photodetectors exhibited rectifying behavior. Under illumination with visible light, the forward current increased by 2 orders of magnitude due to the photogeneration of charge carriers.

Electronics. Thin film transistors (TFTs) are used in many applications such as flat-panel displays, radiofrequency identification (RFID) tags, *etc.*[439] TFTs consist of four layers, including a semiconducting channel, source/drain electrodes, a dielectric layer and a gate electrode (Figure 20 (a)),[440] and require precise alignment between the layers. So far, directed assembly based fabrication of TFTs focuses mainly on the semiconducting channel. The assembly of 0D (CdSeS/ZnS quantum dots,[441] etc.), 1D (SWCNTs,[184,203,442] silicon nanowires,[193,194] InAs nanowires,[320] etc.), and 2D (graphene,[88] molybdenum disulfide (MoS$_2$),[441] etc.) semiconductors has been extensively studied though layer-by-layer fabrication of TFTs was rarely demonstrated in the literature. Minari et al.[443] fabricated large-area TFT arrays via sequential assembly of gold source/drain electrodes, a dioctylbenzothienobenzothiophene (C8-BTBT) semiconducting channel layer, and a gold gate electrode (Figure 20a). The fabricated TFTs exhibited on/off ratios of >10^6 and average field-effect mobilities of 7.9 cm^2 V^{-1} s^{-1}.[443,444] An organic thin-film transistor (OTFT) active-matrix array assembled on a paper substrate was also demonstrated.[443] More studies on the fabrication of TFTs using directed assembly are highly desirable in the future.

Besides TFTs, light-emitting diodes (LEDs) are another extensivly studied application.[124,445−447] Eo et al.[446] fabricated LEDs via EP and DEP-directed assembly of p-GaN/InGaN multiquantum-well/n-GaN (p/MQW/n-InGaN) nanorods between planar electrodes (Figure 20b). A DC offset was added to the AC electric field to controll the orientation of the nanorods. Around ~74% p-GaN ends contacted with the positively charged electrode after assembly, which was significantly higher than ~40% when only an AC field was applied. Due to the alignment of the nanorods, the intensity of the electroluminescence was improved by 1.8 times. Although LED devices were demonstrated,[446] site-selective assembly of single color, precisely aligned, and single nanorod arrays between prepatterned electrodes will bring the devices closer to practical applications.

Nanoelectromechanical systems (NEMS). The continuous miniaturization of CMOS field-effect transistors (FETs) faces challenges related to off-state current leakage and power dissipation.[448] NEM switches have attracted attention in recent years due to their merits of near zero off-state current, steep subthreshold slopes, and robustness in extreme environments.[448−450] Han et al.[448] fabricated NEM switches using DEP assembled gold nanorods as active components (Figure 21a). Single gold nanorods were bridged between a pair of gold electrodes with self-assembled molecular spacers between the nanorod and electrodes. Applying a drain voltage induced electrostatic attraction between the gold nanorod and the gold electrodes, compressing the molecular spaces and leading to a tunneling current. As a consequence, the switch functioned with an on/off current ratio of several orders of magnitude. In some occasions like nonvolatile memories, switches need to remain on when the applied voltage is turned off. To realize this goal, Abbasi et al.[185] fabricated bistable switches using DEP assembled aligned SWCNTs as active components (Figure 21b). The SWCNT bundles were assembled between two electrodes (T1 and T4) while being suspended over a different set of electrodes (T2 and T3) positioned perpendicular to the SWCNT bundles. When applying electric potential between T1 and T2 electrodes, the SWCNT bundles would bend and adhere to the lower electrode establishing a connection between the T1 and T2 electrodes. This conncection state (state I) was nonvolatile because the SWCNT bundles and T2 electrode remained connected even after the applied potential was off. Under State I, when a sufficient potential was applied between T3 and T4 electrodes, the SWCNT bundles would leave the T2 electrode and connect with T3 electrode (state II), establishing connection between T3 and T4. Again, the state II connection was also nonvoltile. The bistable swiches worked under a low actuation voltage of 5 V and exhibited a on/off ratio of >10^5. The initial assembly of the SWCNTs was only possible by driving an AC voltage through both sets of electrodes, but with a phase difference of 180°.

Besides electronic switches, Demirörs et al.[360] fabricated optical switches via assembly of colloidal particles between their magnetic and electric potential minima (Figure 21c). Substrates with micropatterned gold electrodes and nickel micromagnets were fabricated and utilized to direct the assembly of magnetodielectric colloidal particles. The dielectric constant of the particles is smaller than that of the surrounding medium. When an electric field was applied, the particles assembled to the voids on the gold film where the electric field is low under the DEP force, while when a magnetic field was applied, the particles

Table 4. Selected References for Dielectrophoretic Assembly

Ref	type	Material	Assembly parameters	Application
79	∼9 nm particles in 60 nm gap	ZnO	2 Vpp, 30 s, 150 kHz	UV photodetector
80	4 nm particles in 2 μm gap	CdTe	4−10 Vpp, 20 MHz	UV photodetector
160	10−120 nm particles in 20−500 nm gap	Au	1−2 Vpp, several seconds to 1 min, 1 MHz	Nanowires
161	5, 10, 20 nm particles in 20 nm gap	Au	2−3 Vpp, 1 MHz, 1 s	
162	2.5 nm particles in 200 μm gap	Au	5−10 Vpp, 100 Hz to 10 MHz	
85	30 × 11 nm rods in 100 μm gap	Au	60 Vpp, 100−400 kHz	Microscale interconnects
164	5−30 nm particles in 1 μm or 15 μm gap	Au	3−8 Vpp, 0.02−1 MHz	
168	5, 10, 20 nm particles in 3 μm or 100 μm gap	Au	7.5 Vpp, 10 Hz to 1 MHz	
173	20 nm particles in 15−150 nm gap	Au	1−6 Vpp, 1 MHz, 120 s	
175	20 nm particles in 200 nm gap	Au	3 Vpp, 1 MHz, 1−2 s	Single-electron transistors
176	Particles in 9 nm gap	PSL, nanodiamonds, CdSe QDs	up to 1 Vpp, MHz range	
179	1.5 μm nanotubes, 1−100 μm channel	mixed CNTs	2 V DC during dip coating	Strain sensor
180	Nanotubes in 2 μm gap	SWCNT	5 Vpp, 500 kHz	
181	Nanotubes in 5 μm gap	SWCNT	5 Vpp, 300 kHz, 15 s	FETs
182	0.2−2 μm nanotubes in 0.8 μm gap	SWCNT	2 Vpp, 300 kHz	
184	Nanotubes at edge of electrode	SWCNT	5 Vpp, 400 kHz, 4 min	FETs
185	Nanotubes in 500 nm gap	SWCNT	2 Vpp, 1 MHz	Electromechanical switch
186	50 μm nanowires with 30−500 nm nanotubes in 10 or 25 μm gap	Ag/ZnO	30 or 50 Vpp at 100 kHz	Photodetector
187	Nanowire in 0.4−3 μm gap	Au	2−10 Vpp, 2−20 MHz	
188	3−5 μm nanowires in 3 μm gap	Au, Pt, SnO	0.01 Vpp, 100 kHz, 1−6 min	
189	35−50 nm × 3−5 μm nanowires in 2 μm gap	GaAs	7 Vpp, 10 kHz to 1 MHz, 2 min	Photodetector
190	0.1 × 10−80 μm nanowire, simulation	GaN	20 Vpp, 1 kHz	
191	5−10 μm nanowire in 4 μm gap	GaN	1- 20 Vpp, 10 kHz and 20 MHz	p−n junction
192	Nanowire in 2 or 5 μm gap	InAs	5 or 10 Vpp, 1 kHz to 1 MHz	Sensor, gas
193	22 μm nanowire in 150 μm gap	Si	10 Vpp, 1 kHz to 20 MHz, 60 s	
194	1−20 μm nanowires in 10 or 20 μm gap	Si	5−20 Vpp, 4 kHz to 5 MHz	FETs, selectivity
195	∼15 μm nanowire in 12 μm gap	Si	150−450 mVpp, 500 Hz	
196	1−12 μm nanowires in 600 nm gap	MnO$_2$	1−2 Vpp, 1 MHz, 0−60 s	
197	3 μm nanowires in 800 nm gap	MnO$_2$	1 Vpp, up to 10 MHz, 1 min	
198	Nanofibers in 5 μm gap	Coronene tetracarboxylate and dodecyl methyl viologen	2 Vpp, 500 Hz	Supercapacitor
199	8 μm nanowires in 3 μm gap	DNA coated wires	4.2 Vpp, 1 MHz	
200	∼15 μm nanowire in 10 μm gap	InAs	5 Vpp, 10 MHz	
203	nanotubes in 2, 5, 10 μm gap	SWCNT	5 Vpp, 300 kHz, 30 s	FETs, aligned arrays
204	2D sheet in 3 μm gap	WS$_2$	15 Vpp, 100 kHz	
205	20 nm particles in 20−200 nm vias	Silica	2 V$_{DC}$, 12 Vpp, 50 kHz, several min	Plasmonics, printing
206	15−100 nm particles collected on AFM tip or 80 nm gap	Ag, Au	1−20 Vpp, 1 MHz	Tip-enhanced Raman
207	50 nm particles in 100−500 nm vias	Au	2 V$_{DC}$, 12 Vpp, 10 kHz, 90 s	
208	Particles in 50−250 nm vias	Au	2 V$_{DC}$, 12 Vpp, 50 kHz	Plasmonics

assembled at the nickel micromagnets under the magnetophoretic force. The intensity of the fluorescence of the assembled particles varied as the electric and magnetic fields switched, behaving like optical switches.

Kim et al.[451] fabricated ultrahigh-speed rotary nanomotors utilizing Au/Ni/Au nanowires as rotors, patterned Au/Ni/Cr nanomagnets as bearings and quadrupole microelectrodes as stators (Figure 21d). The nanowires 150−400 nm in diameter and 800−1000 nm in length were precisely assembled on the nanomagnets by using "electric tweezers"[452] (based on EP and DEP forces). When applying four AC voltages with a phase shift of 90° on the quadrupole microelectrodes, the assembled nanowires rotate with speed up to 18,000 rpm. By rotating continuously for 15 h, over 240,000 cycles were achieved.

SUMMARY

This review documents recent progress in the directed assembly of nanomaterials (nanoparticles, nanorods, nanotubes, nanowires, etc.) for making nanoscale devices and structures. Unlike the directed self-assembly process which utilizes external fields to enhance interelement interactions, the directed assembly fabrication process utilizes external fields to directly interact with nanoelements and direct them into predefined patterns on a substrate to form nanoscale functional structures. This review is focused on four main external fields used in directed assembly: electric, fluidic flow, magnetic, and optical. The underlying mechanism of how these external fields interact with the nanoelements to generate the driving forces, the influencing parameters and control of the driving forces, and the advantages and disadvantages of each external field-directed assembly

Table 5. Selected References for Electrokinetic Flow

Ref	Type	Material	Parameters	Application
211	40 nm particles, 5 mm spacing, monolayer	Au	1.2 V, 10 min	Plasmonics/chemical reaction platform
212	~6 nm particles, 340 μm spacing, monolayer	Au, Ag	2−20 Vpp, 300 kHz	
213	4−7.5 μm particles at electrode surface	Polystyrenesulfonate, polystyrene amine	up to 8.8 kV m^{-1}, 40 Hz to 10 kHz	
214	4.2 μm particles, 4−12.5 μm spacing, monolayer	PSL	0.73−1.8 V μm^{-1}	
225	2 μm particles, colloidal crystal	PSL	5 Vpp, 100 Hz to 4 kHz	Annealing colloidal crystals
231	210 and 440 nm particles, 5 mm gap, colloidal crystal	PSL	10 and 40 V cm^{-1}	Colloidal crystals
232	2.4−2.7 μm particles in 100−500 μm channel	PSL	28−33 V cm^{-1}	
233	580 nm particles, 0.6−50 μm channels, colloidal crystal	Poly(methyl methacrylate)	400 V cm^{-1}, 90 s	Colloidal crystals
234	0.6, 1.4, and 2.5 μm organic crystals in 5 μm microchannels	Tetra-*tert*-butylperylene	0−20 Vpp, 0−5 MHz, 1−2 min	Sensor, strain
235	17 nm, 130 nm, 5 μm, and 10 μm particles in 10−50 μm wells	Au	10−20 Vpp, 50−1000 Hz	

Table 6. Selected References for Capillary and Fluidic Flow Assembly

Ref	Type	Material	Parameters	Application
244	50 and 500 nm particles on Si substrate	PSL	Studies coffee rings	
246	100 nm gold and 500 nm PSL particles, templated surface	Au and PSL, PDMS	0.05−200 μm s^{-1} rate	Transfer printing
248	PDMS patterned substrate	Fungal spores	Up to 115 μm s^{-1} on patterned substrate	Immobilization of micro-organisms for liquid phase AFM
249	Nanorods in SiO$_2$ patterned substrate	Au	Evaporation from stationary substrate	Plasmonic arrays of aligned nanorods
253	320−970 nm silica particles in microchannel patterned substrate	Silica particles in etched silicon wafer channels	Evaporation from stationary substrate	Planarized photonic crystals
254	2−3 μm nanotubes in 3−9 μm wide channels	SWCNTs on Si substrate	0.1 mm s^{-1} dip coating	SWCNT circuits and devices
256	2−3 μm nanotubes in 4 μm wide channels	SWCNT on flexible parylene-C substrate	0.1 mm s^{-1} dip coating	SWCNT circuits and devices
266	77 and 83 nm particles on flexible patterned substrate, 120 nm holes	Au particles on PDMS	1 μm s^{-1} capillary slide	Plasmonic structures on flexible substrates
267	55 nm particles in hexagonal assemblies on patterned substrate, (59 nm PMMA)	Au on silica substrate	8 μm s^{-1} capillary slide	Polarized plasmonic structures
268	Rods on patterned substrate	Au rods on poly(phthalaldehyde) patterned substrate	Stationary evaporation of droplet	
271	Particles on flexible substrate	Au particles, PDMS substrate	0.5−200 μm s^{-1} capillary slide	High-resolution offset printing
419	100 nm particles on high aspect ratio (deep) patterned substrate	Ag	22−220 μm s^{-1}	Nanoscale grid electrodes
275	Core−shell particles on patterned flexible substrate	Silica/Au on PDMS	Speed not mentioned	Plasmonic clusters
277	Particles on flexible patterned substrate	PDMS substrate for microcontact printing	1 μm s^{-1} capillary slide	SERS platform
280	Aligned rods on flexible substrate for microcontact printing	Au and Ni nanowires on PDMS substrate	drying front on stationary substrate	Arrays of aligned nanorods
284	aligned rods on flexible substrate for microcontact printing	Au nanorods on PDMS substrate	0.1 μm s^{-1} capillary slide	Nanoscale circuits
285	110 × 40 nm rods in patterned substrate	Au nanorods	1−2 μm s^{-1} capillary slide	Nanoscale assembly
109	50 nm particles in 2 μm channels on flexible substrate	Ag on flexible PET	0.25−1 mm min^{-1} dip coating	Grid electrodes
319	Particles in channels	PSL	1−5 mm min^{-1} with 2.4−3.6 V bias	Particle assembly
321	Particles and tubes in 0.5−100 μm wide channels on patterned gold substrate for printing	PSL, silica, Ag, MWCNTs, SWCNTs	3−15 mm min^{-1} with 2−5 V bias	Printed components for circuits and sensors, lactate sensor
322	nanotubes on patterned substrate for printing	CNTs on gold, printed on p-type silicon	100 mm min^{-1} dip coating with applied 4 V bias	Printed source/drain electrodes for FETs
323	Nanotubes on patterned substrate for printing	SWCNTs, MWCNTs, flexible substrate	0.05 mm min^{-1} dip coating for SWCNTs,	Printed all-carbon FETs

process are discussed. A summary of the four main directed assembly techniques is listed in Table 2.

Electric field-directed assembly utilizes electric field-induced electrophoretic and DEP forces as well as electrokinetic flow to direct particle assembly. By controlling the applied electric field, the nanoparticle suspension, and the pattern geometry, scalable and high-throughput assembly of various nanomaterials is possible at single nanoparticle resolution. Many of the previous studies of nanoparticle assembly attributed to one of the three electrokinetic phenomena. However, there is a need to systematically address the influence of all the electrokinetic phenomena on the particle assembly offering a fertile field

Table 7. Selected References for Magnetophoretic Assembly

Ref	Type	Material	Parameters	Application
331	2.7 μm particles in ferrofluid	Superparamagnetic beads		Plasmonic particle rings
333	Template assisted	Fe_3O_4, $CoFe_2O_4$	200 mT	Magnetic shapes
334	12 nm articles	Fe_3O_4		Stamp for transfer printing periodic designs
335	35 nm particles	Au-coated iron oxide		Manipulation
339	5 and 10 μm particles	$MnCl_2$ ferrofluid, diamagnetic polystyrene		Particle separation
347	30 nm particles in 30−60 nm wide lines	Fe_3O_4	5 MT m^{-1} at 25 nm above surface	Particle manipulation
356	10 nm particles	Nickel mask, magnetite particles	1860 T m^{-1}	
354	20 μm magnets in array	cancer cells functionalized with magnetic particles	1−6 T^2 m^{-1}	Capture of cancer cells
360	4.69 and 2.85 μm particles in 5 μm square wells	Ni squares with superparamagnetic particles	2−3 mT	Bistable switch
241	5 μm rods and platelets in grid pattern with 50 μm pitch	Ni grid, diamagnetic silica rods, paramagnetic alumina platelets	0.44 T permanent magnet	Assembly
365	Nickel grids of 1−10 μm pitch in paramagnetic fluid	PSL, silica, bacteria	0.44 T permanent magnet	Assembly
366	4.5−8.4 μm nonmagnetic particles on polymer in ferrofluid	PSL, silica, 2 vol % Fe_3O_4 ferrofluid		Assembly
367	Superparamagnetic and nonmagnetic particles	Fe_3O_4 and ferrofluid from Fe_3O_4		Colloidal photonic array
368	Superparamagnetic particles in resin	Fe_3O_4		Colloidal photonic array
370	Nonmagnetic particles in ferrofluid	PSL in ferrofluid		Photonic array

Table 8. Selected References in Optical Assembly

Ref	Type	Material	Parameters	Application
392	Glass substrate	Au nanorods, 2−10 μm aggregates after assembly	785 nm diode laser	SERS, biosensor
405	Au thin film substrate	CdSe QDs	1064 nm Nd:YAG laser	Ring formation
407	Plasmonic gold island substrate	Semiconductor QDs patterned on plasmonic substrate (Au islands)	~1 cm s^{-1} scanning speed, ~510 nm line width	Particle assembly
409	Perfluoropentane/water biphasic mixture. Plasmonic gold island substrate	Proteins	532 nm diode laser	Low-power bubble generation for protein capture
410	Glass substrate	Au nanorods	632 nm He−Ne laser, 638 and 660 nm diode lasers	SERS, biosensor
411	Focal point in liquid	Au nanorods		SERS, biosensor
413	Glass substrate	silver nanoparticles in diethylene glycol butyl ether	532 nm diode laser, 25 mW, 1.4 μm line width at 30 μm s^{-1}	Continuous deposition of particles
414	Glass substrate	phosphotungstic acid oxometalate and perylene composite particles	1064 nm diode laser, 70−80 mW at surface	Sensor, bio, particle assembly
418	Glass substrate with oxo-metalates	oxo-metalates, dyes, carbon nanotubes, MoO_2 nanotubes	1064 nm diode laser, ~4 μm line width, up to 1 μm in thickness	particle assembly

worthy of future in-depth study. In addition, the electric field-directed assembly process requires conductive substrates to generate the electric field, which limits the choice of the substrates and applications. Studies have shown, however, that directed assembly on an insulating substrate is possible if a conductor is underneath that substrate. In addition, combining the electric field-directed assembly with a transfer printing process shows promise in resolving this challenge, and practical applications of this method in electronics and sensors fabrication are promising.

Magnetic field-directed assembly utilizes magnetophoresis to direct particle assembly. However, the particles to be assembled should be either magnetic or suspended in a magnetic medium. Moreover, because the magnetophoretic force scales with the particle volume, only micro or submicrometer-sized particles could experience sufficient magnetophoretic forces necessary for assembly. Increasing the susceptibility contrast between the particle and the suspending medium or increasing the magnetic field gradient is key to enhancing the magnetophoretic force and should be investigated further.

Optical field-directed assembly utilizes light-induced optical force and optofluidic flow to drive particle assembly. The optical force allows the manipulation of individual nanoparticles into arbitrary patterns without prepatterning of substrates. Despite the high resolution, the fabricated patterns are often composed of isolated nanoparticles, which limits the versatility of the process and the application of the fabricated structures. Furthermore, to get a high optical force, a strongly focused laser with a high power is usually required, which may lead to nanoparticle damage. Like the optical force-directed assembly, the optofluidic flow-directed assembly does not require prepatterning of substrates either. The difference is that a weakly focused laser with a low power can be employed. However, the resolution of the optofluidic flow-directed assembly is limited to micro or submicron scale. Combining the optofluidic flow with physically or chemically patterned substrates could be a potential solution.

Convective assembly, capillary assembly, and fluidic assembly utilize solvent evaporation-induced convective flow to drive the particle assembly. Although these assembly processes are highly

scalable and applicable to all kinds of nanoparticles and substrates, it often takes hours to assemble over centimeter-sized substrates due to the low rate of solvent evaporation, which poses a barrier to their practical application. However, one method known as fast fluidic assembly is much faster, taking around one second to assemble over centimeter-sized substrates. The structures fabricated using the fast fluidic assembly process are mostly in the millimeter or submillimeter scale although submicrometer scale resolution was recently achieved by a few groups. More studies are needed to increase the resolution via tuning the properties of the substrate, the nanoparticle suspension, and the velocity of withdrawal. Although high-resolution and high-throughput assembly has been demonstrated by the interfacial convective assembly process, in-depth study of the assembly mechanism and understanding of the governing parameters of the solutal Marangoni convective flow are needed to further increase the assembly efficiency.

PERSPECTIVE

Even though the directed assembly processes have their limitations, their potential applications in making electronics and sensors, such as field effect transistors, diodes, interconnects, plasmonic pixel arrays, and plasmonic sensors, have been demonstrated. These directed assembly techniques have a very promising future as an additive, scalable, and sustainable method for making electronics and sensors in the fields of medicine, optics, and energy.

One of the main advantages of directed assembly-based nanofabrication is the fact that it is based on physics and physical chemistry and does not require etching or chemical reactions and thus any nano building block can be used if it can be suspended in a liquid. Unlike conventional nanofabrication, directed assembly allows the users to utilize any material based on their properties and not based on it its compatibility with the chemical reactions used. For example, one could envision using organic and/or inorganic semiconductors, conductors, and dielectrics as well as 1D and 2D materials in the same circuit without affecting any of the materials used. This would allow researchers and entrepreneurs to use whatever material they deem necessary for their device based solely on their electrical, magnetic, optical, thermal, or mechanical properties.

The key to the success of any nanofabrication technique is scalability. A technique could be considered a viable manufacturing technique if it is high volume and high rate. For example, a technique where the directed assembly is done using a tip to guide the assembly cannot be considered a high-volume nanofabrication technique. For a technique to be successfully utilized to make electronics, it needs to be temporally and spatially scalable. This implies that an assembly process must be applied over the entire substrate (such as a silicon wafer) in a very short time span such as minutes. Several of the directed assembly approaches reviewed here meet that criterion while others do not. Table 2 addresses the scalability of each technique covered in this paper. We show that there are already hundreds of studies focused on directed assembly techniques, but more studies are needed to establish process repeatability and precise control for scalable directed assembly techniques which will be necessary to obtain high yield fabrication of nanoelectronics.

Semiconductors are essential for making electronics, and a high-performance electronic device depends on the crystallinity of the fabricated semiconductor structure. For example, a fabricated metal or dielectric structure could be used in a high-performance device even if it is not a single crystal or even crystalline. That is not the case for a semiconductor structure which needs to be at least crystalline, and to get the best performance, it needs to be a single crystal. This requires sintering of the assembled particles which is difficult since it often requires precise heating to temperatures in excess of 1100 °C. Recent research has shown that directed assembly can sinter particles in situ at room temperature and pressure to yield a single crystal metallic structure using only directed assembly and short-range forces.[317] However, more studies are needed to show how single crystal structures can be made using other materials.

Although scalable techniques have been studied and many have been used to make several devices using organic or inorganic based electronics, they have not been adopted for use in production yet, and most are still in the research and development stage. This is an issue that relies on the application or product to be made using this technology. For example, to design an electronic circuit be it a processor, memory, or even an amplifier, the designer needs to know how each material can be fabricated and which process will be used and what material properties can be obtained, and the process conditions needed to obtain such properties. This requires what the semiconductor industry calls a process design kit (PDK). The industry uses this kit to model a fabrication process for designing integrated circuits. This PDK requires a certain level of maturity which is essential to the adoption of directed assembly or any other additive manufacturing technology for making nano and microelectronics. There is a need for researchers to develop such data such that certain semiconductors, conductors, and dielectrics can be made using directed assembly processes with a predictable and repeatable outcome with or without sintering to provide a PDK that anyone could use to build devices using directed assembly.

AUTHOR INFORMATION

Corresponding Author

Ahmed A. Busnaina — *NSF Nanoscale Science and Engineering Center for High-Rate Nanomanufacturing (CHN), Northeastern University, Boston, Massachusetts 02115, United States;* orcid.org/0000-0001-8565-385X; Email: busnaina@coe.neu.edu

Authors

Zhimin Chai — *State Key Laboratory of Tribology in Advanced Equipment, Tsinghua University, Beijing 100084, China; NSF Nanoscale Science and Engineering Center for High-Rate Nanomanufacturing (CHN), Northeastern University, Boston, Massachusetts 02115, United States;* orcid.org/0000-0003-0414-1364

Anthony Childress — *NSF Nanoscale Science and Engineering Center for High-Rate Nanomanufacturing (CHN), Northeastern University, Boston, Massachusetts 02115, United States*

Complete contact information is available at:
https://pubs.acs.org/10.1021/acsnano.2c07910

ing Cluster for Smart Sensors and Materials (CSSM) at Northeastern University in Boston. The work was also supported by the start-up funding from Tsinghua University in China (grant nos. 53330600221 and 04200600121) and the funding from State Key Laboratory of Tribology, Tsinghua University in China (no. SKLT2022C15). We would like to thank Jing Wen and Zetong Li for their support in schematic image design.

VOCABULARY

nanofabrication, the approach to manufacture one-, two-, or three-dimensional functional nanostructures with at least one dimension <100 nm; top-down approach, employing physical (photons, electrons, ions, etc.) or chemical (acids, bases, etc.) means to reduce a base material to nanoscopic dimension; bottom-up approach, constructing nanoscale architectures through assembly of basic building blocks such as atoms, molecules, and nanoelements; self-assembly, spontaneously assembling disordered building blocks into ordered structures via interelement interactions driven by the minimization of free energy; directed self-assembly, employing external fields or templates to enhance interelement interactions or introduce element-template interactions in order to accomplish self-assembly of nanoelements into ordered structures; directed assembly, utilizing external fields to directly interact with nanoelements and drive the nanoelements to site-selectively assemble in predefined pattern areas on substrates to form functional structures

REFERENCES

(1) Lee, H. B. R.; Bent, S. F. Selective Toolbox for Nanofabrication. *Chem. Mater.* **2020**, *32* (8), 3323−3324.

(2) Je, J. H.; Kim, J. M.; Jaworski, J. Progression in the Fountain Pen Approach: From 2D Writing to 3D Free-Form Micro/Nanofabrication. *Small* **2017**, *13* (2), 1600137.

(3) Wang, Y.; Mirkin, C. A.; Park, S.-J. Nanofabrication beyond electronics. *ACS Nano* **2009**, *3* (5), 1049−1056.

(4) Yao, Y.; Zhang, L.; Orgiu, E.; Samorì, P. Unconventional Nanofabrication for Supramolecular Electronics. *Adv. Mater.* **2019**, *31* (23), 1900599.

(5) Bathe, M.; Chrisey, L. A.; Herr, D. J. C.; Lin, Q. H.; Rasic, D.; Woolley, A. T.; Zadegan, R. M.; Zhirnov, V. V. Roadmap on biological pathways for electronic nanofabrication and materials. *Nano Futures* **2019**, *3* (1), 012001.

(6) Stanford, M. G.; Rack, P. D.; Jariwala, D. Emerging nanofabrication and quantum confinement techniques for 2D materials beyond graphene. *npj 2D Materials and Applications* **2018**, *2*, 20.

(7) Kagan, C. R.; Lifshitz, E.; Sargent, E. H.; Talapin, D. V. Building devices from colloidal quantum dots. *Science* **2016**, *353* (6302), aac5523.

(8) Choi, J.-H.; Wang, H.; Oh, S. J.; Paik, T.; Sung, P.; Sung, J.; Ye, X.; Zhao, T.; Diroll, B. T.; Murray, C. B.; Kagan, C. R. Exploiting the colloidal nanocrystal library to construct electronic devices. *Science* **2016**, *352* (6282), 205−208.

(9) Rasappa, S.; Hulkkonen, H.; Schulte, L.; Ndoni, S.; Reuna, J.; Salminen, T.; Niemi, T. High molecular weight block copolymer lithography for nanofabrication of hard mask and photonic nanostructures. *J. Colloid Interface Sci.* **2019**, *534*, 420−429.

(10) Galeotti, F.; Pisco, M.; Cusano, A. Self-assembly on optical fibers: a powerful nanofabrication tool for next generation "lab-on-fiber" optrodes. *Nanoscale* **2018**, *10* (48), 22673−22700.

(11) Siampour, H.; Kumar, S.; Bozhevolnyi, S. I. Nanofabrication of Plasmonic Circuits Containing Single Photon Sources. *Acs Photonics* **2017**, *4* (8), 1879−1884.

(12) Furube, A.; Hashimoto, S. Insight into plasmonic hot-electron transfer and plasmon molecular drive: new dimensions in energy conversion and nanofabrication. *Npg Asia Materials* **2017**, *9*, e454.

(13) Li, L.-L.; Wu, H.-H.; Tsai, C.-H.; Wei-Guang Diau, E. Nanofabrication of uniform and stabilizer-free self-assembled platinum monolayers as counter electrodes for dye-sensitized solar cells. *NPG Asia Materials* **2014**, *6* (8), e118−e118.

(14) Ermis, M.; Antmen, E.; Hasirci, V. Micro and Nanofabrication methods to control cell-substrate interactions and cell behavior: A review from the tissue engineering perspective. *Bioactive Materials* **2018**, *3* (3), 355−369.

(15) Linklater, D. P.; Juodkazis, S.; Ivanova, E. P. Nanofabrication of mechano-bactericidal surfaces. *Nanoscale* **2017**, *9* (43), 16564−16585.

(16) Ha, D.; Hong, J.; Shin, H.; Kim, T. Unconventional micro-/nanofabrication technologies for hybrid-scale lab-on-a-chip. *Lab Chip* **2016**, *16* (22), 4296−4312.

(17) Jiang, T.; Deng, M.; James, R.; Nair, L. S.; Laurencin, C. T. Micro- and nanofabrication of chitosan structures for regenerative engineering. *Acta Biomaterialia* **2014**, *10* (4), 1632−1645.

(18) Kim, B. C.; Moraes, C.; Huang, J. X.; Thouless, M. D.; Takayama, S. Fracture-based micro- and nanofabrication for biological applications. *Biomaterials Science* **2014**, *2* (3), 288−296.

(19) Fine, D.; Grattoni, A.; Goodall, R.; Bansal, S. S.; Chiappini, C.; Hosali, S.; van de Ven, A. L.; Srinivasan, S.; Liu, X. W.; Godin, B.; Brousseau, L.; Yazdi, I. K.; Fernandez-Moure, J.; Tasciotti, E.; Wu, H. J.; Hu, Y.; Klemm, S.; Ferrari, M. Silicon Micro- and Nanofabrication for Medicine. *Adv. Healthcare Mater.* **2013**, *2* (5), 632−666.

(20) Hol, F. J. H.; Dekker, C. Zooming in to see the bigger picture: Microfluidic and nanofabrication tools to study bacteria. *Science* **2014**, *346* (6208), 438.

(21) Mallapragada, S. K.; Brenza, T. M.; McMillan, J. M.; Narasimhan, B.; Sakaguchi, D. S.; Sharma, A. D.; Zbarska, S.; Gendelman, H. E. Enabling nanomaterial, nanofabrication and cellular technologies for nanoneuromedicines. *Nanomedicine-Nanotechnology Biology and Medicine* **2015**, *11* (3), 715−729.

(22) Qi, S.; Craig, D. Recent developments in micro-and nanofabrication techniques for the preparation of amorphous pharmaceutical dosage forms. *Adv. Drug Delivery Rev.* **2016**, *100*, 67−84.

(23) Mijatovic, D.; Eijkel, J. C. T.; Van Den Berg, A. Technologies for nanofluidic systems: top-down vs. bottom-up —a review. *Lab Chip* **2005**, *5* (5), 492−500.

(24) Yu, H.-d.; Regulacio, M. D.; Ye, E.; Han, M.-y. Chemical routes to top-down nanofabrication. *Chem. Soc. Rev.* **2013**, *42* (14), 6006−6018.

(25) Biswas, A.; Bayer, I. S.; Biris, A. S.; Wang, T.; Dervishi, E.; Faupel, F. Advances in top-down and bottom-up surface nanofabrication: Techniques, applications & future prospects. *Adv. Colloid Interface Sci.* **2012**, *170* (1−2), 2−27.

(26) Sekkat, Z.; Kawata, S. Laser nanofabrication in photoresists and azopolymers. *Laser & Photonics Reviews* **2014**, *8* (1), 1−26.

(27) Jiang, L.; Wang, A. D.; Li, B.; Cui, T. H.; Lu, Y. F. Electrons dynamics control by shaping femtosecond laser pulses in micro/nanofabrication: modeling, method, measurement and application. *Light-Science & Applications* **2018**, *7*, 17134.

(28) Jesse, S.; Borisevich, A. Y.; Fowlkes, J. D.; Lupini, A. R.; Rack, P. D.; Unocic, R. R.; Sumpter, B. G.; Kalinin, S. V.; Belianinov, A.; Ovchinnikova, O. S. Directing Matter: Toward Atomic-Scale 3D Nanofabrication. *ACS Nano* **2016**, *10* (6), 5600−5618.

(29) Baglin, J. E. E. Ion beam nanoscale fabrication and lithography—A review. *Appl. Surf. Sci.* **2012**, *258* (9), 4103−4111.

(30) Cai, J.; Zhu, Z.; Alkemade, P. F. A.; Van Veldhoven, E.; Wang, Q.; Ge, H.; Rodrigues, S. P.; Cai, W.; Li, W. D. 3D Volumetric Energy Deposition of Focused Helium Ion Beam Lithography: Visualization, Modeling, and Applications in Nanofabrication. *Advanced Materials Interfaces* **2018**, *5* (12), 1800203.

(31) Waldrop, M. M. The chips are down for Moore's law. *Nature* **2016**, *530* (7589), 144.

(32) Eeckhout, L. Is Moore's Law Slowing Down? What's Next? *IEEE Micro* **2017**, *37* (4), 4−5.

(33) Schor, D. *TSMC Starts 5-Nanometer Risk Production*. https://fuse.wikichip.org/news/2207/tsmc-starts-5-nanometer-risk-production/ (accessed 18 Oct 2022).

(34) Platzer, M. D.; Sargent, J. F., Jr. *U.S. Semiconductor Manufacturing: Industry Trends, Global Competition, Federal Policy*; Congressional Research Service: Washington, DC, 2016.

(35) Zhao, C.; Shah, P. J.; Bissell, L. J. Laser additive nano-manufacturing under ambient conditions. *Nanoscale* **2019**, *11* (35), 16187−16199.

(36) Ozin, G. A.; Hou, K.; Lotsch, B. V.; Cademartiri, L.; Puzzo, D. P.; Scotognella, F.; Ghadimi, A.; Thomson, J. Nanofabrication by self-assembly. *Mater. Today* **2009**, *12* (5), 12−23.

(37) Service, R. F. How far can we push chemical self-assembly? *Science* **2005**, *309* (5731), 95.

(38) Zhang, J.; Li, Y.; Zhang, X.; Yang, B. Colloidal self-assembly meets nanofabrication: from two-dimensional colloidal crystals to nanostructure arrays. *Advanced materials (Deerfield Beach, Fla.)* **2010**, *22* (38), 4249.

(39) Liddle, J. A.; Gallatin, G. M. Nanomanufacturing: A Perspective. *ACS Nano* **2016**, *10* (3), 2995.

(40) Tang, L.; Li, T.; Luo, Y. T.; Feng, S. M.; Cai, Z. Y.; Zhang, H.; Liu, B. L.; Cheng, H. M. Vertical Chemical Vapor Deposition Growth of Highly Uniform 2D Transition Metal Dichalcogenides. *ACS Nano* **2020**, *14* (4), 4646−4653.

(41) Nowakowska, S.; Wäckerlin, A.; Kawai, S.; Ivas, T.; Nowakowski, J.; Fatayer, S.; Wäckerlin, C.; Nijs, T.; Meyer, E.; Björk, J.; Stöhr, M.; Gade, L. H.; Jung, T. A. Interplay of weak interactions in the atom-by-atom condensation of xenon within quantum boxes. *Nat. Commun.* **2015**, *6* (1), 6071.

(42) Zhao, Y.; Dai, X. P.; Wang, F.; Zhang, X. L.; Fan, C. H.; Liu, X. G. Nanofabrication based on DNA nanotechnology. *Nano Today* **2019**, *26*, 123−148.

(43) Yang, G. G.; Choi, J.; Cha, S. K.; Lee, G. Y.; Jin, H. M.; Hwang, H. S.; Yun, T.; Kang, J.; Han, K. H.; Kim, J. H.; Choi, H. J.; Im, S. G.; Kim, S. O. Conformal 3D Nanopatterning by Block Copolymer Lithography with Vapor-Phase Deposited Neutral Adlayer. *ACS Nano* **2019**, *13* (11), 13092−13099.

(44) Zhou, H. J.; Yang, G. W.; Zhang, Y. Y.; Xu, Z. K.; Wu, G. P. Bioinspired Block Copolymer for Mineralized Nanoporous Membrane. *ACS Nano* **2018**, *12* (11), 11471−11480.

(45) Morphew, D.; Shaw, J.; Avins, C.; Chakrabarti, D. Programming Hierarchical Self-Assembly of Patchy Particles into Colloidal Crystals via Colloidal Molecules. *ACS Nano* **2018**, *12* (3), 2355−2364.

(46) Whitesides, G. M.; Grzybowski, B. Self-assembly at all scales. *Science* **2002**, *295* (5564), 2418−2421.

(47) Bishop, K. J. M.; Wilmer, C. E.; Soh, S.; Grzybowski, B. A. Nanoscale Forces and Their Uses in Self-Assembly. *Small* **2009**, *5* (14), 1600−1630.

(48) Min, Y.; Akbulut, M.; Kristiansen, K.; Golan, Y.; Israelachvili, J. The role of interparticle and external forces in nanoparticle assembly. *Nat. Mater.* **2008**, *7* (7), 527.

(49) Xu, L. G.; Ma, W.; Wang, L. B.; Xu, C. L.; Kuang, H.; Kotov, N. A. Nanoparticle assemblies: dimensional transformation of nanomaterials and scalability. *Chem. Soc. Rev.* **2013**, *42* (7), 3114−3126.

(50) Jacobs, W. M.; Frenkel, D. Self-assembly protocol design for periodic multicomponent structures. *Soft Matter* **2015**, *11* (46), 8930−8938.

(51) Chin, G. Stabilized self-assembly. *Science* **2002**, *295* (5555), 587.

(52) van Dommelen, R.; Fanzio, P.; Sasso, L. Surface self-assembly of colloidal crystals for micro- and nano-patterning. *Adv. Colloid Interface Sci.* **2018**, *251*, 97−114.

(53) Zhang, S.-y.; Regulacio, M. D.; Han, M.-y. Self-assembly of colloidal one-dimensional nanocrystals. *Chem. Soc. Rev.* **2014**, *43* (7), 2301−2323.

(54) Bigioni, T. P.; Lin, X.-M.; Nguyen, T. T.; Corwin, E. I.; Witten, T. A.; Jaeger, H. M. Kinetically driven self assembly of highly ordered nanoparticle monolayers. *Nat. Mater.* **2006**, *5* (4), 265.

(55) Sainato, M.; Shevitski, B.; Sahu, A.; Forster, J. D.; Aloni, S.; Barillaro, G.; Urban, J. J. Long-Range Order in Nanocrystal Assemblies Determines Charge Transport of Films. *ACS omega* **2017**, *2* (7), 3681−3690.

(56) Lin, X. M.; Jaeger, H. M.; Sorensen, C. M.; Klabunde, K. J. Formation of long-range-ordered nanocrystal superlattices on silicon nitride substrates. *J. Phys. Chem. B* **2001**, *105* (17), 3353.

(57) Aubry, N.; Singh, P.; Janjua, M.; Nudurupati, S. Micro- and nanoparticles self-assembly for virtually defect-free, adjustable monolayers. *Proc. Natl. Acad. Sci. U.S.A.* **2008**, *105* (10), 3711.

(58) Ji, S. X.; Wan, L.; Liu, C. C.; Nealey, P. F. Directed self-assembly of block copolymers on chemical patterns: A platform for nano-fabrication. *Prog. Polym. Sci.* **2016**, *54−55*, 76−127.

(59) Chen, X. X.; Zhou, C.; Chen, S. J.; Craig, G. S. W.; Rincon-Delgadillo, P.; Dazai, T.; Miyagi, K.; Maehashi, T.; Yamazaki, A.; Gronheid, R.; Stoykovich, M. P.; Nealey, P. F. Ionic Liquids as Additives to Polystyrene-Block-Poly(Methyl Methacrylate) Enabling Directed Self-Assembly of Patterns with Sub-10 nm Features. *ACS Appl. Mater. Interfaces* **2018**, *10* (19), 16747−16759.

(60) Darling, S. B. Directing the self-assembly of block copolymers. *Prog. Polym. Sci.* **2007**, *32* (10), 1152−1204.

(61) Kim, H.-C.; Park, S.-M.; Hinsberg, W. D. Block copolymer based nanostructures: materials, processes, and applications to electronics. (Report). *Chem. Rev.* **2010**, *110* (1), 146−177.

(62) Chai, J.; Wang, D.; Fan, X.; Buriak, J. Assembly of aligned linear metallic patterns on silicon. *Nat. Nanotechnol.* **2007**, *2* (8), 500−6.

(63) Park, M.; Harrison, C.; Chaikin, P. M.; Register, R. A.; Adamson, D. H. Block copolymer lithography: periodic arrays of about 10 to the 11th power holes in 1 square centimeter. *Science* **1997**, *276* (5317), 1401.

(64) Dumanli, A. G.; Savin, T. Recent advances in the biomimicry of structural colours. *Chem. Soc. Rev.* **2016**, *45* (24), 6698−6724.

(65) Wang, B.; Zhang, Y.; Guo, Z.; Zhang, L. Self-assembly of nanoparticles: Static and dynamic. *Mater. Today* **2019**, *25*, 112−113.

(66) Grzelczak, M.; Vermant, J.; Furst, E. M.; Liz-Marzan, L. M. Directed Self-Assembly of Nanoparticles. *ACS Nano* **2010**, *4* (7), 3591−3605.

(67) Zhihong, N.; Alla, P.; Eugenia, K. Properties and emerging applications of self-assembled structures made from inorganic nanoparticles. *Nat. Nanotechnol.* **2009**, *5* (1), 15.

(68) Azari, A.; Crassous, J. J.; Mihut, A. M.; Bialik, E.; Schurtenberger, P.; Stenhammar, J.; Linse, P. Directed Self-Assembly of Polarizable Ellipsoids in an External Electric Field. *Langmuir* **2017**, *33* (48), 13834−13840.

(69) Nojd, S.; Mohanty, P. S.; Bagheri, P.; Yethiraj, A.; Schurtenberger, P. Electric field driven self-assembly of ionic microgels. *Soft Matter* **2013**, *9* (38), 9199−9207.

(70) Crassous, J.; Mihut, A.; Wernersson, E.; Pfleiderer, P.; Vermant, J.; Linse, P.; Schurtenberger, P. Field-induced assembly of colloidal ellipsoids into well-defined microtubules. *Nat. Commun.* **2014**, *5* (1), 5516.

(71) Martchenko, I.; Crassous, J. J.; Mihut, A. M.; Bialik, E.; Hirt, A. M.; Rufier, C.; Menzel, A.; Dietsch, H.; Linse, P.; Schurtenberger, P. Anisotropic magnetic particles in a magnetic field. *Soft Matter* **2016**, *12* (42), 8755−8767.

(72) Swan, J. W.; Bauer, J. L.; Liu, Y.; Furst, E. M. Directed colloidal self-assembly in toggled magnetic fields. *Soft Matter* **2014**, *10* (8), 1102−1109.

(73) Butter, K.; Bomans, P. H. H.; Frederik, P. M.; Vroege, G. J.; Philipse, A. P. Direct observation of dipolar chains in iron ferrofluids by cryogenic electron microscopy. *Nat. Mater.* **2003**, *2* (2), 88−91.

(74) Chavez, B. L.; Sosnowski, K. C.; Bauer, M. J.; Budi, M. A. K.; Andrew, J. S.; Crawford, T. M. Toward nanoscale multiferroic devices: Magnetic field-directed self-assembly and chaining in Janus nanofibers. *AIP Adv.* **2018**, *8* (5), 056808.

(75) Hughes, R. A.; Menumerov, E.; Neretina, S. When lithography meets self-assembly: a review of recent advances in the directed assembly of complex metal nanostructures on planar and textured surfaces. *Nanotechnology* **2017**, *28* (28), 282002.

(76) Grzybowski, B. A.; Wilmer, C. E.; Kim, J.; Browne, K. P.; Bishop, K. J. M. Self-assembly: from crystals to cells. *Soft Matter* **2009**, 5 (6), 1110−1128.

(77) Zhang, S. J.; Pelligra, C. I.; Feng, X. D.; Osuji, C. O. Directed Assembly of Hybrid Nanomaterials and Nanocomposites. *Adv. Mater.* **2018**, 30 (18), 1705794.

(78) Kruglova, O.; Demeyer, P.-J.; Zhong, K.; Zhou, Y.; Clays, K. Wonders of colloidal assembly. *Soft Matter* **2013**, 9 (38), 9072−9087.

(79) Kumar, S.; Seo, Y. K.; Kim, G. H. Manipulation and trapping of semiconducting ZnO nanoparticles into nanogap electrodes by dielectrophoresis technique. *Appl. Phys. Lett.* **2009**, 94 (15), 153104.

(80) Jung, S. H.; Chen, C.; Cha, S. H.; Yeom, B.; Bahng, J. H.; Srivastava, S.; Zhu, J.; Yang, M.; Liu, S. Q.; Kotov, N. A. Spontaneous Self-Organization Enables Dielectrophoresis of Small Nanoparticles and Formation of Photoconductive Microbridges. *J. Am. Chem. Soc.* **2011**, 133 (28), 10688−10691.

(81) Huy, B. L.; Kumar, S.; Kim, G. H. Manipulation of palladium nanoparticles in a 20 nm gap between electrodes for hydrogen sensor application. *J. Phys. D: Appl. Phys.* **2011**, 44 (32), 325402.

(82) Xiong, X. G.; Busnaina, A. Direct assembly of nanoparticles for large-scale fabrication of nanodevices and structures. *J. Nanopart. Res.* **2008**, 10 (6), 947−954.

(83) Xiong, X.; Busnaina, A.; Selvarasah, S.; Somu, S.; Wei, M.; Mead, J.; Chen, C.-L.; Aceros, J.; Makaram, P.; Dokmeci, M. R. Directed assembly of gold nanoparticle nanowires and networks for nanodevices. *Appl. Phys. Lett.* **2007**, 91 (6), 063101.

(84) Khanduja, N.; Selvarasah, S.; Chen, C.-L.; Dokmeci, M. R.; Xiong, X.; Makaram, P.; Busnaina, A. Three dimensional controlled assembly of gold nanoparticles using a micromachined platform. *Applied physics letters* **2007**, 90 (8), 083105.

(85) Ozturk, B.; Blackledge, C.; Flanders, B. N.; Grischkowsky, D. R. Reproducible interconnects assembled from gold nanorods. *Appl. Phys. Lett.* **2006**, 88 (7), 073108.

(86) Wang, J.; Rathi, S.; Singh, B.; Lee, I.; Joh, H.-I.; Kim, G.-H. Alternating Current Dielectrophoresis Optimization of Pt-Decorated Graphene Oxide Nanostructures for Proficient Hydrogen Gas Sensor. *ACS Applied Materials Interfaces* **2015**, 7 (25), 13768−13775.

(87) Leiterer, C.; Berg, S.; Eskelinen, A. P.; Csaki, A.; Urban, M.; Torma, P.; Fritzsche, W. Assembling gold nanoparticle chains using an AC electrical field: Electrical detection of organic thiols. *Sens. Actuators, B* **2013**, 176, 368−373.

(88) Sire, C. d.; Ardiaca, F.; Lepilliet, S.; Seo, J.-W. T.; Hersam, M. C.; Dambrine, G.; Happy, H.; Derycke, V. Flexible Gigahertz Transistors Derived from Solution-Based Single-Layer Graphene. *Nano Lett.* **2012**, 12 (3), 1184−1188.

(89) Liberman, V.; Yilmaz, C.; Bloomstein, T. M.; Somu, S.; Echegoyen, Y.; Busnaina, A.; Cann, S. G.; Krohn, K. E.; Marchant, M. F.; Rothschild, M. A Nanoparticle Convective Directed Assembly Process for the Fabrication of Periodic Surface Enhanced Raman Spectroscopy Substrates. *Adv. Mater.* **2010**, 22 (38), 4298−4302.

(90) He, X. B.; Tang, J. B.; Hu, H. T.; Shi, J. J.; Guan, Z. Q.; Zhang, S. P.; Xu, H. X. Electrically Driven Optical Antennas Based on Template Dielectrophoretic Trapping. *ACS Nano* **2019**, 13 (12), 14041−14047.

(91) Stelson, A. C.; Penterman, S. J.; Watson, C. M. L. Electric field-directed assembly of fullerene crystal rods into hierarchical films. *J. Mater. Chem. C* **2018**, 6 (41), 11118−11127.

(92) Stelson, A. C.; Penterman, S. J.; Watson, C. M. L. Hierarchical Fullerene Assembly: Seeded Coprecipitation and Electric Field Directed Assembly. *Small* **2017**, 13 (17), 1603509.

(93) Gong, J. J.; Wu, N. Electric-Field Assisted Assembly of Colloidal Particles into Ordered Nonclose-Packed Arrays. *Langmuir* **2017**, 33 (23), 5769−5776.

(94) Crassous, J. J.; Demirors, A. F. Multiscale directed self-assembly of composite microgels in complex electric fields. *Soft Matter* **2017**, 13 (1), 88−100.

(95) Shah, N.; Zamborini, F. P. Surfactant-Assisted Voltage-Driven Silver Nanoparticle Chain Formation across Microelectrode Gaps in Air. *ACS Nano* **2015**, 9 (10), 10278−10286.

(96) Ma, F. D.; Wang, S. J.; Smith, L.; Wu, N. Two-Dimensional Assembly of Symmetric Colloidal Dimers under Electric Fields. *Adv. Funct. Mater.* **2012**, 22 (20), 4334−4343.

(97) Vijayaraghavan, A.; Sciascia, C.; Dehm, S.; Lombardo, A.; Bonetti, A.; Ferrari, A. C.; Krupke, R. Dielectrophoretic Assembly of High-Density Arrays of Individual Graphene Devices for Rapid Screening. *ACS Nano* **2009**, 3 (7), 1729−1734.

(98) Xie, Q. G.; Davies, G. B.; Harting, J. Direct Assembly of Magnetic Janus Particles at a Droplet Interface. *ACS Nano* **2017**, 11 (11), 11232−11239.

(99) Lee, J. G.; Porter, V.; Shelton, W. A.; Bharti, B. Magnetic Field-Driven Convection for Directed Surface Patterning of Colloids. *Langmuir* **2018**, 34 (50), 15416−15424.

(100) Hu, D. D.; Zheng, K. J.; Yang, F.; Nie, J.; Zhu, X. Q. Flexible electronics based on magnetic printing and the volume additive principle. *J. Mater. Chem. C* **2017**, 5 (32), 8052−8058.

(101) Tierno, P. Magnetic Assembly and Annealing of Colloidal Lattices and Superlattices. *Langmuir* **2014**, 30 (26), 7670−7675.

(102) Ye, M.; Wei, Z. W.; Hu, F.; Wang, J. X.; Ge, G. L.; Hu, Z. Y.; Shao, M. W.; Lee, S. T.; Liu, J. Fast assembling microarrays of superparamagnetic Fe3O4@Au nanoparticle clusters as reproducible substrates for surface-enhanced Raman scattering. *Nanoscale* **2015**, 7 (32), 13427−13437.

(103) Singamaneni, S.; Bliznyuk, V. N.; Binek, C.; Tsymbal, E. Y. Magnetic nanoparticles: recent advances in synthesis, self-assembly and applications. *J. Mater. Chem.* **2011**, 21 (42), 16819−16845.

(104) Erb, R. M.; Son, H. S.; Samanta, B.; Rotello, V. M.; Yellen, B. B. Magnetic assembly of colloidal superstructures with multipole symmetry. *Nature* **2009**, 457 (7232), 999−1002.

(105) Baudry, J.; Chaikin, P.; Bibette, J.; Zerrouki, D.; Pine, D. Chiral colloidal clusters. *Nature* **2008**, 455 (7211), 380−382.

(106) Coursault, D.; Sule, N.; Parker, J.; Bao, Y.; Scherer, N. F. Dynamics of the Optically Directed Assembly and Disassembly of Gold Nanoplatelet Arrays. *Nano Lett.* **2018**, 18 (6), 3391−3399.

(107) Dinh, N. D.; Luo, R. C.; Christine, M. T. A.; Lin, W. N.; Shih, W. C.; Goh, J. C. H.; Chen, C. H. Effective Light Directed Assembly of Building Blocks with Microscale Control. *Small* **2017**, 13 (24), 1700684.

(108) Lin, L.; Peng, X.; Wang, M.; Scarabelli, L.; Mao, Z.; Liz-Marzán, L. M.; Becker, M. F.; Zheng, Y. Light-Directed Reversible Assembly of Plasmonic Nanoparticles Using Plasmon-Enhanced Thermophoresis. *ACS Nano* **2016**, 10 (10), 9659−9668.

(109) Abbasi, S. A.; Chai, Z. M.; Busnaina, A. Scalable Printing of High-Resolution Flexible Transparent Grid Electrodes Using Directed Assembly of Silver Nanoparticles. *Advanced Materials Interfaces* **2019**, 6 (21), 1900898.

(110) Chai, Z.; Abbasi, S. A.; Busnaina, A. A. Scalable Directed Assembly of Highly Crystalline 2,7-Dioctyl[1]benzothieno[3,2- b][1]benzothiophene (C8-BTBT) Films. *ACS Appl. Mater. Interfaces* **2018**, 10 (21), 18123−18130.

(111) Chai, Z. M.; Abbasi, S. A.; Busnaina, A. A. Solution-processed organic field-effect transistors using directed assembled carbon nanotubes and 2,7-dioctyl 1 benzothieno 3,2-b 1 benzothiophene (C8-BTBT). *Nanotechnology* **2019**, 30 (48), 485203.

(112) Cha, N.; Echegoyen, Y.; Kim, T.; Park, J.; Busnaina, A. A. Convective Assembly and Dry Transfer of Nanoparticles Using Hydrophobic/Hydrophilic Monolayer Templates. *Langmuir* **2009**, 25 (19), 11375−11382.

(113) Kalinina, E. G.; Pikalova, E. Y. New trends in the development of electrophoretic deposition method in the solid oxide fuel cell technology: theoretical approaches, experimental solutions and development prospects. *Russ. Chem. Rev.* **2019**, 88 (12), 1179−1219.

(114) Austin, J.; Fernandes, D.; Ruszala, M. J. A.; Hill, N.; Corbett, J. Routine, ensemble characterisation of electrophoretic mobility in high and saturated ionic dispersions. *Sci. Rep.* **2020**, 10 (1), 4628.

(115) Besra, L.; Liu, M. A review on fundamentals and applications of electrophoretic deposition (EPD). *Prog. Mater. Sci.* **2007**, 52 (1), 1−61.

(116) Ferrari, B.; Moreno, R. EPD kinetics: A review. *Journal of the European Ceramic Society* **2010**, 30 (5), 1069−1078.

(117) Dörner, L.; Schmutz, P.; Kaegi, R.; Kovalenko, M. V.; Jeurgens, L. P. H. Electrophoretic deposition of nanoporous oxide coatings from concentrated CuO nanoparticle dispersions. *Langmuir* **2020**, *36*, 8075.

(118) Wu, K.; Zhitomirsky, I. Electrophoretic Deposition of Ceramic Nanoparticles. *International Journal of Applied Ceramic Technology* **2011**, *8* (4), 920−927.

(119) Ji, C. Z.; Lan, W. H.; Xiao, P. Fabrication of yttria-stabilized zirconia coatings using electrophoretic deposition: Packing mechanism during deposition. *J. Am. Ceram. Soc.* **2008**, *91* (4), 1102−1109.

(120) Shah, A. A.; Ganesan, M.; Jocz, J.; Solomon, M. J. Direct current electric field assembly of colloidal crystals displaying reversible structural color. *ACS Nano* **2014**, *8* (8), 8095−8103.

(121) Yilmaz, C.; Cetin, A. E.; Goutzamanidis, G.; Huang, J.; Somu, S.; Altug, H.; Wei, D. G.; Busnaina, A. Three-Dimensional Crystalline and Homogeneous Metallic Nanostructures Using Directed Assembly of Nanoparticles. *ACS Nano* **2014**, *8* (5), 4547−4558.

(122) Yilmaz, C.; Sirman, A.; Halder, A.; Busnaina, A. High-Rate Assembly of Nanomaterials on Insulating Surfaces Using Electro-Fluidic Directed Assembly. *ACS Nano* **2017**, *11*, 7679−7689.

(123) Singh, A.; English, N. J.; Ryan, K. M. Highly ordered nanorod assemblies extending over device scale areas and in controlled multilayers by electrophoretic deposition.(Report). *J. Phys. Chem. B* **2013**, *117* (6), 1608−1615.

(124) Song, K. W.; Costi, R.; Bulović, V. Electrophoretic Deposition of CdSe/ZnS Quantum Dots for Light-Emitting Devices. *Adv. Mater.* **2013**, *25* (10), 1420−1423.

(125) Santhanagopalan, S.; Balram, A.; Meng, D. D. Scalable High-Power Redox Capacitors with Aligned Nanoforests of Crystalline MnO2 Nanorods by High Voltage Electrophoretic Deposition. *ACS Nano* **2013**, *7* (3), 2114−2125.

(126) Salant, A.; Shalom, M.; Hod, I.; Faust, A.; Zaban, A.; Banin, U. Quantum Dot Sensitized Solar Cells with Improved Efficiency Prepared Using Electrophoretic Deposition. *ACS Nano* **2010**, *4* (10), 5962−5968.

(127) Marin-Suarez, M.; Medina-Rodriguez, S.; Ergeneman, O.; Pane, S.; Fernandez-Sanchez, J. F.; Nelson, B. J.; Fernandez-Gutierrez, A. Electrophoretic deposition as a new approach to produce optical sensing films adaptable to microdevices. *Nanoscale* **2014**, *6* (1), 263−271.

(128) Lommens, P.; Van Thourhout, D.; Smet, P. F.; Poelman, D.; Hens, Z. Electrophoretic deposition of zno nanoparticles, from micropatterns to substrate coverage. *Nanotechnology* **2008**, *19* (24), 245301.

(129) Xiong, X. G.; Makaram, P.; Busnaina, A.; Bakhtari, K.; Somu, S.; McGruer, N.; Park, J. Large scale directed assembly of nanoparticles using nanotrench templates. *Appl. Phys. Lett.* **2006**, *89* (19), 193108.

(130) Zhang, H.; Cadusch, J.; Kinnear, C.; James, T.; Roberts, A.; Mulvaney, P. Direct Assembly of Large Area Nanoparticle Arrays. *ACS Nano* **2018**, *12* (8), 7529−7537.

(131) Siavoshi, S.; Yilmaz, C.; Somu, S.; Musacchio, T.; Upponi, J. R.; Torchilin, V. P.; Busnaina, A. Size-Selective Template-Assisted Electrophoretic Assembly of Nanoparticles for Biosensing Applications. *Langmuir* **2011**, *27* (11), 7301−7306.

(132) Adams, S. M.; Campione, S.; Capolino, F.; Ragan, R. Directing cluster formation of Au nanoparticles from colloidal solution. *Langmuir* **2013**, *29* (13), 4242−4251.

(133) Qian, F.; Pascall, A. J.; Bora, M.; Han, T. Y. J.; Guo, S. R.; Ly, S. S.; Worsley, M. A.; Kuntz, J. D.; Olson, T. Y. On-Demand and Location Selective Particle Assembly via Electrophoretic Deposition for Fabricating Structures with Particle-to-Particle Precision. *Langmuir* **2015**, *31* (12), 3563−3568.

(134) Doane, T. L.; Chuang, C. H.; Hill, R. J.; Burda, C. Nanoparticle zeta-Potentials. *Acc. Chem. Res.* **2012**, *45* (3), 317−326.

(135) Yilmaz, C.Precise Directed Assembly of Nanoparticles for Electronic, Optical, and Biomedical Applications. *Ph.D. Thesis*, Northeastern University, Boston, MA, 2013.

(136) Verde, M.; Peiteado, M.; Caballero, A. C.; Villegas, M.; Ferrari, B. Electrophoretic Deposition of Transparent ZnO Thin Films from Highly Stabilized Colloidal Suspensions. *J. Colloid Interface Sci.* **2012**, *373* (1), 27−33.

(137) Oćwieja, M.; Maciejewska-Prończuk, J.; Adamczyk, Z.; Roman, M. Formation of positively charged gold nanoparticle monolayers on silica sensors. *J. Colloid Interface Sci.* **2017**, *501*, 192−201.

(138) Morga, M.; Adamczyk, Z.; Kosior, D. Silica nanoparticle monolayers on a macroion modified surface: formation mechanism and stability. *Phys. Chem. Chem. Phys.* **2017**, *19* (34), 22721−22732.

(139) Bizmark, N.; Ioannidis, M. A. Effects of Ionic Strength on the Colloidal Stability and Interfacial Assembly of Hydrophobic Ethyl Cellulose Nanoparticles. *Langmuir* **2015**, *31* (34), 9282−9289.

(140) Barbee, K. D.; Hsiao, A. P.; Heller, M. J.; Huang, X. Electric field directed assembly of high-density microbead arrays. *Lab Chip* **2009**, *9* (22), 3268.

(141) Tiwari, P.; Ferson, N. D.; Andrew, J. S. Elucidating the role of electrophoretic mobility for increasing yield in the electrophoretic deposition of nanomaterials. *J. Colloid Interface Sci.* **2020**, *570*, 109−115.

(142) Hu, S. S.; Finklea, H.; Li, W. Y.; Li, W.; Qi, H.; Zhang, N.; Liu, X. B. Alternating Current Electrophoretic Deposition of Gadolinium Doped Ceria onto Yttrium Stabilized Zirconia: A Study of the Mechanism. *ACS Appl. Mater. Interfaces* **2020**, *12* (9), 11126−11134.

(143) Chavez-Valdez, A.; Boccaccini, A. R. Innovations in electrophoretic deposition: Alternating current and pulsed direct current methods. *Electrochim. Acta* **2012**, *65*, 70−89.

(144) Neirinck, B.; Van der Biest, O.; Vleugels, J. A Current Opinion on Electrophoretic Deposition in Pulsed and Alternating Fields. *J. Phys. Chem. B* **2013**, *117* (6), 1516−1526.

(145) Morgan, H.; Green, N. G.Introduction and Overview. *AC Electrokinetics: Colloids and Nanoparticles*, 1st ed.; Research Studies Press: Baldock, England, 2003; pp 1−14.

(146) Velev, O. D.; Bhatt, K. H. On-chip micromanipulation and assembly of colloidal particles by electric fields. *Soft Matter* **2006**, *2* (9), 738−750.

(147) Zhao, H. Double-layer polarization of a nonconducting particle in an alternating current field with applications to dielectrophoresis. *Electrophoresis* **2011**, *32*, 2232−2244.

(148) Che-Kai, Y.; Jia-Yang, J. Dimensional analysis and prediction of dielectrophoretic crossover frequency of spherical particles. *AIP Adv.* **2017**, *7* (6), 065304.

(149) Ermolina, I.; Morgan, H. The electrokinetic properties of latex particles: comparison of electrophoresis and dielectrophoresis. *J. Colloid Interface Sci.* **2005**, *285* (1), 419−428.

(150) Green, N. G.; Morgan, H. Dielectrophoresis of submicrometer latex spheres. 1. Experimental results. *J. Phys. Chem. B* **1999**, *103* (1), 41−50.

(151) Green, N. G.; Morgan, H. Dielectrophoretic separation of nanoparticles. *J. Phys. D: Appl. Phys.* **1997**, *30* (11), L41−L44.

(152) Hughes, M. P.; Morgan, H. Dielectrophoretic characterization and separation of antibody-coated submicrometer latex spheres. *Anal. Chem.* **1999**, *71* (16), 3441−3445.

(153) Hughes, M. P.; Morgan, H.; Flynn, M. F. The Dielectrophoretic Behavior of Submicron Latex Spheres: Influence of Surface Conductance. *J. Colloid Interface Sci.* **1999**, *220* (2), 454−457.

(154) Jones, T. B.Dielectrophoresis and magnetophoresis. *Electromechanics of Particles*, 1st ed.; Cambridge University Press: Cambridge, 1995; pp 34−82.

(155) Chen, D. F.; Du, H. Simulation studies on electrothermal fluid flow induced in a dielectrophoretic microelectrode system. *Journal of Micromechanics and Microengineering* **2006**, *16* (11), 2411−2419.

(156) Loire, S.; Kauffmann, P.; Mezić, I.; Meinhart, C. D. A theoretical and experimental study of ac electrothermal flows. *J. Phys. D: Appl. Phys.* **2012**, *45* (18), 185301.

(157) Adams, T. N. G.; Leonard, K. M.; Minerick, A. R. Frequency sweep rate dependence on the dielectrophoretic response of polystyrene beads and red blood cells. *Biomicrofluidics* **2013**, *7* (6), 064114.

(158) Pethig, R. Review Article—Dielectrophoresis: Status of the theory, technology, and applications. *Biomicrofluidics* **2010**, *4* (2), 022811.

(159) Grosse, C.; Delgado, A. V. Dielectric dispersion in aqueous colloidal systems. *Current opinion in colloid & interface science* **2010**, *15* (3), 145−159.

(160) Bernard, L.; Calame, M.; van der Molen, S. J.; Liao, J.; Schönenberger, C. Controlled formation of metallic nanowires via au nanoparticle ac trapping. *Nanotechnology* **2007**, *18* (23), 235202.

(161) Cheon, D.; Kumar, S.; Kim, G. H. Assembly of gold nanoparticles of different diameters between nanogap electrodes. *Appl. Phys. Lett.* **2010**, *96* (1), 013101.

(162) Yuan, Y. J.; Andrews, M. K.; Marlow, B. K. Chaining and dendrite formation of gold particles. *Appl. Phys. Lett.* **2004**, *85* (1), 130−132.

(163) Ding, H. T.; Liu, W. Y.; Ding, Y. C.; Shao, J. Y.; Zhang, L. L.; Liu, P. C.; Liu, H. Z. Particle clustering during pearl chain formation in a conductive-island based dielectrophoretic assembly system. *RSC Adv.* **2015**, *5* (8), 5523−5532.

(164) Kretschmer, R.; Fritzsche, W. Pearl chain formation of nanoparticles in microelectrode gaps by dielectrophoresis. *Langmuir* **2004**, *20* (26), 11797−11801.

(165) Hermanson, K. D.; Lumsdon, S. O.; Williams, J. P.; Kaler, E. W.; Velev, O. D. Dielectrophoretic Assembly of Electrically Functional Microwires from Nanoparticle Suspensions. *Science* **2001**, *294* (5544), 1082−1086.

(166) Velev, O. D.; Gangwal, S.; Petsev, D. N. Particle-localized AC and DC manipulation and electrokinetics. *Annual reports on the progress of chemistry. Section C* **2009**, *105*, 213.

(167) Mittal, M.; Lele, P. P.; Kaler, E. W.; Furst, E. M. Polarization and interactions of colloidal particles in ac electric fields. *J. Chem. Phys.* **2008**, *129* (6), 064513.

(168) Gierhart, B.; Howitt, D. G.; Chen, S. J.; Smith, R.; Collins, S. D. Frequency dependence of gold nanoparticle superassembly by dielectrophoresis. *Langmuir* **2007**, *23* (24), 12450−12456.

(169) Lumsdon, S. O.; Kaler, E. W.; Velev, O. D. Two-dimensional crystallization of microspheres by a coplanar AC electric field. *Langmuir* **2004**, *20* (6), 2108−2116.

(170) Gangwal, S.; Cayre, O. J.; Velev, O. D. Dielectrophoretic Assembly of Metallodielectric Janus Particles in AC Electric Fields. *Langmuir* **2008**, *24* (23), 13312−13320.

(171) Bhatt, K. H.; Velev, O. D. Control and modeling of the dielectrophoretic assembly of on-chip nanoparticle wires. *Langmuir* **2004**, *20* (2), 467−476.

(172) Liu, W. Y.; Wang, C. H.; Ding, H. T.; Shao, J. Y.; Ding, Y. C. AC electric field induced dielectrophoretic assembly behavior of gold nanoparticles in a wide frequency range. *Appl. Surf. Sci.* **2016**, *370*, 184−192.

(173) Barsotti, R. J.; Vahey, M. D.; Wartena, R.; Chiang, Y. M.; Voldman, J.; Stellacci, F. Assembly of Metal Nanoparticles into Nanogaps. *Small* **2007**, *3* (3), 488−499.

(174) Bezryadin, A.; Dekker, C.; Schmid, G. Electrostatic trapping of single conducting nanoparticles between nanoelectrodes. *Appl. Phys. Lett.* **1997**, *71* (9), 1273−1275.

(175) Khondaker, S. I.; Luo, K.; Yao, Z. The fabrication of single-electron transistors using dielectrophoretic trapping of individual gold nanoparticles. *Nanotechnology* **2010**, *21* (9), 095204.

(176) Barik, A.; Chen, X.; Oh, S.-H. Ultralow-Power Electronic Trapping of Nanoparticles with Sub-10 nm Gold Nanogap Electrodes. *Nano Lett.* **2016**, *16* (10), 6317−6324.

(177) Maijenburg, A. W.; Maas, M. G.; Rodijk, E. J. B.; Ahmed, W.; Kooij, E. S.; Carlen, E. T.; Blank, D. H. A.; ten Elshof, J. E. Dielectrophoretic alignment of metal and metal oxide nanowires and nanotubes: A universal set of parameters for bridging prepatterned microelectrodes. *J. Colloid Interface Sci.* **2011**, *355* (2), 486−493.

(178) Abdulhameed, A.; Yunus, N. A. M.; Halin, I. A.; Hamidon, M. N. Simulation of dielectrophoretic alignment for carbon nanotube on indium tin oxide. *Materials Today: Proceedings* **2019**, *7*, 593−600.

(179) Chai, Z.; Seo, J.; Abbasi, S. A.; Busnaina, A. Assembly of Highly Aligned Carbon Nanotubes Using an Electro-Fluidic Assembly Process. *ACS Nano* **2018**, *12* (12), 12315−12323.

(180) Zheng, F. Z.; Yang, X.; Wu, Y.; Zhou, Z. Y.; Liu, Z. B. Large-scale directed assembly of single-walled carbon nanotube devices by alternating current coupling dielectrophoresis. *Carbon* **2017**, *124*, 693−699.

(181) Stokes, P.; Silbar, E.; Zayas, Y. M.; Khondaker, S. I. Solution processed large area field effect transistors from dielectrophoreticly aligned arrays of carbon nanotubes. *Appl. Phys. Lett.* **2009**, *94* (11), 113104.

(182) Vijayaraghavan, A.; Blatt, S.; Weissenberger, D.; Oron-Carl, M.; Hennrich, F.; Gerthsen, D.; Hahn, H.; Krupke, R. Ultra-large-scale directed assembly of single-walled carbon nanotube devices. *Nano Lett.* **2007**, *7* (6), 1556−1560.

(183) Kamat, P. V.; Thomas, K. G.; Barazzouk, S.; Girishkumar, G.; Vinodgopal, K.; Meisel, D. Self-assembled linear bundles of single wall carbon nanotubes and their alignment and deposition as a film in a dc field. *J. Am. Chem. Soc.* **2004**, *126* (34), 10757−10762.

(184) Cao, Q.; Han, S.-j.; Tulevski, G. S. Fringing-field dielectrophoretic assembly of ultrahigh-density semiconducting nanotube arrays with a self-limited pitch. *Nat. Commun.* **2014**, *5*, 5071.

(185) Abbasi, S. A.; Kim, T. H.; Somu, S.; Wang, H. L.; Chai, Z. M.; Upmanyu, M.; Busnaina, A. Fabrication of a nanoelectromechanical bistable switch using directed assembly of SWCNTs. *J. Phys. D: Appl. Phys.* **2020**, *53* (23), 23LT02.

(186) Yang, Z.; Wang, M.; Zhao, Q.; Qiu, H.; Li, J.; Li, X.; Shao, J. Dielectrophoretic-Assembled Single and Parallel-Aligned Ag Nanowire-ZnO-Branched Nanorod Heteronanowire Ultraviolet Photodetectors. *ACS Applied Materials Interfaces* **2017**, *9* (27), 22837−22845.

(187) Venkatesh, R.; Kundu, S.; Pradhan, A.; Sai, T. P.; Ghosh, A.; Ravishankar, N. Directed Assembly of Ultrathin Gold Nanowires over Large Area by Dielectrophoresis. *Langmuir* **2015**, *31* (33), 9246−9252.

(188) Papadakis, S. J.; Hoffmann, J. A.; Deglau, D.; Chen, A.; Tyagi, P.; Gracias, D. H. Quantitative analysis of parallel nanowire array assembly by dielectrophoresis. *Nanoscale* **2011**, *3* (3), 1059−1065.

(189) García Núñez, C.; Braña, A. F.; López, N.; Pau, J. L.; García, B. J. Single GaAs nanowire based photodetector fabricated by dielectrophoresis. *Nanotechnology* **2020**, *31* (22), 225604.

(190) Motayed, A.; He, M.; Davydov, A. V.; Melngailis, J.; Mohammad, S. N. Simple model for dielectrophoretic alignment of gallium nitride nanowires. *J. Vac. Sci. Technol. B* **2007**, *25* (1), 120−123.

(191) Kim, T. H.; Lee, S. Y.; Cho, N. K.; Seong, H. K.; Choi, H. J.; Jung, S. W.; Lee, S. K. Dielectrophoretic alignment of gallium nitride nanowires (GaN NWs) for use in device applications. *Nanotechnology* **2006**, *17* (14), 3394−3399.

(192) Jangir, S.; Malik, H. K.; Saho, P.; Muralidharan, R.; Srinivasan, T.; Mishra, P. Electrical transport and gas sensing characteristics of dielectrophoretically aligned MBE grown catalyst free InAs nanowires. *Nanotechnology* **2019**, *30* (10), 105706.

(193) Constantinou, M.; Hoettges, K. F.; Krylyuk, S.; Katz, M. B.; Davydov, A.; Rigas, G.-P.; Stolojan, V.; Hughes, M. P.; Shkunov, M. Rapid determination of nanowires electrical properties using a dielectrophoresis-well based system. *Appl. Phys. Lett.* **2017**, *110* (13), 133103.

(194) Constantinou, M.; Rigas, G. P.; Castro, F. A.; Stolojan, V.; Hoettges, K. F.; Hughes, M. P.; Adkins, E.; Korgel, B. A.; Shkunov, M. Simultaneous Tunable Selection and Self-Assembly of Si Nanowires from Heterogeneous Feedstock. *ACS Nano* **2016**, *10* (4), 4384−4394.

(195) Freer, E. M.; Grachev, O.; Duan, X.; Martin, S.; Stumbo, D. P. High-yield self-limiting single-nanowire assembly with dielectrophoresis. *Nat. Nanotechnol.* **2010**, *5* (7), 525−530.

(196) Singh, S. K.; Aryaan, N.; Shikder, M. R. A.; Byles, B. W.; Pomerantseva, E.; Subramanian, A. A 3D nanoelectrokinetic model for predictive assembly of nanowire arrays using floating electrode dielectrophoresis. *Nanotechnology* **2019**, *30* (2), 025301.

(197) Palapati, N. K. R.; Pomerantseva, E.; Subramanian, A. Single nanowire manipulation within dielectrophoretic force fields in the sub-crossover frequency regime. *Nanoscale* **2015**, *7* (7), 3109−3116.

(198) Kundu, S.; George, S. J.; Kulkarni, G. U. Electric field assisted assembly of 1D supramolecular nanofibres for enhanced super-capacitive performance. *Journal of Materials Chemistry A* **2020**, *8* (26), 13106−13113.

(199) Morrow, T. J.; Li, M.; Kim, J.; Mayer, T. S.; Keating, C. D. Programmed Assembly of DNA-Coated Nanowire Devices. *Science* **2009**, *323* (5912), 352−352.

(200) Raychaudhuri, S.; Dayeh, S. A.; Wang, D.; Yu, E. T. Precise Semiconductor Nanowire Placement Through Dielectrophoresis. *Nano Lett.* **2009**, *9* (6), 2260−2266.

(201) Li, W.; Hennrich, F.; Flavel, B. S.; Kappes, M. M.; Krupke, R. Chiral-index resolved length mapping of carbon nanotubes in solution using electric-field induced differential absorption spectroscopy. *Nanotechnology* **2016**, *27* (37), 375706.

(202) Benedict, L. X.; Louie, S. G.; Cohen, M. L. Static polarizabilities of single-wall carbon nanotubes. *Physical Review, B: Condensed Matter* **1995**, *52* (11), 8541−8549.

(203) Shekhar, S.; Stokes, P.; Khondaker, S. I. Ultrahigh density alignment of carbon nanotube arrays by dielectrophoresis. *ACS Nano* **2011**, *5* (3), 1739−1746.

(204) Deng, D. D.; Lin, Z.; Elias, A. L.; Perea-Lopez, N.; Li, J.; Zhou, C. J.; Zhang, K. H.; Feng, S. M.; Terrones, H.; Mayer, J. S.; Robinson, J. A.; Terrones, M.; Mayer, T. S. Electric-Field-Assisted Directed Assembly of Transition Metal Dichalcogenide Monolayer Sheets. *ACS Nano* **2016**, *10* (5), 5006−5014.

(205) Chai, Z.; Yilmaz, C.; Busnaina, A. A.; Lissandrello, C. A.; Carter, D. J. D. Directed assembly-based printing of homogeneous and hybrid nanorods using dielectrophoresis. *Nanotechnology* **2017**, *28* (47), 475303.

(206) Leiterer, C.; Deckert-Gaudig, T.; Singh, P.; Wirth, J.; Deckert, V.; Fritzsche, W. Dielectrophoretic positioning of single nanoparticles on atomic force microscope tips for tip-enhanced Raman spectroscopy. *Electrophoresis* **2015**, *36* (9−10), 1142−1148.

(207) Yilmaz, C.; Kim, T. H.; Somu, S.; Busnaina, A. A. Large-Scale Nanorods Nanomanufacturing by Electric-Field-Directed Assembly for Nanoscale Device Applications. *IEEE Trans. Nanotechnol.* **2010**, *9* (5), 653−658.

(208) Cetin, A. E.; Yanik, A. A.; Yilmaz, C.; Somu, S.; Busnaina, A.; Altug, H. Monopole antenna arrays for optical trapping, spectroscopy, and sensing. *Appl. Phys. Lett.* **2011**, *98* (11), 111110.

(209) Kim, T.-H.; Yilmaz, C.; Somu, S.; Busnaina, A. 3-D perpendicular assembly of SWNTs for CMOS interconnects. *Electronic Materials Letters* **2013**, *9* (6), 763−766.

(210) Makaram, P.; Selvarasah, S.; Xiong, X.; Chen, C.-L.; Busnaina, A.; Khanduja, N.; Dokmeci, M. R. Three-dimensional assembly of single-walled carbon nanotube interconnects using dielectrophoresis. *Nanotechnology* **2007**, *18* (39), 395204.

(211) Thrift, W. J.; Nguyen, C. Q.; Darvishzadeh-Varcheie, M.; Zare, S.; Sharac, N.; Sanderson, R. N.; Dupper, T. J.; Hochbaum, A. I.; Capolino, F.; Abdolhosseini Qomi, M. J.; Ragan, R. Driving Chemical Reactions in Plasmonic Nanogaps with Electrohydrodynamic Flow. *ACS Nano* **2017**, *11* (11), 11317−11329.

(212) Song, M. G.; Bishop, K. J. M.; Pinchuk, A. O.; Kowalczyk, B.; Grzybowski, B. A. Formation of Dense Nanoparticle Monolayers Mediated by Alternating Current Electric Fields and Electrohydrodynamic Flows. *J. Phys. Chem. C* **2010**, *114* (19), 8800−8805.

(213) Fagan, J. A.; Sides, P. J.; Prieve, D. C. Evidence of multiple electrohydrodynamic forces acting on a colloidal particle near an electrode due to an alternating current electric field. *Langmuir* **2005**, *21* (5), 1784−1794.

(214) Gong, T.; Wu, D.; Marr, D. Two-dimensional electro-hydrodynamically induced colloidal phases. *Langmuir* **2002**, *18* (26), 10064−10067.

(215) Böhmer. In Situ Observation of 2-Dimensional Clustering during Electrophoretic Deposition. *Langmuir* **1996**, *12* (24), 5747−5750.

(216) Solomentsev, Y.; Böhmer, M.; Anderson, J. L. Particle Clustering and Pattern Formation during Electrophoretic Deposition: A Hydrodynamic Model. *Langmuir* **1997**, *13* (23), 6058−6068.

(217) Solomentsev, Y.; Guelcher, S. A.; Bevan, M.; Anderson, J. L. Aggregation Dynamics for Two Particles during Electrophoretic Deposition under Steady Fields. *Langmuir* **2000**, *16* (24), 9208−9216.

(218) Golding, R. K.; Lewis, P. C.; Kumacheva, E.; Allard, M.; Sargent, E. H. In situ study of colloid crystallization in constrained geometry. *Langmuir* **2004**, *20* (4), 1414−1419.

(219) Trau, M.; Saville, D. A.; Aksay, I. A. Assembly of Colloidal Crystals at Electrode Interfaces. *Langmuir* **1997**, *13* (24), 6375−6381.

(220) Trau; Saville; Aksay. Field-Induced Layering of Colloidal Crystals. *Science* **1996**, *272* (5262), 706−709.

(221) Ristenpart, W. D.; Aksay, I. A.; Saville, D. A. Assembly of colloidal aggregates by electrohydrodynamic flow: Kinetic experiments and scaling analysis. *Phys. Rev. E* **2004**, *69* (2), 021405.

(222) Ristenpart, W.; Aksay, I.; Saville, D. Electrohydrodynamic flow around a colloidal particle near an electrode with an oscillating potential. *J. Fluid Mech.* **2007**, *575*, 83−109.

(223) Ristenpart, W.; Aksay, I.; Saville, D. Electrically guided assembly of planar superlattices in binary colloidal suspensions. *Phys. Rev. Lett.* **2003**, *90* (12), 128303.

(224) Bhatt, K. H.; Grego, S.; Velev, O. D. An AC electrokinetic technique for collection and concentration of particles and cells on patterned electrodes. *Langmuir* **2005**, *21* (14), 6603−6612.

(225) Dutcher, C. S.; Woehl, T. J.; Talken, N. H.; Ristenpart, W. D. Hexatic-to-disorder transition in colloidal crystals near electrodes: rapid annealing of polycrystalline domains. *Phys. Rev. Lett.* **2013**, *111* (12), 128302.

(226) Wirth, C. L.; Sides, P. J.; Prieve, D. C. Electrolyte dependence of particle motion near an electrode during ac polarization. *Phys. Rev. E* **2013**, *87* (3), 032302.

(227) Kim, J.; Anderson, J. L.; Garoff, S.; Sides, P. J. Effects of Zeta Potential and Electrolyte on Particle Interactions on an Electrode under ac Polarization. *Langmuir* **2002**, *18* (14), 5387−5391.

(228) Woehl, T. J.; Heatley, K. L.; Dutcher, C. S.; Talken, N. H.; Ristenpart, W. D. Electrolyte-Dependent Aggregation of Colloidal Particles near Electrodes in Oscillatory Electric Fields. *Langmuir* **2014**, *30* (17), 4887−4894.

(229) Saini, S.; Bukosky, S. C.; Ristenpart, W. D. Influence of Electrolyte Concentration on the Aggregation of Colloidal Particles near Electrodes in Oscillatory Fields. *Langmuir* **2016**, *32* (17), 4210−4216.

(230) Yeh, S.-R.; Seul, M.; Shraiman, B. Assembly of ordered colloidal aggregates by electric-field-induced fluid flow. *Nature* **1997**, *386* (6620), 57−59.

(231) Choi, W. M.; Park, O. The fabrication of micropatterns of a 2D colloidal assembly by electrophoretic deposition. *Nanotechnology* **2006**, *17* (1), 325−329.

(232) Ristenpart, W. D.; Jiang, P.; Slowik, M. A.; Punckt, C.; Saville, D. A.; Aksay, I. A. Electrohydrodynamic flow and colloidal patterning near inhomogeneities on electrodes. *Langmuir* **2008**, *24* (21), 12172−12180.

(233) Kumacheva, E.; Golding, R. K.; Allard, M.; Sargent, E. H. Colloid Crystal Growth on Mesoscopically Patterned Surfaces: Effect of Confinement. *Adv. Mater.* **2002**, *14* (3), 221−224.

(234) Gong, C.; Deng, W.; Zou, B.; Xing, Y.; Zhang, X.; Zhang, X.; Jie, J. Large-scale assembly of organic micro/nanocrystals into highly ordered patterns and their applications for strain sensors. *ACS Appl. Mater. Interfaces* **2014**, *6* (14), 11018−11024.

(235) Goel, M.; Singh, A.; Bhola, A.; Gupta, S. Size-Tunable Assembly of Gold Nanoparticles Using Competitive AC Electrokinetics. *Langmuir* **2019**, *35* (24), 8015−8024.

(236) Ramos, A.; Morgan, H.; Green, N. G.; Castellanos, A. The role of electrohydrodynamic forces in the dielectrophoretic manipulation and separation of particles. *J. Electrost.* **1999**, *47* (1−2), 71−81.

(237) Ramos, A.; Morgan, H.; Green, N. G.; Castellanos, A. AC Electric-Field-Induced Fluid Flow in Microelectrodes. *J. Colloid Interface Sci.* **1999**, *217* (2), 420−422.

(238) Green; Ramos; Gonzalez; Morgan; Castellanos. Fluid flow induced by nonuniform ac electric fields in electrolytes on micro-

electrodes. I. Experimental measurements. *Phys. Rev. E* **2000**, *61* (4), 4011−4018.

(239) Ramos, A.; González, A.; Castellanos, A.; Green, N. G.; Morgan, H. Pumping of liquids with ac voltages applied to asymmetric pairs of microelectrodes. *Phys. Rev. E* **2003**, *67* (5), 056302.

(240) Ristenpart, W. D.; Aksay, I. A.; Saville, D. A. Electrically driven flow near a colloidal particle close to an electrode with a faradaic current. *Langmuir* **2007**, *23* (7), 4071−4080.

(241) Demirörs, A. F.; Alison, L. Electric Field Assembly of Colloidal Superstructures. *J. Phys. Chem. Lett.* **2018**, *9* (15), 4437−4443.

(242) Guelcher, S. A.; Solomentsev, Y.; Anderson, J. L. Aggregation of pairs of particles on electrodes during electrophoretic deposition. *Powder Technol.* **2000**, *110* (1), 90−97.

(243) Mehraeen, S.; Asbahi, M.; Fuke, W.; Yang, J. K. W.; Cao, J.; Tan, M. C. Directed Self-Assembly of sub-10 nm Particles: Role of Driving Forces and Template Geometry in Packing and Ordering. *Langmuir* **2015**, *31* (31), 8548−8557.

(244) Han, W.; Byun, M.; Lin, Z. Assembling and positioning latex nanoparticles via controlled evaporative self-assembly. *J. Mater. Chem.* **2011**, *21* (42), 16968−16972.

(245) Fan, F.; Stebe, K. J. Assembly of colloidal particles by evaporation on surfaces with patterned hydrophobicity. *Langmuir* **2004**, *20* (8), 3062−3067.

(246) Malaquin, L.; Kraus, T.; Schmid, H.; Delamarche, E.; Wolf, H. Controlled particle placement through convective and capillary assembly. *Langmuir* **2007**, *23* (23), 11513−11521.

(247) Watanabe, S.; Mino, Y.; Ichikawa, Y.; Miyahara, M. T. Spontaneous Formation of Cluster Array of Gold Particles by Convective Self-Assembly. *Langmuir* **2012**, *28* (36), 12982−12988.

(248) Dague, E.; Jauvert, E.; Laplatine, L.; Viallet, B.; Thibault, C.; Ressier, L. Assembly of live micro-organisms on microstructured pdms stamps by convective/capillary deposition for afm bio-experiments. *Nanotechnology* **2011**, *22* (39), 395102.

(249) Thai, T.; Zheng, Y.; Ng, S. H.; Mudie, S.; Altissimo, M.; Bach, U. Self-Assembly of Vertically Aligned Gold Nanorod Arrays on Patterned Substrates. *Angew. Chem., Int. Ed.* **2012**, *51* (35), 8732−8735.

(250) Fustin, C.-A.; Glasser, G.; Spiess, H. W.; Jonas, U. Parameters influencing the templated growth of colloidal crystals on chemically patterned surfaces. *Langmuir* **2004**, *20* (21), 9114−9123.

(251) Fustin, C. A.; Glasser, G.; Spiess, H. W.; Jonas, U. Site-Selective Growth of Colloidal Crystals with Photonic Properties on Chemically Patterned Surfaces. *Adv. Mater.* **2003**, *15* (12), 1025−1028.

(252) Prevo, B. G.; Velev, O. D. Controlled, rapid deposition of structured coatings from micro- and nanoparticle suspensions. *Langmuir* **2004**, *20* (6), 2099−2107.

(253) Yang, S. M.; Míguez, H.; Ozin, G. A. Opal Circuits of Light—Planarized Microphotonic Crystal Chips. *Adv. Funct. Mater.* **2002**, *12* (6−7), 425−431.

(254) Jaber-Ansari, L.; Hahm, M. G.; Somu, S.; Sanz, Y. E.; Busnaina, A.; Jung, Y. J. Mechanism of very large scale assembly of SWNTs in template guided fluidic assembly process. *J. Am. Chem. Soc.* **2009**, *131* (2), 804−808.

(255) Xiong, X.; Jaberansari, L.; Hahm, M. G.; Busnaina, A.; Jung, Y. J. Building highly organized singte-walled-carbon-nanotube networks using template-guided fluidic assembly. *Small* **2007**, *3* (12), 2006−2010.

(256) Xiong, X. G.; Chen, C. L.; Ryan, P.; Busnaina, A. A.; Jung, Y. J.; Dokmeci, M. R. Directed assembly of high density single-walled carbon nanotube patterns on flexible polymer substrates. *Nanotechnology* **2009**, *20* (29), 295302.

(257) Liddle, J. A.; Cui, Y.; Alivisatos, P. Lithographically-directed self-assembly of nanostructures. *J. Vac. Sci. Technol. B* **2004**, *22*, 3409−3414.

(258) Kralchevsky, P. A.; Denkov, N. D. Capillary forces and structuring in layers of colloid particles. *Curr. Opin. Colloid Interface Sci.* **2001**, *6* (4), 383−401.

(259) Nagayama, K. Two-dimensional self-assembly of colloids in thin liquid films. *Colloids Surf., A* **1996**, *109*, 363−374.

(260) Denkov, N. D.; Velev, O. D.; Kralchevsky, P. A.; Ivanov, I. B.; Yoshimura, H.; Nagayama, K. Two-dimensional crystallization. *Nature* **1993**, *361* (6407), 26.

(261) Dimitrov, A. S.; Nagayama, K. Continuous Convective Assembling of Fine Particles into Two-Dimensional Arrays on Solid Surfaces. *Langmuir* **1996**, *12* (5), 1303−1311.

(262) Kubiak, K.; Adamczyk, Z.; Maciejewska, J.; Oćwieja, M. Gold Nanoparticle Monolayers of Controlled Coverage and Structure. *J. Phys. Chem. C* **2016**, *120* (22), 11807−11819.

(263) Winkler, K.; Paszewski, M.; Kalwarczyk, T.; Kalwarczyk, E.; Wojciechowski, T.; Gorecka, E.; Pociecha, D.; Holyst, R.; Fialkowski, M. Ionic strength-controlled deposition of charged nanoparticles on a solid substrate. *J. Phys. Chem. C* **2011**, *115* (39), 19096−19103.

(264) Ni, S.; Isa, L.; Wolf, H. Capillary assembly as a tool for the heterogeneous integration of micro- and nanoscale objects. *Soft Matter* **2018**, *14* (16), 2978−2995.

(265) Meng, y.; Cheng, G.; Man, Z.; Xu, Y.; Zhou, S.; Bian, J.; Lu, z.; Zhang, W. Deterministic Assembly of Single Sub-20 nm Functional Nanoparticles Using a Thermally Modified Template with a Scanning Nanoprobe. *Adv. Mater.* **2020**, *32*, 2005979.

(266) Gupta, V.; Probst, P. T.; Gossler, F. R.; Steiner, A. M.; Schubert, J.; Brasse, Y.; Konig, T. A. F.; Fery, A. Mechanotunable Surface Lattice Resonances in the Visible Optical Range by Soft Lithography Templates and Directed Self-Assembly. *ACS Appl. Mater. Interfaces* **2019**, *11* (31), 28189−28196.

(267) Greybush, N. J.; Liberal, I.; Malassis, L.; Kikkawa, J. M.; Engheta, N.; Murray, C. B.; Kagan, C. R. Plasmon Resonances in Self-Assembled Two-Dimensional Au Nanocrystal Metamolecules. *ACS Nano* **2017**, *11* (3), 2917−2927.

(268) Holzner, F.; Kuemin, C.; Paul, P.; Hedrick, J.; Wolf, H.; Spencer, N.; Duerig, U.; Knoll, A. Directed Placement of Gold Nanorods Using a Removable Template for Guided Assembly. *Nano Lett.* **2011**, *11* (9), 3957−3962.

(269) Cui, Y.; Bjork, M. T.; Liddle, J. A.; Sonnichsen, C.; Boussert, B.; Alivisatos, A. P. Integration of colloidal nanocrystals into lithographically patterned devices. *Nano Lett.* **2004**, *4* (6), 1093−1098.

(270) Yin, Y.; Lu, Y.; Gates, B.; Xia, Y. Template-assisted self-assembly: a practical route to complex aggregates of monodispersed colloids with well-defined sizes, shapes, and structures. *J. Am. Chem. Soc.* **2001**, *123* (36), 8718−8729.

(271) Kraus, T.; Malaquin, L.; Schmid, H.; Riess, W.; Spencer, N. D.; Wolf, H. Nanoparticle printing with single-particle resolution. *Nat. Nanotechnol.* **2007**, *2* (9), 570−576.

(272) Kang, J.; Park, C.-G.; Lee, S.-H.; Cho, C.; Choi, D.-G.; Lee, J.-Y. Fabrication of high aspect ratio nanogrid transparent electrodes via capillary assembly of Ag nanoparticles. *Nanoscale* **2016**, *8* (21), 11217−11223.

(273) Asbahi, M.; Mehraeen, S.; Wang, F.; Yakovlev, N.; Chong, K. S. L.; Cao, J.; Tan, M. C.; Yang, J. K. W. Large Area Directed Self-Assembly of Sub-10 nm Particles with Single Particle Positioning Resolution. *Nano Lett.* **2015**, *15* (9), 6066−6070.

(274) Greybush, N. J.; Saboktakin, M.; Ye, X.; Della Giovampaola, C.; Oh, S. J.; Berry, N. E.; Engheta, N.; Murray, C. B.; Kagan, C. R. Plasmon-enhanced upconversion luminescence in single nanophosphor-nanorod heterodimers formed through template-assisted self-assembly. *ACS Nano* **2014**, *8* (9), 9482−9491.

(275) Fan, J. A.; Bao, K.; Sun, L.; Bao, J.; Manoharan, V. N.; Nordlander, P.; Capasso, F. Plasmonic Mode Engineering with Templated Self-Assembled Nanoclusters. *Nano Lett.* **2012**, *12* (10), 5318−5324.

(276) Kuemin, C.; Cathrein Huckstadt, K.; Lörtscher, E.; Rey, A.; Decker, A.; Spencer, N. D.; Wolf, H. Selective Assembly of Sub-Micrometer Polymer Particles. *Adv. Mater.* **2010**, *22* (25), 2804−2808.

(277) Cerf, A.; Molnár, G.; Vieu, C. Novel approach for the assembly of highly efficient SERS substrates. *ACS Appl. Mater. Interfaces* **2009**, *1* (11), 2544−2550.

(278) Kuemin, C.; Stutz, R.; Spencer, N. D.; Wolf, H. Precise Placement of Gold Nanorods by Capillary Assembly. *Langmuir* **2011**, *27* (10), 6305−6310.

(279) Kuemin, C.; Nowack, L.; Bozano, L.; Spencer, N. D.; Wolf, H. Oriented Assembly of Gold Nanorods on the Single-Particle Level. *Adv. Funct. Mater.* **2012**, *22* (4), 702−708.

(280) Zhou, X.; Zhou, Y.; Ku, J. C.; Zhang, C.; Mirkin, C. A. Capillary force-driven, large-area alignment of multi-segmented nanowires. *ACS Nano* **2014**, *8* (2), 1511−1516.

(281) Zhou, Y.; Zhou, X.; Park, D. J.; Torabi, K.; Brown, K. A.; Jones, M. R.; Zhang, C.; Schatz, G. C.; Mirkin, C. A. Shape-selective deposition and assembly of anisotropic nanoparticles. *Nano Lett.* **2014**, *14* (4), 2157−2161.

(282) Jiang, L.; Chen, X.; Lu, N.; Chi, L. Spatially confined assembly of nanoparticles. *Acc. Chem. Res.* **2014**, *47* (10), 3009−3017.

(283) Henzie, J.; Andrews, S. C.; Ling, X. Y.; Li, Z.; Yang, P. Oriented assembly of polyhedral plasmonic nanoparticle clusters. *Proc. Natl. Acad. Sci. U.S.A.* **2013**, *110* (17), 6640−6645.

(284) Rey, A.; Billardon, G.; Lörtscher, E.; Moth-Poulsen, K.; Stuhr-Hansen, N.; Wolf, H.; Bjørnholm, T.; Stemmer, A.; Riel, H. Deterministic assembly of linear gold nanorod chains as a platform for nanoscale applications. *Nanoscale* **2013**, *5* (18), 8680−8688.

(285) Flauraud, V.; Mastrangeli, M.; Bernasconi, G. D.; Butet, J.; Alexander, D. T. L.; Shahrabi, E.; Martin, O. J. F.; Brugger, J. Nanoscale topographical control of capillary assembly of nanoparticles. *Nat. Nanotechnol.* **2017**, *12* (1), 73−81.

(286) Ni, S.; Leemann, J.; Wolf, H.; Isa, L. Insights into mechanisms of capillary assembly. *Faraday Discuss.* **2015**, *181*, 225−242.

(287) Ni, S.; Leemann, J.; Buttinoni, I.; Isa, L.; Wolf, H. Programmable colloidal molecules from sequential capillarity-assisted particle assembly. *Science Advances* **2016**, *2* (4), No. e1501779.

(288) Ni, S.; Wolf, H.; Isa, L. Programmable Assembly of Hybrid Nanoclusters. *Langmuir* **2018**, *34* (7), 2481−2488.

(289) Park, N.-G.; Zhu, K. Scalable fabrication and coating methods for perovskite solar cells and solar modules. *Nature Reviews Materials* **2020**, *5* (5), 333−350.

(290) Lu, Z.; Wang, C.; Deng, W.; Achille, M. T.; Jie, J.; Zhang, X. Meniscus-guided coating of organic crystalline thin films for high-performance organic field-effect transistors. *J. Mater. Chem. C* **2020**, *8* (27), 9133−9146.

(291) Dai, X.; Deng, Y.; Van Brackle, C. H.; Huang, J. Meniscus fabrication of halide perovskite thin films at high throughput for large area and low-cost solar panels. *International Journal of Extreme Manufacturing* **2019**, *1* (2), 022004.

(292) Lee, S. B.; Lee, S.; Kim, D. G.; Kim, S. H.; Kang, B.; Cho, K. Solutal-Marangoni-Flow-Mediated Growth of Patterned Highly Crystalline Organic Semiconductor Thin Film Via Gap-Controlled Bar Coating. *Adv. Funct. Mater.* **2021**, *31* (28), 2100196.

(293) Wang, C.; Lu, Z.; Deng, W.; Zhao, W.; Lu, B.; Xiao, J.; Zhang, X.; Jie, J.; Zhang, X. Precise patterning of single crystal arrays of organic semiconductors by a patterned microchannel dip-coating method for organic field-effect transistors. *J. Mater. Chem. C* **2021**, *9* (15), 5174−5181.

(294) Abbasi, S. A.Surface Engineering Assisted Directed Assembly-Based Printing of Electronic Devices. *Ph.D. Thesis*, Northeastern University, Boston, MA, 2019.

(295) Kim, D.-K.; Park, J.-I.; Jang, J.; Kang, I. M.; Park, J.; Bae, J.-H. Expeditious and eco-friendly solution-free self-patterning of sol-gel oxide semiconductor thin films. *Materials & Design* **2020**, *194*, 108949.

(296) Xin, Z.; Yan, M.; Gu, L.; Liu, J.; Liu, R.; Li, L.; Fang, Y.; Mo, L.; Li, Y.; Shen, Y.; Guolin, X.; Li, M.; Yang, L. Scalable Fabrication of Conductive Lines by Patterned Wettability-Assisted Bar-Coating for Low Cost Paper-Based Circuits. *Advanced Materials Interfaces* **2019**, *6* (10), 1802047.

(297) Zhang, X.; Deng, W.; Jia, R.; Zhang, X.; Jie, J. Precise Patterning of Organic Semiconductor Crystals for Integrated Device Applications. *Small* **2019**, *15* (27), 1900332.

(298) Schmaltz, T.; Sforazzini, G.; Reichert, T.; Frauenrath, H. Self-Assembled Monolayers as Patterning Tool for Organic Electronic Devices. *Adv. Mater.* **2017**, *29* (18), 1605286.

(299) Hoffmann, J.; Gamboa, S. M.; Hofmann, A.; Gliemann, H.; Welle, A.; Wacker, I.; Schröder, R. R.; Ness, L.; Hagenmeyer, V.;

Gengenbach, U. Siloxane-functionalised surface patterns as templates for the ordered deposition of thin lamellar objects. *Sci. Rep.* **2019**, *9* (1), 17952.

(300) Chen, S.; Ma, X.; Cai, Z.; Long, H.; Wang, X.; Li, Z.; Qu, Z.; Zhang, F.; Qiao, Y.; Song, Y. A Direct Writing Approach for Organic Semiconductor Single-Crystal Patterns with Unique Orientation. *Adv. Mater.* **2022**, *34*, 2200928.

(301) Giri, G.; Miller, E.; Bao, Z. Selective solution shearing deposition of high performance TIPS-pentacene polymorphs through chemical patterning. *J. Mater. Res.* **2014**, *29* (22), 2615−2624.

(302) Mandsberg, N. K.; Hansen, O.; Taboryski, R. Generation of micro-droplet arrays by dip-coating of biphilic surfaces; the dependence of entrained droplet volume on withdrawal velocity. *Sci. Rep.* **2017**, *7* (1), 12794.

(303) Li, L.; Li, W.; Sun, Q.; Liu, X.; Jiu, J.; Tenjimbayashi, M.; Kanehara, M.; Nakayama, T.; Minari, T. Dual Surface Architectonics for Directed Self-Assembly of Ultrahigh-Resolution Electronics. *Small* **2021**, *17* (26), 2101754.

(304) Belgardt, C.; Blaudeck, T.; von Borczyskowski, C.; Graaf, H. Self-Assembly of Ordered Colloidal Nanoparticle Films in Few-Micron Wide Laser-Desorbed Lines of Octadecylsiloxane Monolayers on Silicon Oxide Surfaces. *Adv. Eng. Mater.* **2014**, *16* (9), 1090−1097.

(305) Yamada, T.; Fukuhara, K.; Matsuoka, K.; Minemawari, H.; Tsutsumi, J. y.; Fukuda, N.; Aoshima, K.; Arai, S.; Makita, Y.; Kubo, H.; Enomoto, T.; Togashi, T.; Kurihara, M.; Hasegawa, T. Nanoparticle chemisorption printing technique for conductive silver patterning with submicron resolution. *Nat. Commun.* **2016**, *7* (1), 11402.

(306) van Gestel, M. A. C.; He, B.; Darhuber, A. A. Formation of residual droplets upon dip-coating of chemical and topographical surface patterns on partially wettable substrates. *Chem. Eng. Sci.* **2020**, *227*, 115832.

(307) Brasjen, B. J.; Wedershoven, H. M. J. M.; van Cuijk, A. W.; Darhuber, A. A. Dip- and die-coating of hydrophilic squares on flat, hydrophobic substrates. *Chem. Eng. Sci.* **2017**, *158*, 340−348.

(308) Brasjen, B. J.; van Cuijk, A. W.; Darhuber, A. A. Dip-coating of chemically patterned surfaces. *Chemical Engineering and Processing: Process Intensification* **2011**, *50* (5), 565−568.

(309) Pierre, A.; Sadeghi, M.; Payne, M. M.; Facchetti, A.; Anthony, J. E.; Arias, A. C. All-Printed Flexible Organic Transistors Enabled by Surface Tension-Guided Blade Coating. *Adv. Mater.* **2014**, *26* (32), 5722−5727.

(310) Reynolds, T. D.; Kalpathy, S. K.; Kumar, S.; Francis, L. F. Dip coating of charged colloidal suspensions onto substrates with patterned wettability: Coating regime maps. *J. Colloid Interface Sci.* **2010**, *352* (1), 202−210.

(311) Deegan, R. D.; Bakajin, O.; Dupont, T. F.; Huber, G.; Nagel, S. R.; Witten, T. A. Capillary flow as the cause of ring stains from dried liquid drops. *Nature* **1997**, *389* (6653), 827−829.

(312) Gao, M.; Li, L. H.; Song, Y. L. Inkjet printing wearable electronic devices. *J. Mater. Chem. C* **2017**, *5* (12), 2971−2993.

(313) Kim, D.; Jeong, S.; Park, B. K.; Moon, J. Direct writing of silver conductive patterns: Improvement of film morphology and conductance by controlling solvent compositions. *Appl. Phys. Lett.* **2006**, *89* (26), 264101.

(314) Inanlu, M. J.; Shojaan, B.; Farhadi, J.; Bazargan, V. Effect of Particle Concentration on Surfactant-Induced Alteration of the Contact Line Deposition in Evaporating Sessile Droplets. *Langmuir* **2021**, *37* (8), 2658−2666.

(315) Shao, X.; Duan, F.; Hou, Y.; Zhong, X. Role of surfactant in controlling the deposition pattern of a particle-laden droplet: Fundamentals and strategies. *Adv. Colloid Interface Sci.* **2020**, *275*, 102049.

(316) Zhu, Z.; Ning, H.; Cai, W.; Wei, J.; Zhou, S.; Yao, R.; Lu, X.; Zhang, J.; Zhou, Z.; Peng, J. Morphology Modulation of Direct Inkjet Printing by Incorporating Polymers and Surfactants into a Sol-Gel Ink System. *Langmuir* **2018**, *34* (22), 6413−6419.

(317) Chai, Z.; Korkmaz, A.; Yilmaz, C.; Busnaina, A. A. High-Rate Printing of Micro/Nanoscale Patterns Using Interfacial Convective Assembly. *Adv. Mater.* **2020**, *32* (22), 2000747.

(318) Darhuber, A. A.; Troian, S. M.; Davis, J. M.; Miller, S. M.; Wagner, S. Selective dip-coating of chemically micropatterned surfaces. *J. Appl. Phys.* **2000**, *88* (9), 5119−5126.

(319) Sirman, A.Development of high-rate electro-fluidic directed assembly of nanoelements on insulating surfaces for sensor applications. *Ph.D. Thesis*, Northeastern University, Boston, MA, 2014.

(320) Collet, M.; Salomon, S.; Klein, N. Y.; Seichepine, F.; Vieu, C.; Nicu, L.; Larrieu, G. Large-Scale Assembly of Single Nanowires through Capillary-Assisted Dielectrophoresis. *Adv. Mater.* **2015**, *27* (7), 1268−1273.

(321) Cho, H. C.; Somu, S.; Lee, J. Y.; Jeong, H. B.; Busnaina, A. High-Rate Nanoscale Offset Printing Process Using Directed Assembly and Transfer of Nanomaterials. *Adv. Mater.* **2015**, *27* (10), 1759−1766.

(322) Chai, Z.; Jeong, H.; Abbasi, S. A.; Busnaina, A. A. Fabrication of organic field effect transistors using directed assembled and transfer printed carbon nanotube source/drain electrodes. *Appl. Phys. Lett.* **2019**, *114* (10), 103301.

(323) Wang, W.-H.; Abbasi, S. A.; Chai, Z.; Jeong, H.; Busnaina, A. Solution processed all-carbon transistors via directed assembly and transfer printing of CNT channel and electrodes. *Applied physics letters* **2020**, *117* (13), 133101.

(324) Abbasi, S. A.; Busnaina, A.; Isaacs, J. A. Cumulative Energy Demand for Printing Nanoscale Electronics. *Procedia CIRP* **2019**, *80*, 298−303.

(325) Wang, M.; He, L.; Yin, Y. Magnetic field guided colloidal assembly. *Mater. Today* **2013**, *16* (4), 110−116.

(326) Li, Z.; Yang, F.; Yin, Y. Smart Materials by Nanoscale Magnetic Assembly. *Adv. Funct. Mater.* **2020**, *30* (2), 1903467.

(327) Cao, Q. L.; Fan, Q.; Chen, Q.; Liu, C. T.; Han, X. T.; Li, L. Recent advances in manipulation of micro- and nano-objects with magnetic fields at small scales. *Materials Horizons* **2020**, *7* (3), 638−666.

(328) Sherman, Z. M.; Swan, J. W. Transmutable Colloidal Crystals and Active Phase Separation via Dynamic, Directed Self-Assembly with Toggled External Fields. *ACS Nano* **2019**, *13* (1), 764−771.

(329) Malik, V.; Pal, A.; Pravaz, O.; Crassous, J. J.; Granville, S.; Grobety, B.; Hirt, A. M.; Dietsch, H.; Schurtenberger, P. Hybrid magnetic iron oxide nanoparticles with tunable field-directed self-assembly. *Nanoscale* **2017**, *9* (38), 14405−14413.

(330) Ge, J.; He, L.; Hu, Y.; Yin, Y. Magnetically induced colloidal assembly into field-responsive photonic structures. *Nanoscale* **2011**, *3* (1), 177−183.

(331) Li, K. H.; Yellen, B. B. Magnetically tunable self-assembly of colloidal rings. *Appl. Phys. Lett.* **2010**, *97* (8), 083105.

(332) Tracy, J. B.; Crawford, T. M. Magnetic field-directed self-assembly of magnetic nanoparticles. *MRS Bull.* **2013**, *38* (11), 915−920.

(333) Velez, C.; Torres-Díaz, I.; Maldonado-Camargo, L.; Rinaldi, C.; Arnold, D. P. Magnetic Assembly and Cross-Linking of Nanoparticles for Releasable Magnetic Microstructures. *ACS Nano* **2015**, *9* (10), 10165−10172.

(334) Yang, Z.; Wei, J.; Gizynski, K.; Song, M.-G.; Grzybowski, B. A. Interference-like patterns of static magnetic fields imprinted into polymer/nanoparticle composites. *Nat. Commun.* **2017**, *8* (1), 1564.

(335) Lim, J.; Lanni, C.; Evarts, E. R.; Lanni, F.; Tilton, R. D.; Majetich, S. A. Magnetophoresis of Nanoparticles. *ACS Nano* **2011**, *5* (1), 217−226.

(336) Ayansiji, A. O.; Dighe, A. V.; Linninger, A. A.; Singh, M. R. Constitutive relationship and governing physical properties for magnetophoresis. *Proc. Natl. Acad. Sci. U. S. A.* **2020**, *117*, 30208.

(337) Leong, S. S.; Ahmad, Z.; Low, S. C.; Camacho, J.; Faraudo, J.; Lim, J. Unified View of Magnetic Nanoparticle Separation under Magnetophoresis. *Langmuir* **2020**, *36* (28), 8033−8055.

(338) Gijs, M. A. M.; Lacharme, F.; Lehmann, U. Microfluidic Applications of Magnetic Particles for Biological Analysis and Catalysis. *Chem. Rev.* **2010**, *110* (3), 1518−1563.

(339) Tarn, M. D.; Hirota, N.; Iles, A.; Pamme, N. On-chip diamagnetic repulsion in continuous flow. *Sci. Technol. Adv. Mater.* **2009**, *10* (1), 014611.

(340) Alnaimat, F.; Dagher, S.; Mathew, B.; Hilal-Alnqbi, A.; Khashan, S. Microfluidics Based Magnetophoresis: A Review. *Chem. Rec.* **2018**, *18* (11), 1596−1612.

(341) Krebs, M. D.; Erb, R. M.; Yellen, B. B.; Samanta, B.; Bajaj, A.; Rotello, V. M.; Alsberg, E. Formation of Ordered Cellular Structures in Suspension via Label-Free Negative Magnetophoresis. *Nano Lett.* **2009**, *9* (5), 1812−1817.

(342) Winkleman, A.; Gudiksen, K. L.; Ryan, D.; Whitesides, G. M.; Greenfield, D.; Prentiss, M. A magnetic trap for living cells suspended in a paramagnetic buffer. *Appl. Phys. Lett.* **2004**, *85* (12), 2411−2413.

(343) Skjeltorp, A. T. One- and Two-Dimensional Crystallization of Magnetic Holes. *Phys. Rev. Lett.* **1983**, *51* (25), 2306−2309.

(344) Munaz, A.; Shiddiky, M. J. A.; Nguyen, N.-T. Recent advances and current challenges in magnetophoresis based micro magneto-fluidics. *Biomicrofluidics* **2018**, *12* (3), 031501.

(345) Odenbach, S. Ferrofluids—magnetically controlled suspensions. *Colloids Surf., A* **2003**, *217* (1), 171−178.

(346) Zhao, Z.; Torres-Díaz, I.; Vélez, C.; Arnold, D.; Rinaldi, C. Brownian Dynamics Simulations of Magnetic Nanoparticles Captured in Strong Magnetic Field Gradients. *J. Phys. Chem. C* **2017**, *121* (1), 801−810.

(347) Ye, L.; Pearson, T.; Dolbashian, C.; Pstrak, P.; Mohtasebzadeh, A. R.; Fellows, B.; Mefford, O. T.; Crawford, T. M. Magnetic-Field-Directed Self-Assembly of Programmable Mesoscale Shapes. *Adv. Funct. Mater.* **2016**, *26* (22), 3983−3989.

(348) Rampini, S.; Li, P.; Lee, G. U. Micromagnet arrays enable precise manipulation of individual biological analyte-superparamagnetic bead complexes for separation and sensing. *Lab Chip* **2016**, *16* (19), 3645−3663.

(349) Erb, R. M.; Sebba, D. S.; Lazarides, A. A.; Yellen, B. B. Magnetic field induced concentration gradients in magnetic nanoparticle suspensions: Theory and experiment. *J. Appl. Phys.* **2008**, *103* (6), 063916.

(350) Helseth, L. E.; Wen, H. Z.; Hansen, R. W.; Johansen, T. H.; Heinig, P.; Fischer, T. M. Assembling and Manipulating Two-Dimensional Colloidal Crystals with Movable Nanomagnets. *Langmuir* **2004**, *20* (17), 7323−7332.

(351) Yellen, B. B.; Friedman, G. Programmable Assembly of Colloidal Particles Using Magnetic Microwell Templates. *Langmuir* **2004**, *20* (7), 2553−2559.

(352) Yellen, B.; Friedman, G.; Feinerman, A. Printing super-paramagnetic colloidal particle arrays on patterned magnetic film. *J. Appl. Phys.* **2003**, *93* (10), 7331−7333.

(353) Yellen, B. B.; Hovorka, O.; Friedman, G. Arranging matter by magnetic nanoparticle assemblers. *Proc. Natl. Acad. Sci. U. S. A.* **2005**, *102* (25), 8860−8864.

(354) Chen, P.; Huang, Y.-Y.; Hoshino, K.; Zhang, J. X. J. Microscale magnetic field modulation for enhanced capture and distribution of rare circulating tumor cells. *Sci. Rep.* **2015**, *5* (1), 8745.

(355) Ruan, G.; Vieira, G.; Henighan, T.; Chen, A.; Thakur, D.; Sooryakumar, R.; Winter, J. O. Simultaneous Magnetic Manipulation and Fluorescent Tracking of Multiple Individual Hybrid Nanostructures. *Nano Lett.* **2010**, *10* (6), 2220−2224.

(356) Ahn, T.; Oh, S.; Hu, X.; Lee, J. W.; Park, C. W.; Yang, H. M.; Kim, C.; Kim, J. D. Controlled Self-Assembly for High-Resolution Magnetic Printing. *Small* **2014**, *10* (6), 1081−1085.

(357) Kimura, T.; Yamato, M.; Nara, A. Particle Trapping and Undulation of a Liquid Surface Using a Microscopically Modulated Magnetic Field. *Langmuir* **2004**, *20* (3), 572−574.

(358) Kimura, T.; Sato, Y.; Kimura, F.; Iwasaka, M.; Ueno, S. Micropatterning of Cells Using Modulated Magnetic Fields. *Langmuir* **2005**, *21* (3), 830−832.

(359) Piao, G.; Kimura, F.; Kimura, T. Simultaneous Alignment and Micropatterning of Organic Crystallites under a Modulated Magnetic Field. *Langmuir* **2006**, *22* (10), 4853−4855.

(360) Demirors, A. F.; Beltramo, P. J.; Vutukuri, H. R. Colloidal Switches by Electric and Magnetic Fields. *ACS Appl. Mater. Interfaces* **2017**, *9* (20), 17238−17245.

(361) Demirörs, A. F. Magnetophoretic Assembly of Anisotropic Colloids for Spatial Control of Reinforcement in Composites. *J. Phys. Chem. B* **2016**, *120* (36), 9759−9765.

(362) Xue, X.; Furlani, E. P. Analysis of the Dynamics of Magnetic Core-Shell Nanoparticles and Self-Assembly of Crystalline Superstructures in Gradient Fields. *J. Phys. Chem. C* **2015**, *119* (10), 5714−5726.

(363) Xue, X.; Furlani, E. P. Template-assisted nano-patterning of magnetic core-shell particles in gradient fields. *Phys. Chem. Chem. Phys.* **2014**, *16* (26), 13306−13317.

(364) Xue, X.; Wang, J.; Furlani, E. P. Self-Assembly of Crystalline Structures of Magnetic Core-Shell Nanoparticles for Fabrication of Nanostructured Materials. *ACS Applied Materials Interfaces* **2015**, *7* (40), 22515−22524.

(365) Demiros, A. F.; Pillai, P. P.; Kowalczyk, B.; Grzybowski, B. A. Colloidal assembly directed by virtual magnetic moulds. *Nature* **2013**, *503* (7474), 99−103.

(366) He, L.; Wang, M.; Zhang, Q.; Lu, Y.; Yin, Y. Magnetic assembly and patterning of general nanoscale materials through nonmagnetic templates. *Nano Lett.* **2013**, *13* (1), 264−271.

(367) He, L.; Wang, M.; Ge, J.; Yin, Y. Magnetic Assembly Route to Colloidal Responsive Photonic Nanostructures. *Acc. Chem. Res.* **2012**, *45* (9), 1431−1440.

(368) Ge, J.; Lee, H.; He, L.; Kim, J.; Lu, Z.; Kim, H.; Goebl, J.; Kwon, S.; Yin, Y. Magnetochromatic Microspheres: Rotating Photonic Crystals. *J. Am. Chem. Soc.* **2009**, *131* (43), 15687−15694.

(369) He, L.; Hu, Y.; Han, X.; Lu, Y.; Lu, Z.; Yin, Y. Assembly and Photonic Properties of Superparamagnetic Colloids in Complex Magnetic Fields. *Langmuir* **2011**, *27* (22), 13444−13450.

(370) He, L.; Hu, Y.; Kim, H.; Ge, J.; Kwon, S.; Yin, Y. Magnetic Assembly of Nonmagnetic Particles into Photonic Crystal Structures. *Nano Lett.* **2010**, *10* (11), 4708−4714.

(371) Henderson, J. R.; Crawford, T. M. Repeatability of magnetic-field driven self-assembly of magnetic nanoparticles. *J. Appl. Phys.* **2011**, *109* (7), 07D329.

(372) Henderson, J.; Shi, S.; Cakmaktepe, S.; Crawford, T. M. Pattern transfer nanomanufacturing using magnetic recording for programmed nanoparticle assembly. *Nanotechnology* **2012**, *23* (18), 185304.

(373) Ye, L.; Terry, B.; Mefford, O. T.; Rinaldi, C.; Crawford, T. M. All-nanoparticle concave diffraction grating fabricated by self-assembly onto magnetically-recorded templates. *Opt. Express* **2013**, *21* (1), 1066−1075.

(374) Mohtasebzadeh, A. R.; Ye, L.; Crawford, T. M. Magnetic Nanoparticle Arrays Self-Assembled on Perpendicular Magnetic Recording Media. *Int. J. Mol. Sci.* **2015**, *16* (8), 19769−19779.

(375) Singh, S. K.; Rajib, M. M.; Drobitch, J. L.; Atulasimha, J.; Bandyopadhyay, S.; Subramanian, A. A 3-D NanoMagnetoElectrokinetic model for ultra-high precision assembly of ferromagnetic NWs using magnetic-field assisted dielectrophoresis. *RSC Adv.* **2020**, *10* (65), 39763−39770.

(376) Li, J.; Hill, E. H.; Lin, L.; Zheng, Y. Optical Nanoprinting of Colloidal Particles and Functional Structures. *ACS Nano* **2019**, *13* (4), 3783−3795.

(377) Maragò, O. M.; Jones, P. H.; Gucciardi, P. G.; Volpe, G.; Ferrari, A. C. Optical trapping and manipulation of nanostructures. *Nat. Nanotechnol.* **2013**, *8* (11), 807−819.

(378) Urban, A. S.; Carretero-Palacios, S.; Lutich, A. A.; Lohmüller, T.; Feldmann, J.; Jäckel, F. Optical trapping and manipulation of plasmonic nanoparticles: fundamentals, applications, and perspectives. *Nanoscale* **2014**, *6* (9), 4458−4474.

(379) Lehmuskero, A.; Johansson, P.; Rubinsztein-Dunlop, H.; Tong, L.; Käll, M. Laser trapping of colloidal metal nanoparticles. *ACS Nano* **2015**, *9* (4), 3453−3469.

(380) Ashkin, A.; Dziedzic, J. M.; Bjorkholm, J. E.; Chu, S. Observation of a single-beam gradient force optical trap for dielectric particles. *Opt. Lett.* **1986**, *11* (5), 288−290.

(381) Svoboda, K.; Block, S. M. Optical trapping of metallic Rayleigh particles. *Opt. Lett.* **1994**, *19* (13), 930−932.

(382) Hansen, P. M.; Bhatia, V. K.; Harrit, N.; Oddershede, L. Expanding the Optical Trapping Range of Gold Nanoparticles. *Nano Lett.* **2005**, *5* (10), 1937−1942.

(383) Bosanac, L.; Aabo, T.; Bendix, P. M.; Oddershede, L. B. Efficient Optical Trapping and Visualization of Silver Nanoparticles. *Nano Lett.* **2008**, *8* (5), 1486−1491.

(384) Prikulis, J.; Svedberg, F.; Käll, M.; Enger, J.; Ramser, K.; Goksör, M.; Hanstorp, D. Optical Spectroscopy of Single Trapped Metal Nanoparticles in Solution. *Nano Lett.* **2004**, *4* (1), 115−118.

(385) Selhuber-Unkel, C.; Zins, I.; Schubert, O.; Sönnichsen, C.; Oddershede, L. B. Quantitative Optical Trapping of Single Gold Nanorods. *Nano Lett.* **2008**, *8* (9), 2998−3003.

(386) Nome, R. A.; Guffey, M. J.; Scherer, N. F.; Gray, S. K. Plasmonic Interactions and Optical Forces between Au Bipyramidal Nanoparticle Dimers. *J. Phys. Chem. A* **2009**, *113* (16), 4408−4415.

(387) Jauffred, L.; Richardson, A. C.; Oddershede, L. B. Three-Dimensional Optical Control of Individual Quantum Dots. *Nano Lett.* **2008**, *8* (10), 3376−3380.

(388) Grier, D. G. A revolution in optical manipulation. *Nature* **2003**, *424* (6950), 810−816.

(389) Chaumet, P. C.; Nieto-Vesperinas, M. Time-averaged total force on a dipolar sphere in an electromagnetic field. *Opt. Lett.* **2000**, *25* (15), 1065−1067.

(390) Arias-González, J. R.; Nieto-Vesperinas, M. Optical forces on small particles: attractive and repulsive nature and plasmon-resonance conditions. *Journal of the Optical Society of America A* **2003**, *20* (7), 1201−1209.

(391) Guffey, M. J.; Scherer, N. F. All-optical patterning of Au nanoparticles on surfaces using optical traps. *Nano Lett.* **2010**, *10* (11), 4302−4308.

(392) Bernatova, S.; Donato, M. G.; Jezek, J.; Pilat, Z.; Samek, O.; Magazzu, A.; Marago, O. M.; Zemanek, P.; Gucciardi, P. G. Wavelength-Dependent Optical Force Aggregation of Gold Nanorods for SERS in a Microfluidic Chip. *J. Phys. Chem. C* **2019**, *123* (9), 5608−5615.

(393) Gargiulo, J.; Violi, I. L.; Cerrota, S.; Chvátal, L.; Cortés, E.; Perassi, E. M.; Diaz, F.; Zemánek, P.; Stefani, F. D. Accuracy and Mechanistic Details of Optical Printing of Single Au and Ag Nanoparticles. *ACS Nano* **2017**, *11* (10), 9678−9688.

(394) Gargiulo, J.; Brick, T.; Violi, I. L.; Herrera, F. C.; Shibanuma, T.; Albella, P.; Requejo, F. G.; Cortés, E.; Maier, S. A.; Stefani, F. D. Understanding and Reducing Photothermal Forces for the Fabrication of Au Nanoparticle Dimers by Optical Printing. *Nano Lett.* **2017**, *17* (9), 5747−5755.

(395) Huergo, M. a. A.; Maier, C. M.; Castez, M. F.; Vericat, C.; Nedev, S.; Salvarezza, R. C.; Urban, A. S.; Feldmann, J. Optical Nanoparticle Sorting Elucidates Synthesis of Plasmonic Nanotriangles. *ACS Nano* **2016**, *10* (3), 3614−3621.

(396) Gargiulo, J.; Cerrota, S.; Cortés, E.; Violi, I. L.; Stefani, F. D. Connecting Metallic Nanoparticles by Optical Printing. *Nano Lett.* **2016**, *16* (2), 1224−1229.

(397) Urban, A. S.; Pfeiffer, T.; Fedoruk, M.; Lutich, A. A.; Feldmann, J. Single-Step Injection of Gold Nanoparticles through Phospholipid Membranes. *ACS Nano* **2011**, *5* (5), 3585−3590.

(398) Urban, A. S.; Lutich, A. A.; Stefani, F. D.; Feldmann, J. Laser printing single gold nanoparticles. *Nano Lett.* **2010**, *10* (12), 4794−4798.

(399) Bao, Y.; Yan, Z.; Scherer, N. F. Optical Printing of Electrodynamically Coupled Metallic Nanoparticle Arrays. *J. Phys. Chem. C* **2014**, *118* (33), 19315−19321.

(400) Nedev, S.; Urban, A. S.; Lutich, A. A.; Feldmann, J. Optical Force Stamping Lithography. *Nano Lett.* **2011**, *11* (11), 5066−5070.

(401) Do, J.; Fedoruk, M.; Jäckel, F.; Feldmann, J. Two-color laser printing of individual gold nanorods. *Nano Lett.* **2013**, *13* (9), 4164−4168.

(402) Chen, J. J.; Loo, J. F. C.; Wang, D. P.; Zhang, Y.; Kong, S. K.; Ho, H. P. Thermal Optofluidics: Principles and Applications. *Adv. Opt. Mater.* **2020**, *8* (1), 1900829.

(403) Donner, J. S.; Baffou, G.; McCloskey, D.; Quidant, R. Plasmon-assisted optofluidics. *ACS Nano* **2011**, 5 (7), 5457−5462.

(404) Winterer, F.; Maier, C. M.; Pernpeintner, C.; Lohmuller, T. Optofluidic transport and manipulation of plasmonic nanoparticles by thermocapillary convection. *Soft Matter* **2018**, 14 (4), 628−634.

(405) Fujii, S.; Kanaizuka, K.; Toyabe, S.; Kobayashi, K.; Muneyuki, E.; Haga, M.-A. Fabrication and placement of a ring structure of nanoparticles by a laser-induced micronanobubble on a gold surface. *Langmuir* **2011**, 27 (14), 8605−8610.

(406) Lin, L.; Peng, X.; Mao, Z.; Li, W.; Yogeesh, M. N.; Rajeeva, B. B.; Perillo, E. P.; Dunn, A. K.; Akinwande, D.; Zheng, Y. Bubble-Pen Lithography. *Nano Lett.* **2016**, 16 (1), 701−708.

(407) Rajeeva, B. B.; Alabandi, M. A.; Lin, L.; Perillo, E. P.; Dunn, A. K.; Zheng, Y. Patterning and fluorescence tuning of quantum dots with haptic-interfaced bubble printing. *J. Mater. Chem. C* **2017**, 5 (23), 5693−5699.

(408) Bangalore Rajeeva, B.; Lin, L.; Perillo, E. P.; Peng, X.; Yu, W. W.; Dunn, A. K.; Zheng, Y. High-Resolution Bubble Printing of Quantum Dots. *ACS Appl. Mater. Interfaces* **2017**, 9 (19), 16725−16733.

(409) Kim, Y.; Ding, H.; Zheng, Y. Enhancing Surface Capture and Sensing of Proteins with Low-Power Optothermal Bubbles in a Biphasic Liquid. *Nano Lett.* **2020**, 20 (10), 7020−7027.

(410) Foti, A.; D'Andrea, C.; Villari, V.; Micali, N.; Donato, M. G.; Fazio, B.; Maragò, O. M.; Gillibert, R.; Lamy de la Chapelle, M.; Gucciardi, P. G. Optical Aggregation of Gold Nanoparticles for SERS Detection of Proteins and Toxins in Liquid Environment: Towards Ultrasensitive and Selective Detection. *Materials (Basel)* **2018**, 11 (3), 440.

(411) Fazio, B.; D'Andrea, C.; Foti, A.; Messina, E.; Irrera, A.; Donato, M. G.; Villari, V.; Micali, N.; Maragò, O. M.; Gucciardi, P. G. SERS detection of Biomolecules at Physiological pH via aggregation of Gold Nanorods mediated by Optical Forces and Plasmonic Heating. *Sci. Rep.* **2016**, 6 (1), 26952.

(412) Namura, K.; Nakajima, K.; Suzuki, M. Quasi-stokeslet induced by thermoplasmonic Marangoni effect around a water vapor micro-bubble. *Sci. Rep.* **2017**, 7 (1), 45776.

(413) Armon, N.; Greenberg, E.; Layani, M.; Rosen, Y. S.; Magdassi, S.; Shpaisman, H. Continuous Nanoparticle Assembly by a Modulated Photo-Induced Microbubble for Fabrication of Micrometric Conductive Patterns. *ACS Appl. Mater. Interfaces* **2017**, 9 (50), 44214−44221.

(414) Thomas, P.; Ghosh, S.; Mallick, A.; Banerjee, A.; Roy, S. Inexpensive Design of a Bio-Chip for Disease Diagnostics: Molecular Biomarker Sensing Microchip Patterned from a Soft Oxometalate-Perylene-Based Hybrid Composite using Thermo-Optical Laser Tweezers. *Eur. J. Inorg. Chem.* **2019**, 2019 (3−4), 469−476.

(415) Rajeeva, B. B.; Wu, Z.; Briggs, A.; Acharya, P. V.; Walker, S. B.; Peng, X.; Bahadur, V.; Bank, S. R.; Zheng, Y. Point-and-Shoot" Synthesis of Metallic Ring Arrays and Surface-Enhanced Optical Spectroscopy. *Adv. Opt. Mater.* **2018**, 6 (10), 1701213.

(416) Setoura, K.; Ito, S.; Miyasaka, H. Stationary bubble formation and Marangoni convection induced by CW laser heating of a single gold nanoparticle. *Nanoscale* **2017**, 9 (2), 719−730.

(417) Zhao, C.; Xie, Y.; Mao, Z.; Zhao, Y.; Rufo, J.; Yang, S.; Guo, F.; Mai, J. D.; Huang, T. J. Theory and experiment on particle trapping and manipulation via optothermally generated bubbles. *Lab Chip* **2014**, 14 (2), 384−391.

(418) Roy, B.; Arya, M.; Thomas, P.; Jürgschat, J. K.; Venkata Rao, K.; Banerjee, A.; Malla Reddy, C.; Roy, S. Self-assembly of mesoscopic materials to form controlled and continuous patterns by thermo-optically manipulated laser induced microbubbles. *Langmuir* **2013**, 29 (47), 14733−14742.

(419) Kang, Z.; Chen, J.; Ho, H.-P. Surface-enhanced Raman scattering via entrapment of colloidal plasmonic nanocrystals by laser generated microbubbles on random gold nano-islands. *Nanoscale* **2016**, 8 (19), 10266−10272.

(420) Jin, C. M.; Lee, W.; Kim, D.; Kang, T.; Choi, I. Photothermal Convection Lithography for Rapid and Direct Assembly of Colloidal

Plasmonic Nanoparticles on Generic Substrates. *Small* **2018**, 14 (45), 1803055.

(421) Greenberg, E.; Armon, N.; Kapon, O.; Ben-Ishai, M.; Shpaisman, H. Nanostructure and Mechanism of Metal Deposition by a Laser-Induced Photothermal Reaction. *Advanced Materials Interfaces* **2019**, 6 (14), 1900541.

(422) Jung, H. Y.; Kim, Y. L.; Park, S.; Datar, A.; Lee, H. J.; Huang, J.; Somu, S.; Busnaina, A.; Jung, Y. J.; Kwon, Y. K. High-performance H2S detection by redox reactions in semiconducting carbon nanotube-based devices. *Analyst* **2013**, 138 (23), 7206−7211.

(423) Wang, Z.; Yi, K.; Lin, Q.; Yang, L.; Chen, X.; Chen, H.; Liu, Y.; Wei, D. Free radical sensors based on inner-cutting graphene field-effect transistors. *Nat. Commun.* **2019**, 10 (1), 1544.

(424) Yildirim-Tirgil, N.; Lee, J.; Cho, H.; Lee, H.; Somu, S.; Busnaina, A.; Gu, A. Z. A SWCNT based aptasensor system for antibiotic oxytetracycline detection in water samples. *Analytical Methods* **2019**, 11 (20), 2692−2699.

(425) Francioso, L.; De Pascali, C.; Creti, P.; Radogna, A. V.; Capone, S.; Taurino, A.; Epifani, M.; Baldacchini, C.; Bizzarri, A. R.; Siciliano, P. A. Nanogap Sensors Decorated with SnO2 Nanoparticles Enable Low-Temperature Detection of Volatile Organic Compounds. *ACS Applied Nano Materials* **2020**, 3 (4), 3337−3346.

(426) Chmela, O.; Sadílek, J.; Domènech-Gil, G.; Samà, J.; Somer, J.; Mohan, R.; Romano-Rodriguez, A.; Hubálek, J.; Vallejos, S. Selectively arranged single-wire based nanosensor array systems for gas monitoring. *Nanoscale* **2018**, 10 (19), 9087−9096.

(427) Kravets, V. G.; Kabashin, A. V.; Barnes, W. L.; Grigorenko, A. N. Plasmonic Surface Lattice Resonances: A Review of Properties and Applications. *Chem. Rev.* **2018**, 118 (12), 5912−5951.

(428) Ye, S.; Zha, H.; Xia, Y.; Dong, W.; Yang, F.; Yi, C.; Tao, J.; Shen, X.; Yang, D.; Nie, Z. Centimeter-Scale Superlattices of Three-Dimensionally Oriented Plasmonic Dimers with Highly Tunable Collective Properties. *ACS Nano* **2022**, 16 (3), 4609−4618.

(429) Wang, W.; Ramezani, M.; Väkeväinen, A. I.; Törmä, P.; Rivas, J. G.; Odom, T. W. The rich photonic world of plasmonic nanoparticle arrays. *Mater. Today* **2018**, 21 (3), 303−314.

(430) Scarabelli, L.; Vila-Liarte, D.; Mihi, A.; Liz-Marzán, L. M. Templated Colloidal Self-Assembly for Lattice Plasmon Engineering. *Accounts of Materials Research* **2021**, 2 (9), 816−827.

(431) Tian, L.; Wang, C.; Zhao, H.; Sun, F.; Dong, H.; Feng, K.; Wang, P.; He, G.; Li, G. Rational Approach to Plasmonic Dimers with Controlled Gap Distance, Symmetry, and Capability of Precisely Hosting Guest Molecules in Hotspot Regions. *J. Am. Chem. Soc.* **2021**, 143 (23), 8631−8638.

(432) Niu, R.; Song, C.; Gao, F.; Fang, W.; Jiang, X.; Ren, S.; Zhu, D.; Su, S.; Chao, J.; Chen, S.; Fan, C.; Wang, L. DNA Origami-Based Nanoprinting for the Assembly of Plasmonic Nanostructures with Single-Molecule Surface-Enhanced Raman Scattering. *Angew. Chem., Int. Ed.* **2021**, 60 (21), 11695−11701.

(433) Negoro, H.; Sugimoto, H.; Hinamoto, T.; Fujii, M. Template-Assisted Self-Assembly of Colloidal Silicon Nanoparticles for All-Dielectric Nanoantenna. *Adv. Opt. Mater.* **2022**, 10 (8), 2102750.

(434) Peng, J.; Jeong, H.-H.; Lin, Q.; Cormier, S.; Liang, H.-L.; De Volder, M. F. L.; Vignolini, S.; Baumberg, J. J. Scalable electrochromic nanopixels using plasmonics. *Science Advances* **2019**, 5 (5), No. eaaw2205.

(435) Yang, F.; Ye, S.; Dong, W.; Zheng, D.; Xia, Y.; Yi, C.; Tao, J.; Sun, C.; Zhang, L.; Wang, L.; Chen, Q.; Wang, Y.; Nie, Z. Laser-Scanning-Guided Assembly of Quasi-3D Patterned Arrays of Plasmonic Dimers for Information Encryption. *Adv. Mater.* **2021**, 33 (24), 2100325.

(436) Lee, J. B.; Walker, H.; Li, Y.; Nam, T. W.; Rakovich, A.; Sapienza, R.; Jung, Y. S.; Nam, Y. S.; Maier, S. A.; Cortés, E. Template Dissolution Interfacial Patterning of Single Colloids for Nano-electrochemistry and Nanosensing. *ACS Nano* **2020**, 14 (12), 17693−17703.

(437) Frisenda, R.; Giovanelli, E.; Mishra, P.; Gant, P.; Flores, E.; Sánchez, C.; Ares, J. R.; Perez de Lara, D.; Ferrer, I. J.; Pérez, E. M.; Castellanos-Gomez, A. Dielectrophoretic assembly of liquid-phase-

exfoliated TiS3 nanoribbons for photodetecting applications. *Chem. Commun.* **2017**, *53* (45), 6164−6167.

(438) Zhang, Y.; Jie, J.; Sun, Y.; Jeon, S.-G.; Zhang, X.; Dai, G.; Lee, C. J.; Zhang, X. Precise Patterning of Organic Single Crystals via Capillary-Assisted Alternating-Electric Field. *Small* **2017**, *13* (25), 1604261.

(439) Myny, K. The development of flexible integrated circuits based on thin-film transistors. *Nature Electronics* **2018**, *1* (1), 30−39.

(440) Zhu, J.; Hersam, M. C. Assembly and Electronic Applications of Colloidal Nanomaterials. *Adv. Mater.* **2017**, *29* (4), 1603895.

(441) Engel, M.; Farmer, D. B.; Azpiroz, J. T.; Seo, J.-W. T.; Kang, J.; Avouris, P.; Hersam, M. C.; Krupke, R.; Steiner, M. Graphene-enabled and directed nanomaterial placement from solution for large-scale device integration. *Nat. Commun.* **2018**, *9* (1), 4095.

(442) Xu, X.; Mukadam, Z.; Amoroso, G.; Freeley, M.; Palma, M. Directed assembly of multiplexed single chirality carbon nanotube devices. *J. Appl. Phys.* **2021**, *129* (2), 024305.

(443) Minari, T.; Kanehara, Y.; Liu, C.; Sakamoto, K.; Yasuda, T.; Yaguchi, A.; Tsukada, S.; Kashizaki, K.; Kanehara, M. Room-Temperature Printing of Organic Thin-Film Transistors with π-Junction Gold Nanoparticles. *Adv. Funct. Mater.* **2014**, *24* (31), 4886−4892.

(444) Minari, T.; Liu, C.; Kano, M.; Tsukagoshi, K. Controlled Self-Assembly of Organic Semiconductors for Solution-Based Fabrication of Organic Field-Effect Transistors. *Adv. Mater.* **2012**, *24* (2), 299−306.

(445) Park, H.; Kim, B.-J.; Kim, J. Electroluminescence from InGaN/GaN multi-quantum-wells nanorods light-emitting diodes positioned by non-uniform electric fields. *Opt. Express* **2012**, *20* (23), 25249−25254.

(446) Eo, Y. J.; Yoo, G. Y.; Kang, H.; Lee, Y. K.; Kim, C. S.; Oh, J. H.; Lee, K. N.; Kim, W.; Do, Y. R. Enhanced DC-Operated Electroluminescence of Forwardly Aligned p/MQW/n InGaN Nanorod LEDs via DC Offset-AC Dielectrophoresis. *ACS Appl. Mater. Interfaces* **2017**, *9* (43), 37912−37920.

(447) Park, H. K.; Yoon, S. W.; Eo, Y. J.; Chung, W. W.; Yoo, G. Y.; Oh, J. H.; Lee, K. N.; Kim, W.; Do, Y. R. Horizontally assembled green InGaN nanorod LEDs: scalable polarized surface emitting LEDs using electric-field assisted assembly. *Sci. Rep.* **2016**, *6* (1), 28312.

(448) Han, J.; Nelson, Z.; Chua, M. R.; Swager, T. M.; Niroui, F.; Lang, J. H.; Bulović, V. Molecular Platform for Fast Low-Voltage Nanoelectromechanical Switching. *Nano Lett.* **2021**, *21* (24), 10244−10251.

(449) Subramanian, A.; Alt, A. R.; Dong, L.; Kratochvil, B. E.; Bolognesi, C. R.; Nelson, B. J. Electrostatic Actuation and Electromechanical Switching Behavior of One-Dimensional Nanostructures. *ACS Nano* **2009**, *3* (10), 2953−2964.

(450) Niroui, F.; Saravanapavanantham, M.; Han, J.; Patil, J. J.; Swager, T. M.; Lang, J. H.; Bulović, V. Hybrid Approach to Fabricate Uniform and Active Molecular Junctions. *Nano Lett.* **2021**, *21* (4), 1606−1612.

(451) Kim, K.; Xu, X.; Guo, J.; Fan, D. L. Ultrahigh-speed rotating nanoelectromechanical system devices assembled from nanoscale building blocks. *Nat. Commun.* **2014**, *5* (1), 3632.

(452) Fan, D. L.; Zhu, F. Q.; Cammarata, R. C.; Chien, C. L. Electric tweezers. *Nano Today* **2011**, *6* (4), 339−354.